CFD Analysis on Aerodynamic Drag Reduction of Pickup Vehicles Using Rear Spoiler

By

Engidayehu Wotango Wolde

A Thesis Submitted To

The Department Of Automotive Engineering

School Of Mechanical, Chemical And Materials Engineering

Presented In Partial Fulfillment Of The Requirement For The Degree Of Master Of Science In

Automotive Engineering

Office of Graduate Studies

Adama Science and Technology University

June, 2019

Adama, Ethiopia

CFD Analysis on Aerodynamic Drag Reduction of Pickup Vehicles Using Rear Spoiler

By

Engidayehu Wotango Wolde

Advisor: N. Ramesh Babu (Asst. Prof)

A Thesis Submitted To

The Department Of Automotive Engineering

School Of Mechanical, Chemical And Materials Engineering Presented In Partial Fulfillment Of The Requirement For The Degree Of Master Of Science In

Automotive Engineering

Office of Graduate Studies

Adama Science and Technology University

June, 2019

Adama, Ethiopia

Approval of Board of Examiners

We, the undersigned, members of the Board of Examiners of the final open defense by Engidayehu Wotango Wolde have read and evaluated his thesis entitled "CFD Analysis On Aerodynamic Drag Reduction of Pickup Vehicles Using Rear Spoiler" and examined the candidate. This is, therefore, to certify that the thesis has been accepted in partial fulfillment of the requirement of the Degree of Master of Science in Automotive Engineering.

______________________	______________________	______________
Chairperson	Signature	Date
______________________	______________________	______________
Internal Examiner	Signature	Date
______________________	______________________	______________
External Examiner	Signature	Date

Declaration

I hereby declare that this MSc Thesis is my original work and has not been presented for a degree in any other university, and all sources of material used for this thesis have been duly acknowledged.

Name: Engidayehu Wotango Wolde

Signature:_________________

This MSc Thesis has been submitted for examination with my approval as thesis Advisor.

Name: N. Ramesh Babu (Asst Prof)

Signature:__________________

Date of submission:_______________

ACKNOWLEDGEMENT

First of all, I would like to thank immensely my Lord, the Lord God for all His Provisions and Blessings throughout my life and the thesis work. I would also like to thank my parents Wotango Wolde and Elfinesh Worku, and my Family for their support and encouragement. I would like to express my sincere gratitude for my Advisor N. Ramesh Babu (Ass. Professor) for his excellent guidance, moral support and constructive criticism. Finally, I thank my friends for their suggestions and helps they provided for me.

TABLE OF CONTENTS

CHAPTER **PAGE**

LIST OF TABLES

TABLE **PAGE**

LIST OF FIGURES

FIGURES **PAGE**

ACRONYMS AND SYMBOLS

AFC	Active Flow Control
BC	Boundary Condition
BL	Boundary Layer
BEM	Boundary Element Method
CAD	Computer Aided Drafting
CFD	Computational Fluid Dynamics
DNS	Direct Numerical Simulation
FVM	Finite Volume Method
FEM	Finite Element Method
LBM	Lattice Boltzmann Method
LES	Large Eddy Simulation
OLD	Outer Layer Device
RAM	Random Access Memory
RANS	Reynolds-Averaged Navier-Stokes
RNG	Re Normalized Group
SST	Shear Stress Transport
SUVs	Sport Utility Vehicles
3D	Three Dimensional
VG	Vortex Generator
C	Specific Heat Capacity
C_l	Lift Coefficient
CPU	Central Processing Unit

Cop	Coefficient of Pressure
C_d	Drag Coefficient
C_p	Pressure Drag
F_f	Friction Drag
F_l	Lift Force
F_d	Drag Force
P_s	Static Pressure
P_d	Dynamic Pressure
P	Pressure
T	Temperature
V	Speed
kmph	Kilometer per hour
g	Gravity
K	Coefficient of Thermal Conductivity
mm	Millimeters
m/s	Meter per Second
ρ	Density
ε	Epsilon
Φ	Viscous Dissipation Function
μ	Viscosity
%	Percentage

ABSTRACT

In order to save energy and to conserve the environment, a reduction in the fuel consumption is a primary concern in the automotive industry. Currently, there are several options for improvement in the fuel economy, such as enhancing the engine performance, decreasing the automobile weight and reducing the aerodynamic drag. A large percentage of the usable fuel is employed in overcoming the aerodynamic drag at highway speeds and therefore if reduced could produce a large reduction in the total fuel consumption and reduce the negative environmental effects. In this thesis air flow over a pickup vehicle with spoiler attached on the rear end of the vehicle roof at different inclination angle and spoiler length using computational fluid dynamics (CFD) with the objective of reducing the aerodynamic drag was studied. All numerical simulations were performed using commercial CFD software Fluent and realizable k-epsilon turbulence modelling. A 1/12 scaled down generic pickup model with extended cab modeled with SolidWorks was used as the baseline model. Improvements in drag coefficient and lift coefficient were obtained in models with spoiler when compared to the baseline model without any add-on device. A drag reduction of 6.50%, 6.12%, and 0.493% was achieved on model one, model three and model two respectively when compared to the baseline model. The decrease in the amount of drag was attributed to the decrease in wake region and swirling air inside the bed box of the pickup. Because of the reduction in drag a maximum of 3.90% reduction in fuel consumption was achieved. The lift coefficient of the baseline model was also reduced to 22.47% on model two, 14.55% on model three and 4.30% on model one at a vehicle speed of 120 kmph. This reduction in lift coefficient increases vehicle stability at high speed. Overall aerodynamic drag reduction of pickup vehicle using spoiler as an add-on device which leads to better fuel economy was shown here. For future further improvement in drag and lift coefficients can be made possible using optimization software and/or using synergetic effect of different aerodynamic add-on devices.

Keywords: Add-on device, Drag and Lift coefficient, Fuel consumption, pickup vehicle, Turbulence modelling.

CHAPTER ONE

INTRODUCTION

In this chapter background of the study, statement of the problem, objective of the study, scope of the study, significance of the study, scope of the study, beneficiaries, and structure of the study is explained.

1.1 Back ground of the study

The narrative of the horseless carriage, as the car was initially starting in Europe. In 1860, a French engineer named Etienne Lenoir invented an internal combustion engine that used illuminating gas for fuel and an electric spark for ignition. It was used to drive machinery and became the first commercial gas engine. In 1866, Otto and Lange of Germany improved upon the gas engine by developing the four-stroke cycle, which is still used today. In 1885, Daimler, another German, used the Otto cycle in a gas vapor engine, which he manufactured in quantity. The following year he applied his petrol engine to a motorcar. Daimler's engine was used in France by Emile Levassor, who designed a vehicle that set the basic mechanical pattern for modern automobiles [1].

Due to industrialization, and need of mobile labor mankind started to travel in a modern way in the early 19th century. In major European cities, public transport systems were established in the 1830s and 1840s and the horse-drawn omnibus became a common feature in city traffic. The horse-drawn buses were followed by steam engine buses. At the end of the 19th century the steam engine was replaced by electric motors and soon came the internal combustion engine. The early truck-based buses had the engine located at the front, as shown in Figure 1.1.

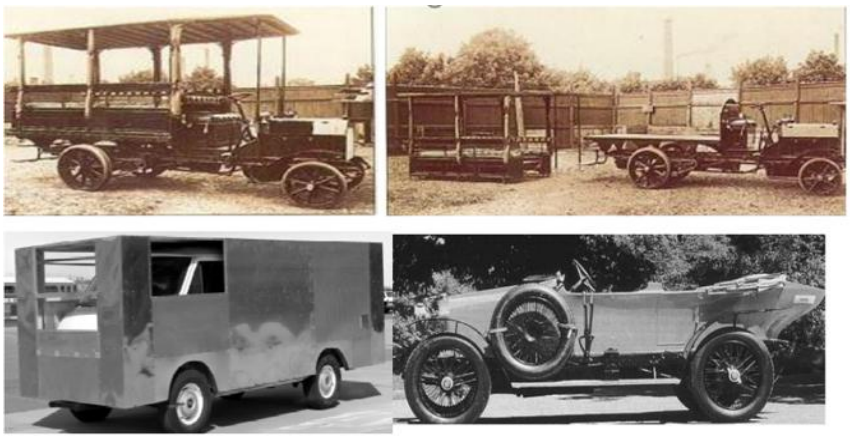

Figure 1.1. A Scania truck used as transportation [1].

Since the inception of the modern motor vehicle in early 1900's, vehicle manufacturers have shown little interest to streamline vehicle body shape for better aerodynamic efficiency as their priority was to make stylish cars. The oil crisis due to Middle East oil embargo in 1970s compelled vehicle manufacturers to bring sound aerodynamic design to the forefront for practical and scientific uses rather than for aesthetic purposes as in previous decades. Ethiopia spends billions of dollars on annual basis for importing fuel. If it was possible to reduce the fuel consumption by a little percentage a great deal of money can be saved. In addition to the economic benefit, fuel consumption reduction also helps in avoiding environmental upside. The environmental upside has revealed itself currently through El Nino which caused devastating drought especially in eastern Africa. So, tackling this upside means reducing the amount of fuel consumption which will come into effect by decreasing aerodynamic drag [2].

The aerodynamic drag exceeds fifty percent of the total resistance to motion at speeds above 70 Km/h. It is the most important factor, responsible for resistance to motion, for speeds above 100 Km/h. Automobile body designers have understood its importance and a large number of efforts have been made [2]. They have tried to stream line vehicle body and use drag reduction add-on devices also. These efforts include studies based on scale modelling and computer simulation approaches.

The aerodynamic effects on current designs of vehicle add-ons spoilers, bull bars, roof racks, taxi signs and ladders were not well studied and documented except some studies by Faerber [3] in 1950s. Although the primary focuses of vehicle manufacturers and researchers have been concentrated on fuel saving devices of the commercial vehicles till to date [4]. As the number of passenger cars have been increased significantly worldwide, it is utmost important to study the effects of various add-ons of the passenger car on fuel cost as well as environmental impact.

Installing a sloping front roof on a lorry could save as much as 7% of fuel costs Alexander, [5]. Even small changes to design and shape will make a difference. Vehicles that travel at higher speeds and for longer distances will benefit most from aerodynamic styling, giving greater savings. Drag is the energy lost pushing through air, and it accounts 26% for most of the fuel used on long distance journeys, regardless of vehicle type. Overcoming drag uses approximately 60% of fuel used at cruising speeds when loaded, 70% when empty.

Sharp corners, racks and parts that stick out will add “parasitic drag”, further reducing fuel efficiency [5].

The performance, handling, safety, and comfort of an automobile are significantly affected by its aerodynamic properties. Extra parts are added to the body like rear spoilers, lower front and rear bumpers, air dams and many more aerodynamic aids as to direct the airflow in different way and offer greater drag reduction to the car and at the same time enhance the stability. Rear spoiler is a component which is used to decrease the overall drag, and at the same time increase downward force of a vehicle especially passenger car. It is an aerodynamic device that is designed to ‘spoil’ unfavorable air movement across a car body. Main fixing location is at rear portion, depends on shape of the rear portion either the car is square back, notchback or fastback because not all rear spoiler can be fixed at any type of rear portion of a car. However, spoiler can also be attached to front/rear bumper as air dam. The use of rear spoiler can contribute to the reduction of drag. The reduction of drag force can save fuel; Moreover, spoiler can also be used to control stability at cornering. Besides reducing drag, it can reduce rear-axle lift.

1.2 Statement of the problem

Swirling motion of air inside the bed box of pickup vehicles in addition to the wide wake region subjects this vehicles to high amount of drag. The aerodynamic drag is the most important factor, responsible for resistance to motion specially at high speeds. With increased resistance to motion the vehicle must produce additional power by utilizing more fuel to overcome the drag. With rising oil price and with requirement of huge amount of foreign currency to import fuel in addition to the increasing number of vehicles, the consumption of more fuel threatens our shivering economy. Besides, there will be more emission from more fuel supply which has its own adverse environmental impact, again affecting the economy of our nation by a devastating drought and/or climate change.

1.3 Objectives of the study

1.3.1 General objective

The general objective of this thesis is to reduce the overall aerodynamic drag of a pickup vehicle by employing spoiler on the rear end of its roof.

1.3.2 Specific objectives

The specific objectives of the study are:

- To model the pickup vehicle by SolidWorks.
- To model the spoilers using CAD.
- Meshing the models using ANSYS meshing.
- To analyse the air flow around the vehicle using ANSYS Fluent.
- To compare the drag coefficients of the different spoilers attached to the baseline vehicle.

1.4 Scope of the study

This work is only limited to reducing the drag of a pickup vehicle using spoiler which is attached to the rear end of the vehicle roof, and analyse the air flow around the vehicle using CFD. Wind tunnel test of the prototype is not included.

1.5 Significance of the study

The significance of this study is that it helps in minimizing the fuel consumption of pickup vehicles allowing the owners to save their money and environment (which is directly related to health).

It is true that aerodynamics can be improved by properly designing various component profiles. Computational Fluid Dynamics (CFD) is done to save cost, and time of running high cost experiments using experimental wind tunnel. These researches reduce the consumption of fuel and production of harmful emissions to the atmosphere. Whereas the result of this paper can be useful as one of the references for any individual, researcher or manufacturer who are interested in pickup aerodynamics.

1.6 Beneficiaries

As the environment and the ones living in it are affected by the emissions from vehicles, which is the result of increased fuel consumption because of the need to overcome high drag, they also are who benefit from this work. Hence, pickup vehicle owners will benefit from the reduced amount of drag.

1.7 Structure of the report

This study consists of five chapters. The first chapter is introduction about the study. It includes the background of study, problem statement, objectives, scopes, significant of the study, beneficiaries and structure of the report. Chapter two focuses on different literatures which emphasize on study of vehicle aerodynamics. Chapter three describes materials and methodology used to complete this work. The results and discussions are presented in chapter four. The generated data of pressure force, lift force, drag coefficient and lift coefficient are presented in form of tables and graphics for quantitative and qualitative discussion. The contours of flow are also discussed to understand the best design characteristics. The final chapter of this thesis consists of conclusion and recommendations.

CHAPTER TWO

LITERATURE REVIEW

To understand the researches done in the past and gain insight in their studies reviewing different literatures is mandatory. In this chapter different types of literature focusing on CFD analysis on various vehicles and add-on devices are covered. At the end of this chapter the research gap is pointed out.

2.1 Different CFD Analyses

Vivek Yakkundi et al. [6] investigated the effect of rear spoiler on sedan and front spoiler above windshield of a hatchback model. The comparison is done on both with and without spoiler. The CFD investigations are done with 3 turbulence models which show that the drag marginally increases, but there is reduction in lift which implies increase in down force and the function of the spoiler increased at higher speeds.

Jiyan et al. [7] have done simulation analysis of car with and without spoiler. Different 4-digit NACA series airfoils at different angle of attack were analyzed and the most efficient airfoil was taken for spoiler design. Also, the best height of the spoiler was analyzed. They have shown that at optimum angle of attack and spoiler height the rear spoiler increases negative lift force and decreased drag force. Rubel et al. [8] observed that at a particular spoiler height the spoiler that possess smaller angle of wind collision gives higher drag force. There was higher pressure behind the spoiler but lower pressure behind the rear of the vehicle.

Karthick et al. [9] presented a numerical simulation of flow around racing car with spoiler positioned at the rear-end using CFD. A three-dimensional computer model of a racing car was used as the base model. It was found that at the certain height of spoiler and wind collision angle, the change in CD is negligible but CL changes significantly as the speed of the racing car increases. Whereas Rakibul et al. [10] have concentrated on different aspects of analysis of aerodynamic drag of racing cars and different drag reduction techniques such as rear under body modification and exhaust gas redirection towards the rear separation zones. The drag coefficient of the car under analysis is found to be 0.3233 and it is evident that the drag can be reduced up to 22.13% by different rear under-body modifications and up to 9.5% by exhaust gas redirection towards the separated region at the rear of the car.

Kelbessa et al. [11] they have studied the effects of fluid flow and the effective drag of the vehicle over a 3D standard car (Bolero) with attached Rear Spoiler by using CFD and concluded that the drag of the vehicle decreased by 4.8%. Sathish et al. [12] have designed a rear car spoiler. They have analyzed different models of spoilers. It is shown in the analysis that the pressure and velocity have decreased whereas drag force, lift force and mass flow rate have increased with increasing vehicle speed.

Zhigang Yang and Bahram Khalighi [13] steady state formulation was used to simulate flow over pickup vehicles. The simulation was to assess the capabilities of the currently used CFD tools for vehicle aerodynamic development for pickup vehicles. Detailed comparisons were made between the CFD simulations and the existing experiments for a generic pickup vehicle. It was found that the flow structures obtained from the CFD calculations are very similar to the corresponding measured values. Comparison for aerodynamic drags was carried out for both the generic pickup vehicle and a production pickup vehicle. Both the simulations and the measurements show the same trends for the drag as the vehicle geometry changes.

Jeong et al. [14] quantitatively examined the drag reduction effects of typical and modified cab roof fairings through wind tunnel and numerical simulation. The wind tunnel experiment is done for scaled commercial vehicle. It is shown that the modified CRF significantly changes the flow structure, leading to approximately 19% drag reduction. Chaitanya et al. [15] have modified the profile of basic truck-trailer model by providing wind deflector on truck’s cabin, vortex trap, mini skirt, vortex strake and aerodynamic revolute. It has been analyzed that, due to profile modification the aerodynamic drag has been reduced by 21 %, which reduces the fuel consumption by 4 liters for 100 km for diesel powered truck. Whereas Alamaan Altaf et al. [16] have worked to obtain a baseline drag value for a simplified MAN TGX series truck using CFD, and the drag reduction of a proposed elliptically shaped flap is compared to aerodynamically equivalent rectangular flaps. The optimal mounting angle and the length of ellipse semi major axis are calculated. Also drag reduction for perforated flap is analyzed. A maximum drag reduction of 11.1% is achieved using an elliptical flap with 0.12m semi-major axis; compared to 6.37% for a length equivalent rectangular flap.

Mohab et al. [17] investigated the effect of crosswinds on the near wake structure of a vehicle with and without boat tails. During crosswind a quadratic increase in drag was observed, as a function of yaw angle. Boat-tail with a slant angle of 15, at zero yaw, has resulted in a drag reduction of up to 50%, relative to the baseline vehicle.

Chunhui et al. [18] presented computational studies to investigate under hood airflow features associated with radiator performance and cooling drag. It is shown that by properly adjusting the cooling airflow pattern, simultaneous improvement of radiator performance and total vehicle drag can be achieved.

Premoli et al. [19] have analyzed the variation, interms of aerodynamic coefficients obtained with moving and still model simulations. the lateral force and the rolling moment coefficients are lower with the stationary model of about 5% and the differences are of about 12% for the vertical force coefficient. It is concluded that even if static tests are not conservative, the differences in terms of CWC are significantly low in the STBR scenario.

Ping et al. [20] employed an aerodynamic design optimization framework using a discrete adjoint approach with open field operation and manipulation. To demonstrate their design-optimization framework, they optimized the ramp shape of a simple bluff geometry and analyzed the flow in detail. They have achieved 9.4% drag reduction, which is validated by wind tunnel experiments. Furthermore, they have applied the framework to solve two more complex aerodynamic- shape-optimization applications: an unmanned aerial vehicle, and a car. For these two cases, the drag is reduced by 5.6% and 12.1%, respectively.

Avadiar et al. [21] experimentally investigated the time-averaged wake through wind tunnel test. Velocities maps and profiles, drag-force measurements and base pressure distributions are used to characterize and quantify the flow behind and around the vehicle. The results have indicated that the near wake and base pressure distribution is dominated by up-wash caused by flow exiting the smooth underbody diffuser.

Luckhurst et al. [22] have investigated a very small base geometry change. They have used Detached Eddy Simulations (DES) to obtain time-averaged and instantaneous data; allowing the effect of horizontal base slats on global forces and wake structures to be presented. The results have shown that the scope for very small changes to a simplified road vehicle, in areas that have not previously been explored, to reduce overall drag with minimal aesthetic penalties.

Firoz et al. [2] they have conducted study using a reduced scale (25%) detailed model of a production large family size passenger car. Industrial Wind Tunnel was used to measure the aerodynamic properties of a test vehicle and vehicle add-ons experimentally. The vehicle add-ons had significant effects on aerodynamic drag and have generated 5 to 30% more aerodynamic drag depending on yaw angles. Sumit et al. [23] have also used a scale model to experimentally evaluate the automobile aerodynamics in a wind tunnel. They have considered Three cases, they are model without polish, model with polish and model with add-on, a load on the roof. A reduction in drag coefficient due to polishing was noticed, and drag has been increased due to vehicle add-on.

Malviya et al. [24] have analyzed Flow paths and pressure distribution in the flow field. They have injected momentum at the top windward edge of the semi-trailer that has provided a significant reduction in aerodynamic drag coefficient which was equivalent to that achieved by the cab roof fairing.

Rohatgi et al. [25] have used a small-scale model of General Motor SUV and tested in the wind tunnel. Drag reduction of 26% and 6.5% was obtained by rear fairing and rear screen respectively. Vortex generators were also tested. Results have shown that Aesthetics and practical considerations can affect implementation of these options. Giacomo et al. [26] they have used to study the influence of after body rounding on the aerodynamic characteristics of a fastback vehicle model by experimental and numerical analysis. At zero crosswind, rounded edges resulted a minimal impact on drag due to opposite effects over the rear slant and the base. Unfortunately, rounded edges resulted in a detriment of the lateral stability.

Ram Bansal and R.B.Sharma [27] have used different types of aerodynamic add-on devices on the base line car to get the results for the coefficient of drag and lift. The results have shown that spoiler with VGs is more effective add-on device to reduce the drag coefficient and lift coefficient.

Hyeon et al. [28] optimized the bobsleigh bumper shape to reduce aerodynamic drag using three-dimensional Reynolds averaged Navier–Stokes analysis and surrogate modeling. The results show that the aerodynamic drag of the bobsleigh was reduced by 3.08% with the optimization compared with the reference design.

Ziyu et al. [29] conducted optimization. Eight body design variables were selected after analyzing the flow field. The first phase of body optimization was conducted for the front of the vehicle, the second phase for the rear of the vehicle, and the third phase for the global vehicle. The optimization resulted in reduction of the front drag by 5.64%, then the rear drag by 7.21%, and finally the global drag by 10.34%, without changing the design style.

Yiping et al. [30] carried out numerical simulation to investigate the influence of the dimpled non smooth surface, which was added on the rear slope of a general vehicle body to reduce the aerodynamic drag. The decrease in the negative zone, the turbulence kinetic energy and the vorticity in the wake showed that the dimpled non-smooth surface had a positive effect on the reduction in the drag. Xu et al. [31] presented a surrogate model-based aerodynamic shape optimization method applied to the wind deflector of a tractor-trailer. The drag coefficient of the tractor-trailer with and without the wind deflector subjected to crosswinds was analyzed. The numerical results have shown that wind deflector can decrease drag coefficient.

2.2 Pickup vehicle aerodynamics

In the automotive industry, pickup vehicles are known for their relatively higher drag coefficients [32] which suggest that there is room for improvement. Previous studies performed on different types of vehicle have showed that with proper modification and addition of some devices the amount of drag coefficient can be reduced. Flow control devices such as cabin flaps [34] and placing geometrically optimized bumps on the rear end of the cabin roof of a generic truck [33] are another promising strategy that does not require major changes in vehicular geometry.

We can divide vehicle aerodynamics into internal and external flow categories. The main concern of this thesis is the external flow. External flow characteristics are dependent on the geometrical configuration and Reynolds number of the flow. Figure 2.1 shows how flow varies on the external surface of a pickup vehicle. External flow can be differentiated by drag, lift and stability [35]. Surface pressure, the maximum amount of pressure occurs at the truck's front surface where the stagnation point is generated. Maximum static pressure occurs on the grill of the truck and the windshield. It is interesting to note that the truck tires are also subjected to a high aerodynamic pressure as the flow velocity reduces in these areas [36].

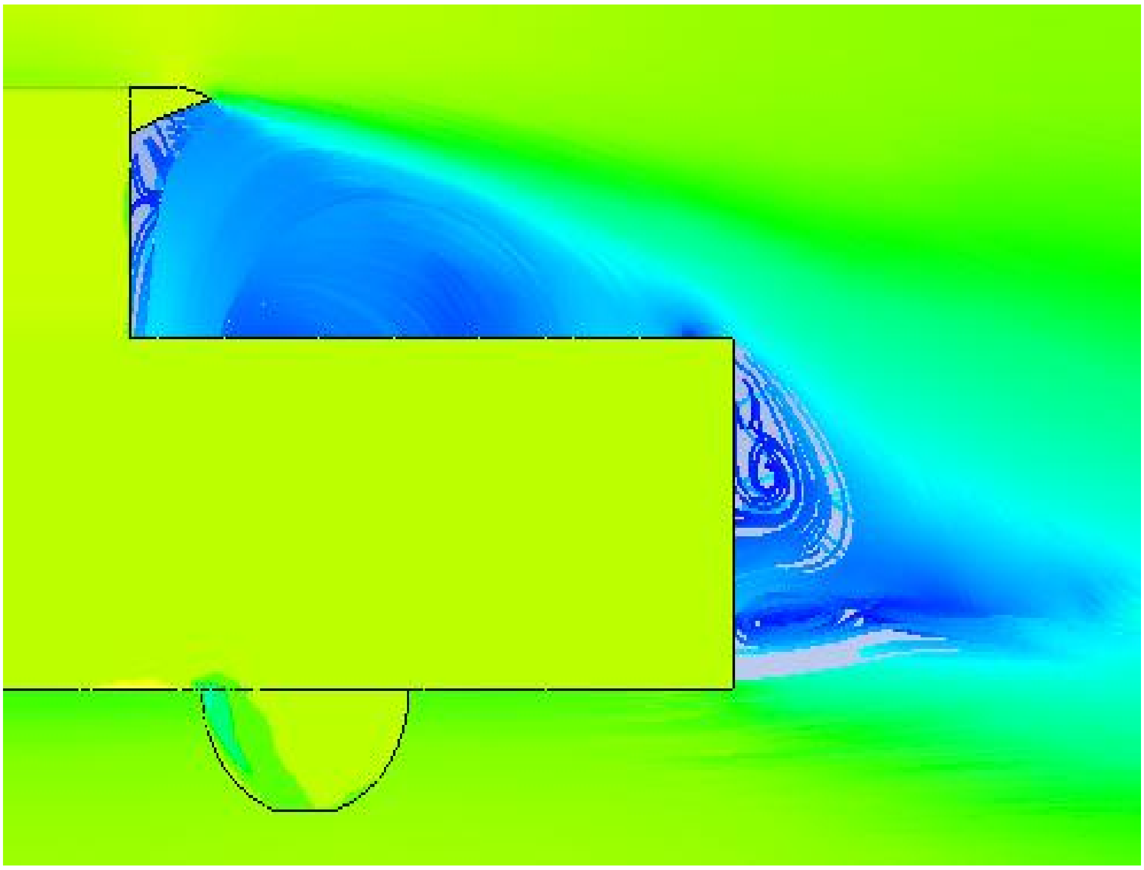

Figure 2.1. stream line on symmetry plane

Drag forces on pickups can be divided into four parts. Which pressure drag occurs highest to 77 percentage, internal flow loss 10 percentage, under floor roughness 10 percentage and friction loss occurs around body car about 3 percentages [37].

2.3 Flow control

Flow control have been used for many years to control the fluid flow, and some employ different concepts to serve this purpose in last decades. The ability to manipulate a flow passively or actively is of immense technological importance [38]. Figure 2.2 below shows the different methods employed in controlling flows.

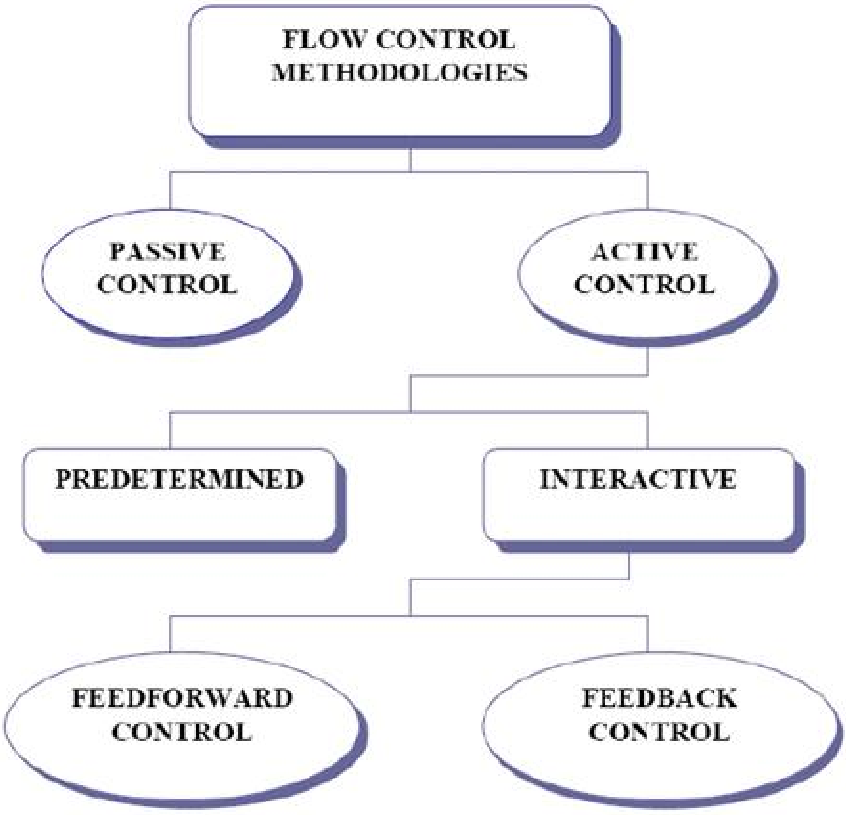

Figure 2.2. Flow control methods [38]

2.3.1 Active flow control

Active flow-control (AFC) is a fast-growing multidisciplinary science and technology aimed at altering a natural flow state or development path into a more desired state (or path). Active control schemes can be divided into predetermined or interactive methods. A predetermined method of control involves the introduction of steady or unsteady energy inputs without consideration for the state of the flow field. Examples of predetermined active flow control include jet vectoring using piezoelectric actuators and post stall lift enhancement and form drag reduction using oscillatory blowing. Predetermined open-loop control schemes can be very effective in modifying the flow field. In interactive methods of flow control, the power input to the actuator (controller) is continuously adjusted based on some form of measurement element (sensor). The control loop for interactive control can be either a feed forward (open) or feedback (closed) loop. In the feed forward control loop, the sensor is placed upstream of the actuator. Therefore, the measured flow field parameter and the controlled flow field parameter will differ as flow structures come over stationary sensors and actuators. Another classification scheme for flow control methods is to consider whether the technique is applied at the wall or away from it. Surface parameters that can influence the flow include roughness, shape, curvature, rigid-wall motion, compliance, temperature, and porosity. Heating and cooling of the surface can influence the flow via the resulting viscosity and density gradients. Mass transfer can take place through a porous wall or a wall with slots. Suction and injection of primary fluid can have significant effects on the flow field, influencing particularly the shape of the velocity profile near the wall and thus the boundary layer susceptibility to transition and separation. Different additives, such as polymers, surfactants, micro-bubbles, droplets, particles, dust or fibers, can also be injected through the surface in water or air wall-bounded flows. Control devices located away from the surface can also be beneficial. Large-eddy breakup devices (also called outer-layer devices, or OLDs), acoustic waves bombarding a shear layer from outside, additives introduced in the middle of a shear layer, manipulation of free stream turbulence levels and spectra, gust, and magneto-and electro-hydrodynamic body forces are examples of flow control strategies applied away from the wall.

An important point which we should emphasize is that, there are two primary advantages to active flow control that are not achievable by passive techniques. First, active flow control technology leverages and controls a natural stability of the flow to attain a large effect using small, localized energy input. Control is most effective when the control input is introduced locally at a high receptivity region. Secondly, active control can be used to control complex, dynamical processes like turbulence production in turbulent boundary layers to reduce skin friction, and hence viscous drag, where the reduction is proportional to the surface area covered by the actuators[38].

2.4 Control application

To successfully apply active flow control, several basic questions should be answered. First the control objective to be achieved is specified (e.g., increased lift). Secondly, the flow phenomenon to be controlled or leveraged is identified (e.g., boundary layer separation). Flow physics is key to scaling and determining influential parameters. An appropriate actuation strategy is then selected (e.g., predetermined open-loop control or feedback control). Finally, a range of operation for the key control parameters is determined (e.g., forcing frequency and amplitude)[38].

2.4.1 Control of jets

For the reasons like increasing mixing, reduce jet engine noise, and vector the jet thrust, there was a lot of interest in the control of jets by means of periodic perturbation. More recently the control of an axis symmetric free jet (ReUe = 6600) using a single synthetic jet was investigated experimentally (Tamburello & Amitay, 2008). The interaction was examined for a range of momentum coefficients, Strouhal numbers, and synthetic jet orientations (with respect to the main jet). The synthetic jet deflects the majority of the main jet flow away from it, while drawing some of the flow back toward it[38].

2.4.2 Transition control

Delaying laminar-to-turbulence transition of a boundary layer has many obvious advantages. Depending on the Reynolds number, the skin-friction drag in the laminar state can be as much as an order of magnitude less than that in the turbulent condition. For ground vehicle, the reduced drag means longer range, reduced fuel cost and volume, or increased speed. Flow-induced noise results from the pressure fluctuations in the turbulent boundary layer and, hence, is virtually nonexistent in the laminar case [40].

2.4.3 Separation control

Separation delay of a nominally two-dimensional attached boundary layer could be achieved by enhancing the averaged skin friction upstream of the mean separation region. Typically, simply and most effectively, increased skin friction could be achieved by enhanced near wall-outer/core flow (for external and internal flows, respectively) momentum transfer. At least three known methods exist to enhance near wall stream wise momentum: (1) add (high momentum fluid), (2) remove (low momentum fluid) or (3) re-distribute (momentum across the boundary layer). Emphasis should be placed on minimum energy expenditure in order to re-distribute momentum [39].

2.4.4 Wake vortex control

A wide variety of aerodynamic and hydrodynamic means for suppressing vortex shedding is classified into three categories in accordance with the phenomenological mechanism of vortex shedding. The three categories are as follows: (i) surface protrusions, which affect separation lines and/or separated shear layers, e.g. helical strakes, wires, fins, studs or spheres, etc.(ii) shrouds, which affect the entrainment layers, e.g. perforated, gauze, axial-rod, axial-slat, etc.;(iii) near wake stabilizers, which prevent interaction of entrainment layers, e.g. splitter plates, guiding vanes, base-bleed, slits cut across the cylinder, etc. Most means in the first two categories are omnidirectional, i.e. they are effective irrespective of the direction of fluid velocity. The importance of developing control methods for flow over 3D bodies such as a truck or bus is emphasized [41]. In this body type, vertical structures in the wake significantly change depending on the stream wise length of the body (which may determine the momentum thickness at separation), aspect ratio (i.e., height to width), body height from the ground, and so forth.

2.4.5 Drag reduction

Drag reduction is a subject that is explicitly or implicitly interwoven in every aspects of flow control. The practical benefits of achieving even a modest reduction in fluid resistance to moving bodies are enormous. There is no shortage of ideas on how to reduce the drag. Many challenges remain, however, when attempting to apply laboratory curiosities to real-life situations. For airplanes and submarines, streamlining has led to significant reduction in the pressure drag component attributed to separation. That is not the case for most land vehicles which, despite substantial improvement during the last few decades, are still more or less blunt bodies [42].

2.5 Passive flow control

The passive flow control system uses more or less discrete obstacles, added around or on the roof of the vehicle. They can be declined in two groups according to their influence on the flow control. The first group consists on obstacles positioned on the surface of the geometry. The second group consists of the obstacles positioned upstream or downstream of the geometry to be controlled [43]. the following are some example of passive flow control methods.

2.5.1 Effect of VG on aerodynamic drag

Vortex Generator is an aerodynamic surface which is basically a small vane that creates a vortex. van de Wijdeven and Katz [44] studied the surface pressure distribution and the trailing vortex signature behind the VGs of a generic model in a low speed wind tunnel. In order to delay the flow separation at the rear, bump-shaped VGs at the roof end of a cars is used. VGs themselves create drag, but they also reduce drag by preventing flow separation at downstream. The overall effect of VG was calculated by totaling the positive and negative effects.

2.5.2 Effect of spoiler on aerodynamic drag

The spoiler is used to minimize unfavorable air movement around the vehicle and can be divided into the front spoilers and the rear spoilers. The added spoiler can diffuse the airflow passing a vehicle, which minimizes the turbulence at the rear of the vehicle, adds more downward pressure to the back end and reduces lift acted on the rear trunk [45]. Park et al. [46] studied the flow around a simplified high-speed passenger car with a rear-spoiler.

2.5.3 Others add-on devices

Hahba et al. [47] numerically investigated the use of lateral guide vanes as a drag reducing device for ground vehicles. Two types of ground vehicles were considered, a simplified bus model and a simplified sport utility vehicle (SUV) model. The guide vanes were used to direct air into the low-pressure wake region in order to enhance pressure recovery, which in turn would reduce form drag and hence the overall aerodynamic drag. CFD simulations were used to assess the efficiency of the drag reducing device. The steady-state simulations were based on the RANS (Reynolds Averaged Navier Stock equations). Results of simulations indicated that an overall reduction in the aerodynamic drag coefficient is up to 18% for the bus and SUV models with lateral guide vanes.

2.6 Flow separation

Flow separation occurs (figure 2.3) when the velocity at the wall is zero or negative and an inflection point exists in the velocity profile, and a positive or adverse pressure gradient occurs in the direction of flow [48].

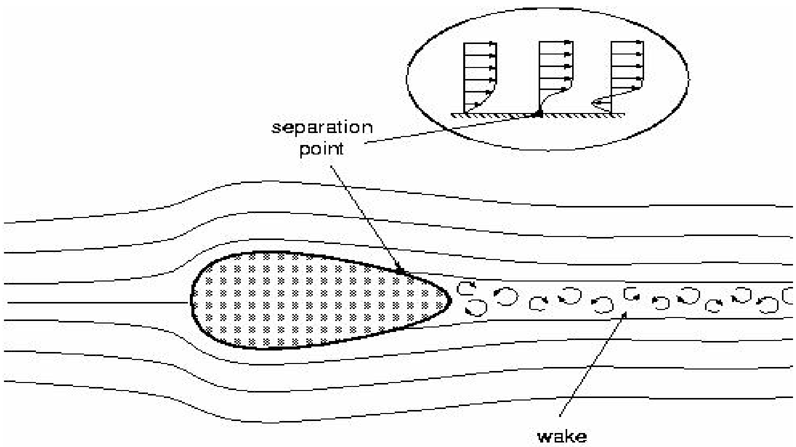

Figure 2.3. Flow separation [48]

2.6.1 Separation at sharp corners

Corners, sharp turns and high angles of attack all represent sharply decelerating flow situations where the loss in energy in the boundary layer ends up leading to separation. Here, the boundary layer flow is unable to follow the turn in the sharp corner (which would require a very rapid acceleration), causing separation at the edge and recirculation in the aft region of the backward facing step.

2.6.2 Flow around a truck

Flow over non-streamlined bodies such as trucks leads to considerable drag due to recirculation and separation zones. It can be seen from figure 2.4 that, a recirculation zone is on the back of the cab, and another one around the edge of the trailer box. The addition of air shields to the cab roof ahead of the trailer helps organize the flow around the trailer and minimize losses, reducing drag by up to 10-15% [48].

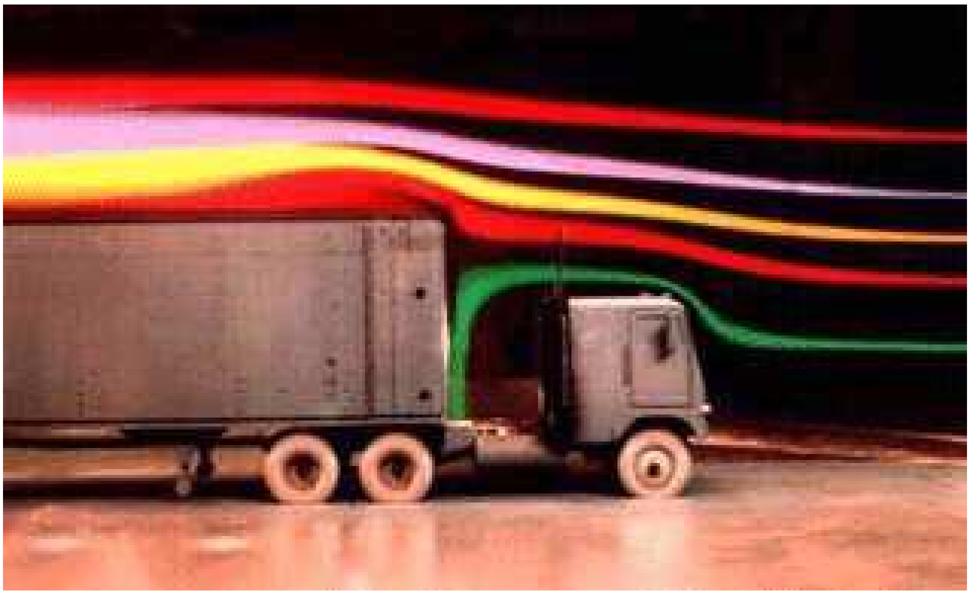

Figure 2.4. Flow over truck [48]

2.7 Ahmed Body

The generic Ahmed Body reference model has been chosen as the benchmark for carrying out computations for studying of the aerodynamic parameters. The body was first proposed by Ahmed et al. [49]. The Ahmed body is a very simple bluff body which has its shape simple enough to allow for accurate flow simulation but retains some important practical features relevant to automobile bodies. As shown on figure 2.5 it has a slant on its rear end, whose angle can be manipulated and the corresponding drag and lift coefficients calculated. This is done to exhibit the air flow over the different geometry sections of an automobile and in its vicinity, at different slant angles. This model portrays how to calculate the turbulent flow field around a simple car-like geometry using the turbulent flow, k-epsilon interface [50].

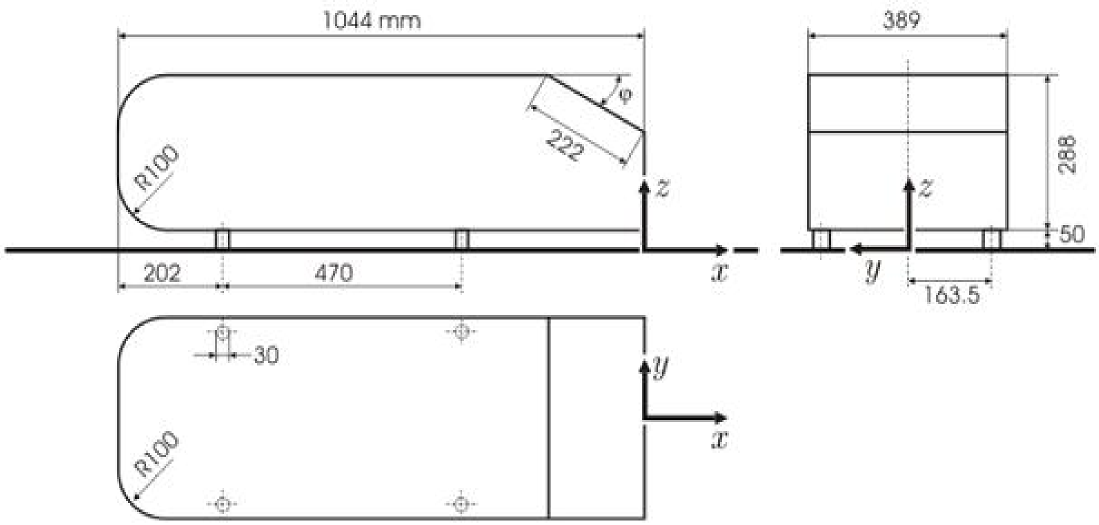

Figure 2.5. The original Ahmed body. Top view and side view for the standard (30°) slant angle as presented by Ahmed S.R. and Ramm G. [49]

2.8 Computational Fluid Dynamics

Computational fluid dynamics (CFD) uses numerical methods to solve and analyze problems that involve fluid flows. The governing equations and turbulence models have been solved with respect to the specified boundary conditions using the finite volume method as implemented in the commercial CFD code FLUENT.

There are three type of vehicle aerodynamic testing such as road testing, utilizing CFD tools and wind tunnel testing. Three main methods to analyzing fluid dynamic problems exist; theoretical, experimental, and numerical, which can also be referred to as computational fluid dynamics. The theoretical method can also be referred to as the analytical approach, which infers that the problem is solved using known mathematical equations. Since most fluid dynamic problems are complex and cannot be solved directly, assumptions must be made to employ this approach. The main advantage of the theoretical methodology is that "clean" general information is able to be solved for using simple formulas.

Experimental methods are often the primary approach for testing aerodynamic flow fields. Evaluating the performance of a scaled-down model of a prototype device is the main objective of the experimental method. Scaled-down models of the device are relatively inexpensive and therefore it is realistic for companies to use this method. One problem this method faces is that the wind tunnel facility must be able to produce the required free stream conditions which can be difficult to obtain, especially for cases that model large aircrafts or space vehicles.

As computers gained popularity a new method of solving complex fluid problems was developed called computational fluid dynamics. The governing equations of fluid motion, including the conservation of mass, momentum, and energy, usually in partial differential or integral form, are solved numerically using this approach to predict the fluid flow. With computational methods few assumptions are needed and a high-speed computer is utilized to solve the resulting governing equations for the fluid dynamic problem. Advantages of this method are that the user is not constrained to linear problems, complicated problems can be solved, and time evolution of flow can be obtained. There are disadvantages to this method which include boundary condition problems and the high costs of a computer that is able to run the complex problems. As CFD becomes more prevalent in industrial applications the disadvantages decrease due to cheaper computers and turbulence models able to reduce boundary condition issues [51].

There are three components in CFD analysis; the pre-processor, the solver, and the post-processor. The inter-dependency between these components can clearly be seen in figure 2.6. Preprocessor is defined as a program that processes input data to produce output that is used as an input to the processor. Any CAD software like Solidworks can be used as a preprocessor. The solution of the flow is later solved at the center of each of these volumes by the solver. The preprocessor also defines general surface types (for example - inlet/outlet areas) to regions of the domain.

The solver discretizes the differential equations converting them to algebraic equations that can be solved numerically using the finite volume method. The finite volume method is discussed subsequently in this chapter in further detail. Finally, the post-processor is a tool that allows the interpretation of the solution in the form of graphs, plots, and charts.

FLUENT can be used for both the solver and the post-processor. Microsoft Excel can also be used as a post processor for making graphs and charts [52].

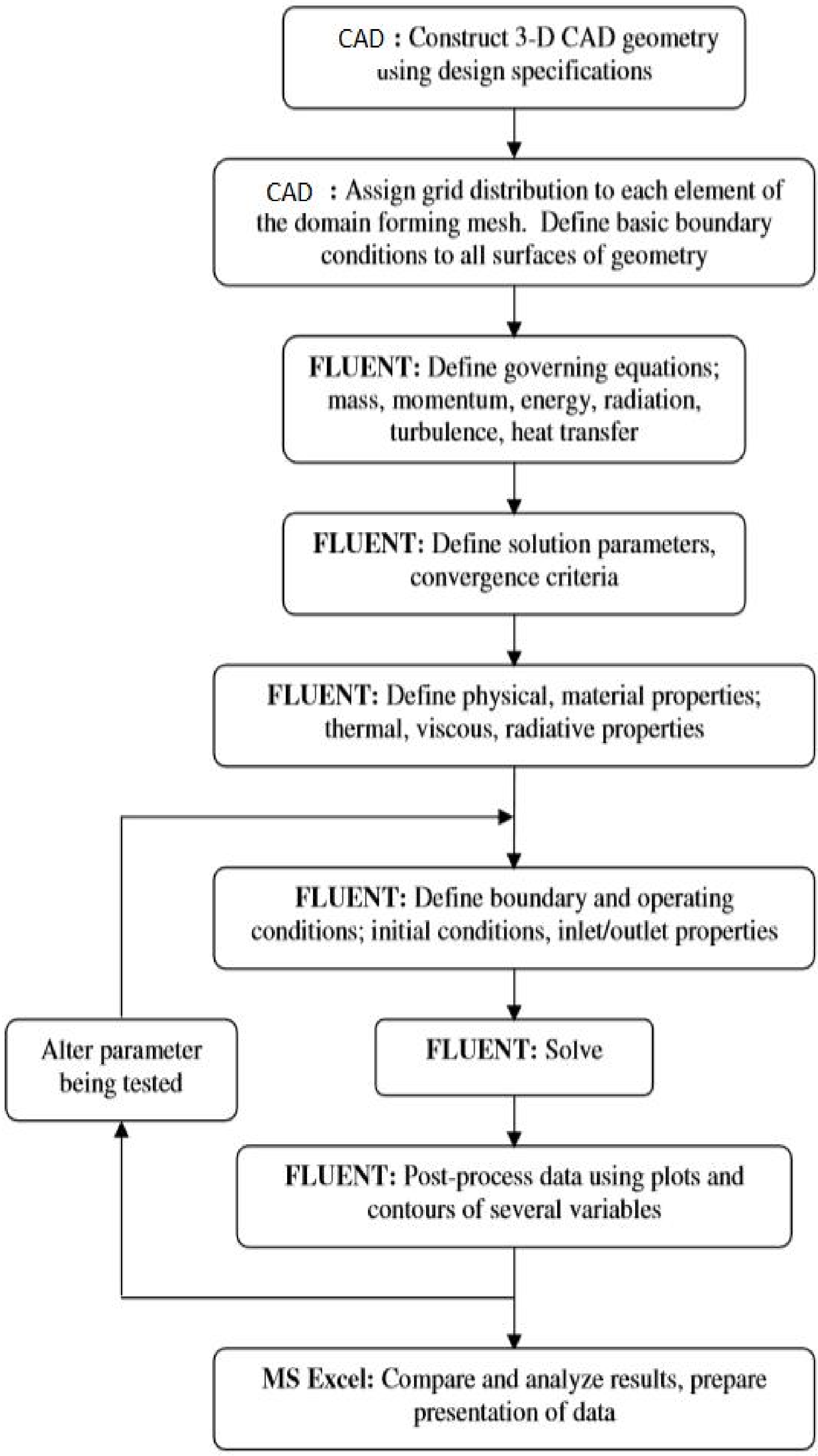

Figure 2.6. Flowchart of method used for CFD application [52]

2.9 Numerical Models

2.9.1 Basic Model and Assumptions

Assumptions

The numerical model is based on the following assumptions:

- the flow is steady, turbulent and three-dimensional;
- the flow is single phase, i.e., the effects of dust particles and/or water vapor have been neglected;
- the velocity is uniform over the vent inlet
- the air properties are constant, except for the density change with temperature, which has been treated using the Boussinesq Approximation[52].

2.9.2 Governing Equations

The flows being considered involve mechanically induced flow (air entering thought a vent) and buoyant forces that drive the air motion in the domain considered. An important factor in the flow calculations is taking into consideration the buoyant forces (natural convective flow) that arise due to differences in fluid density due to temperature difference. The air flow can be considered incompressible as the velocities are low (air flows can usually be considered incompressible if the Mach number is less than roughly 0.3 or about 100m/s). Also, air being a Newtonian fluid displays a linear relationship between shear and strain rate. The laws of conservation of mass (continuity) and momentum are used to describe the flow based on the assumptions discussed[52].

The four equations below are Navier Stokes equations in the x, y and z

directions and the continuity equation which describes the flow.

Momentum in x-direction

$$\frac{\partial}{\partial t}(\rho u) + \frac{\partial}{\partial x}(\rho uu) + \frac{\partial}{\partial y}(\rho vu) + \frac{\partial}{\partial z}(\rho wu) = -\frac{\partial P}{\partial x} + \mu\left(\frac{\partial^2 u}{\partial x^2} + \frac{\partial^2 u}{\partial y^2} + \frac{\partial^2 u}{\partial z^2}\right) \quad \text{.......... (2.1)}$$

Momentum in y direction

$$\frac{\partial}{\partial t}(\rho v) + \frac{\partial}{\partial x}(\rho uv) + \frac{\partial}{\partial y}(\rho vv) + \frac{\partial}{\partial z}(\rho wv) = -\frac{\partial P}{\partial y} + \mu\left(\frac{\partial^2 v}{\partial x^2} + \frac{\partial^2 v}{\partial y^2} + \frac{\partial^2 v}{\partial z^2}\right) - \rho g \beta (T_\infty - T) \quad \text{........ (2.2)}$$

Momentum in z direction

$$\frac{\partial}{\partial t}(\rho w) + \frac{\partial}{\partial x}(\rho u w) + \frac{\partial}{\partial y}(\rho v w) + \frac{\partial}{\partial z}(\rho w w) = -\frac{\partial P}{\partial z} + \mu\left(\frac{\partial^2 w}{\partial x^2} + \frac{\partial^2 w}{\partial y^2} + \frac{\partial^2 w}{\partial z^2}\right) \ldots\ldots (2.3)$$

Continuity

$$\frac{\partial}{\partial x}(\rho u) + \frac{\partial}{\partial y}(\rho v) + \frac{\partial}{\partial z}(\rho w) = 0 \ldots\ldots (2.4)$$

The y-axis of the Cartesian coordinate system is aligned in the vertical direction as shown in Figure 2.7 below. u, v and w are the velocity components in the x, y and z directions respectively, ρ is the mass density, μ is the viscosity and β is the thermal expansion coefficient of air, t is time, T is the temperature, P is the pressure, and g is the gravitational acceleration. The Boussinesq approximation was used and therefore fluid properties were assumed constant except for the density change with temperature which leads to the buoyancy forces. The density change is assumed to be proportional to the temperature difference.

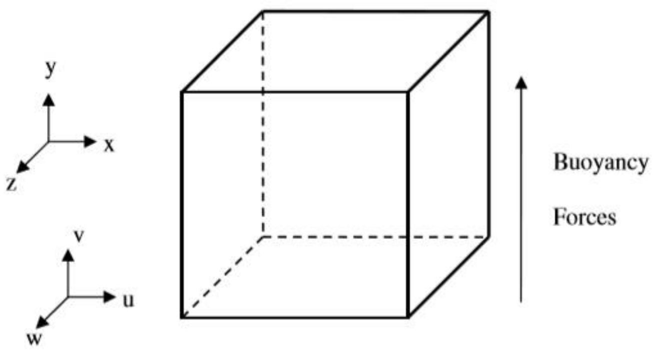

Figure 2.7. Buoyancy Force

The equation of continuity simply states that mass is conserved or that the net accumulation of mass in the control volume is zero in steady flow. Each term in the continuity equation represents the net mass flow through a face perpendicular to one of the respective axes. Because the y direction equation contains a temperature dependent term, a necessary addition to the Navier Stokes equations is the energy equation. Because of the assumptions being used, the conservation of energy equation is:

$$\frac{\partial}{\partial t}(\rho C_p T) + \frac{\partial}{\partial x}(\rho u C_p T) + \frac{\partial}{\partial y}(\rho v C_p T) + \frac{\partial}{\partial z}(\rho w C_p T) = K\left(\frac{\partial^2 T}{\partial x^2} + \frac{\partial^2 T}{\partial y^2} + \frac{\partial^2 T}{\partial z^2}\right) + q''' \quad (2.5)$$

where C_p is the specific heat (J/kgK), and K is the conductivity (W/m K) of the fluid and q''' is the rate of internal heat generation.

The above two Equations describe the flow and temperature distributions. For turbulent flow, the velocity and temperature vary with time.

2.10 Turbulence Models

Velocity fields characterize Turbulent flows. These fluctuations mix transported quantities such as momentum, energy, and species concentration, and cause the transported quantities to fluctuate as well. Since these fluctuations can be of small scale and high frequency, they are too computationally expensive to simulate directly in practical engineering calculations. Instead, the instantaneous (exact) governing equations can be time-averaged, ensemble-averaged, or otherwise manipulated to remove the small scales, resulting in a modified set of equations that are computationally less expensive to solve. However, the modified equations contain additional unknown variables, and turbulence models are needed to determine these variables in terms of known quantities[52].

No single turbulence model can be universally applied to all situations. Some consideration must be taken when choosing a turbulence model including; physics encompassed in the flow; level of accuracy; and computation resources available. Both the Realizable and RNG (Renormalization Group) K-Epsilon models along with the standard K-epsilon turbulence models were explained. The standard and Shear Stress Transport variations of the K-Omega turbulence model were examined, as well as, the Detached Eddy Simulation (DES) model and the Large Eddy Simulation (LES) model.

The equations of motion are averaged with respect to time and these turbulent transport models predict the effect of turbulence on the time averaged mean motion. Since all of the terms currently in the equations of motion are instantaneous values, they are replaced with the sum of a time-mean quantity and a fluctuating quantity. (for instance, $T = \overline{T} + T'$). A new set of equations of motion with the same form are obtained with the addition of these quantities.

Energy

$$\frac{\partial}{\partial t}(\rho c_p \overline{T}) + \frac{\partial}{\partial x}(\rho \overline{u} c_p \overline{T}) + \frac{\partial}{\partial y}(\rho \overline{v} c_p \overline{T}) + \frac{\partial}{\partial t}(\rho \overline{w} c_p \overline{T})$$

$$= K\left(\frac{\partial^2 \overline{T}}{\partial x^2} + \frac{\partial^2 \overline{T}}{\partial y^2} + \frac{\partial^2 \overline{T}}{\partial z^2}\right) - \frac{\partial}{\partial x_i}\left(\rho c_p \overline{T \grave{U}_l}\right) + \dot{q} \ldots\ldots.. (26)$$

Momentum in x direction

$$\frac{\partial}{\partial t}(\rho\bar{u}) + \frac{\partial}{\partial x}(\rho\overline{uu}) + \frac{\partial}{\partial y}(\rho\overline{uv}) + \frac{\partial}{\partial z}(\rho\overline{uw}) = \frac{\partial\bar{P}}{\partial x} + \mu\left(\frac{\partial^2\bar{u}}{\partial x^2} + \frac{\partial^2\bar{u}}{\partial y^2} + \frac{\partial^2\bar{u}}{\partial z^2}\right) - \frac{\partial}{\partial x_i}\left(\rho\overline{u\grave{U}_l}\right)(2.7)$$

Momentum in y direction

$$\frac{\partial}{\partial t}(\rho\bar{v}) + \frac{\partial}{\partial x}(\rho\overline{uv}) + \frac{\partial}{\partial y}(\rho\overline{vv}) + \frac{\partial}{\partial z}(\rho\overline{vw})$$

$$= -\frac{\partial\bar{P}}{\partial x} + \mu\left(\frac{\partial^2\bar{v}}{\partial x^2} + \frac{\partial^2\bar{v}}{\partial y^2} + \frac{\partial^2\bar{v}}{\partial z^2}\right) - \frac{\partial}{\partial x_i}\left(\rho\overline{v\grave{U}_l}\right) - \rho g\beta(\overline{T_\infty} - \bar{T}) \ldots\ldots\ldots (2.8)$$

Momentum in z direction

$$\frac{\partial}{\partial t}(\rho\bar{w}) + \frac{\partial}{\partial x}(\rho\overline{uw}) + \frac{\partial}{\partial y}(\rho\overline{vw}) + \frac{\partial}{\partial z}(\rho\overline{ww}) = \frac{\partial\bar{P}}{\partial z} + \mu\left(\frac{\partial^2\bar{w}}{\partial x^2} + \frac{\partial^2\bar{w}}{\partial y^2} + \frac{\partial^2\bar{w}}{\partial z^2}\right) - \frac{\partial}{\partial x_i}\left(\rho\overline{w\grave{U}_l}\right) \ldots\ldots (2.9)$$

Continuity

$$\frac{\partial}{\partial x}(\rho u) + \frac{\partial}{\partial y}(\rho v) + \frac{\partial}{\partial z}(\rho w) = 0 \ldots\ldots\ldots\ldots\ldots\ldots\ldots\ldots\ldots\ldots\ldots (2.10)$$

2.10.1 K-Epsilon Turbulence Model

The K-Epsilon model has become one of the most widely used turbulence models as it provides robustness, economy and reasonable accuracy for a wide range of turbulent flows. Improvements have been made to the standard model which improves its performance and two variants are available in Fluent; the RNG (renormalization group) model and the realizable model. Three versions of the K-Epsilon model will be investigated here. The standard, RNG, and realizable models have similar form with transport equations for k and ε. The two transport equations independently solve for the turbulent velocity and length scales. The main differences between the three models are as follows[52]:

- The turbulent Prandtl Numbers governing the turbulent diffusion of k and ε

- The generation and destruction terms in the equation for ε
- The method of calculating turbulent viscosity

Standard K-Epsilon Turbulence Model

This original model was initially proposed by Launder and Spalding [53]. For this model the transport equation for k is derived from the exact equation, but the transport for ε was obtained using physical reasoning and is therefore similar to the mathematically derived transport equation of k, but is not exact. The turbulent kinetic energy k, and its rate of dissipation ε, for this model are obtained by the following equations.

$$\frac{\partial}{\partial t}(\rho k)+\frac{\partial}{\partial x_i}(\rho k u_i)=\frac{\partial}{\partial x_j}\left[(\mu+\frac{\mu_i}{\sigma_k})\frac{\partial k}{\partial x_j}\right]+G_k+G_b+\rho\epsilon-Y_m+S_k\text{........ (2.11)}$$

$$\frac{\partial}{\partial t}(\rho\epsilon)+\frac{\partial}{\partial x_i}(\rho\varepsilon u_i)=\frac{\partial}{\partial x_j}\left[(\mu+\frac{\mu_i}{\sigma_\varepsilon})\frac{\partial\varepsilon}{\partial x_j}\right]+C_{1\varepsilon}\frac{\varepsilon}{k}(G_k+C_{3\varepsilon}G_b)-C_{2\varepsilon}\rho\frac{\varepsilon^2}{k}+S_\varepsilon\text{..... (2.12)}$$

where Gk represents the generation of turbulent kinetic energy the arises due to mean velocity gradients, Gb is the generation of turbulent kinetic energy that arises due to buoyancy, and M Y represents the fluctuating dilation in compressible turbulence that contributes to the overall dissipation rate. $S_\varepsilon$and S_k are source terms defined by the user. $C_{1\varepsilon}$, $C_{2\varepsilon}$ and C_μ are constants that have been determined experimentally and are taken to have the following values;

$C_{1\varepsilon}$=1.44, $C_{2\varepsilon}$=1.92, C_μ=0.09

σ_ε and σ_k are turbulent Prandtl numbers for the turbulent kinetic energy and its dissipation rate. These have also been derived experimentally and are defined as follows.

σ_ε=1.3, σ_k=1.0

The turbulent (or eddy) viscosity at each point is related to the local values of turbulent kinetic energy and its dissipation rate by;

$$\mu_t=\rho C_\mu\frac{k^2}{\varepsilon}\text{... ....(2.13)}$$

The term for the production of turbulent kinetic energy G_k is common in many of the turbulence models studied and is defined as

$$G_k = -\rho\overline{u_i' u_j'}\frac{\partial u_j}{\partial x_i} \ldots\ldots\ldots\ldots\ldots\ldots\ldots\ldots\ldots\ldots\ldots\ldots\ldots (2.14)$$

The modulus of mean rate-of-strain tensor, S is defined as

$$S = \sqrt{2S_{ij}S_{ij}} \ldots\ldots\ldots\ldots\ldots\ldots\ldots\ldots\ldots\ldots\ldots\ldots\ldots (2.15)$$

The generation of turbulent kinetic energy that arises due to buoyancy, Gb is defined as follows

$$G_b = \beta g_i \frac{\mu_i}{Pr_i}\frac{\partial T}{\partial x_i} \ldots\ldots\ldots\ldots\ldots\ldots\ldots\ldots\ldots\ldots\ldots\ldots (2.16)$$

As the present study uses relatively low velocities, the dilation dissipation term, Y_m which accounts for turbulence from compressibility effects is defined as

$$Y_m = 2\rho\varepsilon M_t^2 \ldots\ldots\ldots\ldots\ldots\ldots\ldots\ldots\ldots\ldots\ldots\ldots\ldots (2.17)$$

RNG K-Epsilon Turbulence Model

Similar to the standard k-epsilon model, the RNG model was derived from the instantaneous Navier Stokes equations, except it uses a technique called renormalization group theory described by Yakhot and Orszag [54]. This derivation produces a model with different constants to those used in the standard k-epsilon model and also adds new terms to the transport equations for the turbulent kinetic energy and its dissipation. The effect of swirl is also accounted for in the RNG model enhancing the accuracy of swirling flows. An analytical formula for turbulent Prandtl numbers is provided in this model while the standard model relies on user-specific constant values. Finally, assuming appropriate treatment of the near wall region, the RNG model uses an analytically derived differential formula for the effective turbulent viscosity which accounts for low Reynolds number flows. The RNG K-Epsilon model is therefore more accurate and more reliable than the standard K-Epsilon model for a wider range of flows.

As a result, from these differences, the transport equations appear as follows.

$$\frac{\partial}{\partial t}(\rho k) + \frac{\partial}{\partial x_i}(\rho k u_i) = \frac{\partial}{\partial x_j}\left[\alpha_k \mu_{eff}\frac{\partial k}{\partial x_j}\right] + G_k + G_b + \rho\epsilon - Y_m + S_k \ldots\ldots (2.18)$$

$$\frac{\partial}{\partial t}(\rho\epsilon) + \frac{\partial}{\partial x_i}(\rho\varepsilon u_i) = \frac{\partial}{\partial x_j}\left[(\alpha_\varepsilon \mu_{eff}\frac{\partial \varepsilon}{\partial x_j}\right] + C_{1\varepsilon}\frac{\varepsilon}{k}(G_k + C_{3\varepsilon}G_b) - C_{2\varepsilon}\rho\frac{\varepsilon^2}{k} - R_\varepsilon + S_\varepsilon (2.19)$$

where Gk represents the generation of turbulent kinetic energy that arises due to mean velocity gradients, Gb is generation of turbulent kinetic energy the arises due to buoyancy, and Y_m represents the fluctuating dilation in compressible turbulence that contributes to the overall dissipation rate. S_ε and S_k are source terms defined by the user. α_k and α_ε are inverse effective Prandtl numbers for the turbulent kinetic energy and its dissipation.

The RNG theory uses a scale elimination procedure that defines the effective viscosity given in the following equation.

$$d\left(\frac{\rho^2 k}{\sqrt{\mu\varepsilon}}\right) = 1.72\frac{\hat{v}}{\sqrt{\hat{v}^3 - 1 + C_v}}d\hat{v} \quad (2.20)$$

where $\hat{v} = \mu_{eff}/\mu$ and C_v is a constant equal approximately to 100. This equation incorporates the ability to accurately define how the effective turbulent transport varies with effective Reynolds number to obtain more accurate results for low-Re flows and near-wall flows. For high Reynolds numbers, the effective viscosity is defined by the following ratio;

$$\mu_t = \rho C_\mu \frac{k^2}{\varepsilon} \quad (2.21)$$

Although this is similar to the turbulent viscosity of the standard model, the constant C_μ is derived using the RNG theory and found to be 0.0845 which is very close to the value used in the standard model (i.e., 0.09).

$C_{1\varepsilon}$ and $C_{2\varepsilon}$ are constants that have been derived analytically by the RNG theory and are defined as follows.

$C_{1\varepsilon} = 1.42,\ C_{2\varepsilon} = 1.68$

Realizable K-Epsilon Turbulence Model

The Realizable model by Shih [55] is the most recently developed of the three K-Epsilon variations and features two main differences from the standard K-Epsilon model. It uses a new equation for the turbulent viscosity and the dissipation rate transport equation has been derived from the equation for the transport of the mean-square vorticity fluctuation. The form of the eddy viscosity (turbulent) equations is based on the realizability constraints; the positivity of normal Reynolds stresses and Schwarz' inequality for turbulent shear stresses (i.e., certain mathematical constraints on the normal stresses are satisfied). This is not satisfied by either the standard or the RNG K-Epsilon models which makes the realizable model more precise than both models at predicting flows such as separated flows and flows with complex secondary flow features.

In terms of the improved changes by Shih (1995), the transport equations become:

$$\frac{\partial}{\partial t}(\rho k) + \frac{\partial}{\partial x_j}(\rho k u_j) = \frac{\partial}{\partial x_j}\left[(\mu + \frac{\mu_t}{\sigma_k})\frac{\partial k}{\partial x_j}\right] + G_k + G_b - \rho\epsilon - Y_m + S_k \ldots\ldots (2.22)$$

$$\frac{\partial}{\partial t}(\rho \epsilon) + \frac{\partial}{\partial x_j}(\rho \varepsilon u_j) = \frac{\partial}{\partial x_j}\left[(\mu + \frac{\mu_t}{\sigma_\varepsilon})\frac{\partial \varepsilon}{\partial x_j}\right] + \rho S \varepsilon C_1 - \rho C_2 \frac{\varepsilon}{k+\sqrt{v\varepsilon}} + C_{1\varepsilon}\frac{\varepsilon}{k} C_{3\varepsilon} G_b + S_\varepsilon \ldots (2.23)$$

where Gk represents the generation of turbulent kinetic energy the arises due to mean velocity gradients, Gb is generation of turbulent kinetic energy the arises due to buoyancy, and Y_m represents the fluctuating dilation in compressible turbulence that contributes to the overall dissipation rate. S_ε and S_k are source terms defined by the user. $\alpha_k \, and \, \alpha_\varepsilon$ are the turbulent Prandtl numbers for the turbulent kinetic energy and its dissipation.

Similar to the previous variations of the K-Epsilon models, the turbulent viscosity is determined by the formula given below; however, it produces different results as C_μ is not constant.

$$\mu_t = \rho C_\mu \frac{k^2}{\varepsilon} \ldots\ldots\ldots\ldots\ldots\ldots\ldots\ldots\ldots\ldots\ldots\ldots\ldots\ldots (2.24)$$

Where C_μ is computed from

$$C_\mu = \frac{1}{A_0 + A_s \frac{KU^*}{\varepsilon}} \ldots\ldots\ldots\ldots\ldots\ldots\ldots\ldots\ldots\ldots\ldots\ldots\ldots\ldots (2.25)$$

Where

$$U^* = \sqrt{S_{ij}S_{ij} + \widetilde{\Omega_{ij}}\widetilde{\Omega_{ij}}} \text{ and } \widetilde{\Omega_{ij}} = \overline{\Omega_{ij}} - \varepsilon_{ijk}\omega_k - 2\varepsilon_{ijk}\omega_k \ldots\ldots\ldots (2.26)$$

In the above equation, $\overline{\Omega_{ij}}$ is the mean rate of rotation tensor viewed in a rotating reference frame with angular velocity ω_k. The constants $A_0 \, and \, A_s$ are defined as;

$A_0 = 4.04$, $A_s = \sqrt{6} cos\phi$

Where

$$\phi = \frac{1}{3}cos^{-1}\left(\sqrt{6}\frac{S_{ij}S_{jk}S_{ki}}{\tilde{S}^3}\right), \tilde{S} = \sqrt{S_{ij}S_{ij}}\ , S_{ij} = \frac{1}{2}\left(\frac{\partial u_j}{\partial x_i} + \frac{\partial u_i}{\partial x_j}\right) \qquad (2.27)$$

It has been shown that C_μ is a function of the mean strain and rotational rates, the angular velocity of the rotating system, and the turbulent kinetic energy and its dissipation rate. The standard value of C_μ =0.09 is found to be the solution of equation 2.32 for an inertial sub layer in the equilibrium boundary layer.

The constants $C_{1\varepsilon}$, C_2,. $\alpha_k and\ \alpha_\varepsilon$ have been determined by Shih [55] and are defined as follows.

$C_{1\varepsilon} = 1.44,\ C_2 = 1.9, \quad \alpha_k = 1.0 and\ \alpha_\varepsilon = 1.2$

K-Omega Turbulence Model

The second turbulence model to be investigated is the K-Omega turbulence model. The K-Omega model has two variations that will both be described in this section; the standard K-Omega model, and the shear stress transport (SST) model[56]. Both of these models use similar transport equations for k and ω but the SST model differs from the standard model as follows:

- There is a gradual change from the standard k-omega model in the inner region of the boundary layer to the k-epsilon model in the outer part of the boundary layer.
- In order to account for the transport effects of the principal turbulent shear stresses the SST model incorporates a modified turbulent viscosity equation

Standard K-Omega Turbulence Model

FLUENT uses a standard K-Omega model developed by Wilcox [56] that was formulated to better compute Low-Reynolds number effects, compressibility, and shear flow spreading. The standard model is an empirical based model with transport equations for turbulent kinetic energy (k) and its specific dissipation rate (ω).

$$\frac{\partial}{\partial t}(\rho k) + \frac{\partial}{\partial x_i}(\rho k u_i) = \frac{\partial}{\partial x_i}\left[(\mu + \frac{\mu_t}{\sigma_k})\frac{\partial k}{\partial x_j}\right] + G_k - Y_k + S_k \qquad (2.28)$$

$$\frac{\partial}{\partial t}(\rho \omega) + \frac{\partial}{\partial x_i}(\rho \omega u_i) = \frac{\partial}{\partial x_j}\left[(\mu + \frac{\mu_t}{\sigma_\omega})\frac{\partial \omega}{\partial x_j}\right] + G_\omega - Y_\omega + S_\omega \qquad (2.29)$$

where Gk represents the generation of turbulent kinetic energy the arises due to mean velocity gradients and G_ω is generation of ω which are defined in the exact manor as the K-Epsilon model. Y_k and Y_ω represent the dissipation of k and ω due to turbulence. σ_k and σ_ω are the turbulent Prandtl numbers (constants in this case; equal to 2) for k and ω respectively and $S_\varepsilon$andS_k are source terms defined by the user.

The turbulent viscosity is defined using a damping coefficient (α^*);

$$\mu_t = \alpha^* \frac{\rho k}{\omega} \quad \text{(2.30)}$$

The low-Reynolds number correlation is obtained from this coefficient α^* which damps the turbulent viscosity. This coefficient is given by,

$$\alpha^* = \alpha^*_\infty \left(\frac{\alpha^*_0 + {Re_t}/{R_k}}{1 + {Re_t}/{R_k}} \right) \quad \text{(2.31)}$$

Where $Re_t = \frac{\rho k}{\mu\omega}$, $R_k = 6$, $\alpha^*_0 = {\beta_i}/{3}$ and $\beta_i = 0.072$. for the high –Re form of the standard k-omega model, $\alpha^* = \alpha^*_\infty = 1$

The term for the dissipation of k due to turbulence, Y_k is defined as

$$Y_k = \rho \beta^* f_{\beta^*} k \omega$$

and the term for the dissipation of ω due to turbulence, Y_ω is defined as

$$Y_\omega = \rho \beta f_\beta \omega^2$$

this k-omega model was developed by Wilcox [56] has shown comparable results for far wakes, mixing layers and various jet types which make it applicable to wall bounded flows and free shear flows. It incorporates modifications for compressibility, shear flow spreading, and low-Re number effects.

SST K-Omega Turbulence Model

The shear stress transport K-Omega model is the only variation of the standard k-omega model available in FLUENT. It was developed by Menter [57] using the standard k-omega model and a transformed k-epsilon model. The main difference is the way in which the model calculates the turbulent viscosity to account for the transport of the principal turbulent shear stress. This model also incorporates a cross-diffusion term in the ω equation and a blending function to allow proper calculation of the near-wall and far-field areas. The blending function triggers the standard K-Omega model in near wall regions, and triggers the K-Epsilon-like model in areas away from the surface. These differences make the SST model more precise for a larger variety of flows than the standard model.

Similar to the standard K-Omega model, the transport equations for k and ω are slightly modified and are given by;

$$\frac{\partial}{\partial t}(\rho k)+\frac{\partial}{\partial x_i}(\rho k u_i)=\frac{\partial}{\partial x_j}\left[(\mu+\frac{\mu_t}{\sigma_k})\frac{\partial k}{\partial x_j}\right]+\widetilde{G_k}-Y_k+S_k \text{…………….. (2.32)}$$

$$\frac{\partial}{\partial t}(\rho \omega)+\frac{\partial}{\partial x_i}(\rho \omega u_i)=\frac{\partial}{\partial x_j}\left[(\mu+\frac{\mu_t}{\sigma_\omega})\frac{\partial \omega}{\partial x_j}\right]+G_\omega-Y_\omega+D_\omega+S_\omega \text{……. (2.33)}$$

where $\widetilde{G_k}$ represents the generation of turbulent kinetic energy the arises due to mean velocity gradients, G_ω is generation of ω, and Y_k and Y_ω represent the dissipation of k and ω due to turbulence. σ_k and σ_ω are the turbulent Prandtl numbers for k and ω respectively and S_ε and S_k are source terms defined by the user. D_ω is the cross diffusion term which will be described below.

The term for production of turbulent kinetic energy, $\widetilde{G_k}$ is determined slightly differently from the other models and is defined as

$$\widetilde{G_k}=\min(G_k, 10\rho\beta^* k\omega)$$

Where G_k is defined the same way as described in the previous models.

The term for the production of ω , G_ω is defined as

$$G_\omega=\frac{\alpha}{v_t}G_k \text{………………………………………….. (2.34)}$$

The terms for the dissipation of k and ω due to turbulence, Y_k and Y_ω, are defined in a similar manner to that used in the standard model with the main difference being that f_{β^*} and f_β are both considered constants with a value of 1.

the turbulent viscosity is computed in a different way from that used in the standard model and is given by;

$$\mu_t = \frac{\rho k}{\omega} \frac{1}{max\left[\frac{1}{\alpha^*}, \frac{SF_2}{a_1 \omega}\right]} \quad \ldots\ldots\ldots\ldots\ldots\ldots (2.35)$$

where S is the strain rate magnitude. The turbulent Prandtl numbers which were constant in the standard model are equated below and incorporate the blending functions F1 and F2. Blending functions have been added to the SST model to ensure that the model equations behave appropriately in both near wall and far field zones.

$$\alpha_k = \frac{1}{F1/\alpha_{k,1} + (1-F1)/\alpha_{k,2}} \quad \ldots\ldots\ldots\ldots\ldots\ldots (2.36)$$

$$\alpha_\omega = \frac{1}{F1/\alpha_{w,1} + (1-F1)/\alpha_{w,2}} \quad \ldots\ldots\ldots\ldots\ldots\ldots (2.37)$$

Where;

$F_1 = \tanh(\Phi_1^4)$ $\quad$ $F_2 = \tanh(\Phi_2^2)$

The cross-diffusion term, D_ω blends the standard k-epsilon model and the standard k-omega model and is defined as

$$D_\omega = 2(1 - F_1)\rho\sigma_{\omega,2} \frac{1}{\omega} \frac{\partial k}{\partial x_i} \frac{\partial \omega}{\partial x_j} \quad \ldots\ldots\ldots\ldots\ldots\ldots (2.38)$$

The constants specific to the SST k-omega model are defined as

$\sigma_{\omega,1} = 2.0$, $\sigma_{\omega,2} = 1.168$, $\sigma_{k,2} = 1.0$, $\sigma_{k,1} = 1.176$ and $\sigma_1 = 0.31$

Summary

Analyzing flow around a vehicle using CFD/ANSYS has shown better and dependable results. Analysis in Improving drag and lift coefficients for various vehicles with different types of add-on devices have been carried out using CFD/ANSYS Fluent. Most of the literatures cited in this work focused mainly on sedans, SUVs and trucks. However, the literatures available on pickup vehicles are very limited and the ones available hardly used spoilers. Some have investigated effect of add-on devices and have also conducted wind tunnel experiments. But, still it is not analyzed enough because till now the aerodynamic drag on pickup vehicles is high. With high drag coefficient and versatility of pickup vehicles reducing the amount of drag is of immense importance.

CHAPTER THREE

MATERIALS AND METHODOLOGY

In this chapter the materials used to work on the study and the methodologies employed are discussed. Because this study focused mainly on CFD analysis which was done using ANSYS Fluent, the materials used were mainly of softwares.

3.1 Materials

The softwares used in this study were:

SOLIDWORKS: Used to construct the baseline and the pickup vehicle models, and the spoilers.

ANSYS fluent: Used to simulate the air flow around the pickup truck and calculate the drag and lift coefficients.

Microsoft excel: Used to draw graph using ANSYS output as input.

3.2 Methodology

3.2.1 Baseline Model

Extended cab Toyota pickup vehicle model was used for the present work. The model represents a 1:12 scale of the full-scale pickup vehicle. The model was designed with a smooth underbody, enclosed wheel wells, with no side view mirrors and without openings for cooling airflow. The model used has been modified to resemble the generic pickup vehicle in [13]. Schematics of the pickup truck model with the pertinent dimensions are depicted in Appendix.

3.2.2 Bench marking the baseline model

From the given data, the baseline model of extended cab 1/12 scaled down pickup vehicle model was generated using SolidWorks. The dimensions of the body which are almost considered for aerodynamic analysis were bench marked for the study. These dimensions give the basic geometry of the vehicle. The modeled vehicle shown in figure 3.1 below was selected as the baseline for studying the aerodynamic performances.

The length of the model is 0.432 m, the width is 0.152 m, and the height is 0.1488 m. A coordinate system is attached to the front tip of the vehicle in the symmetry plane.

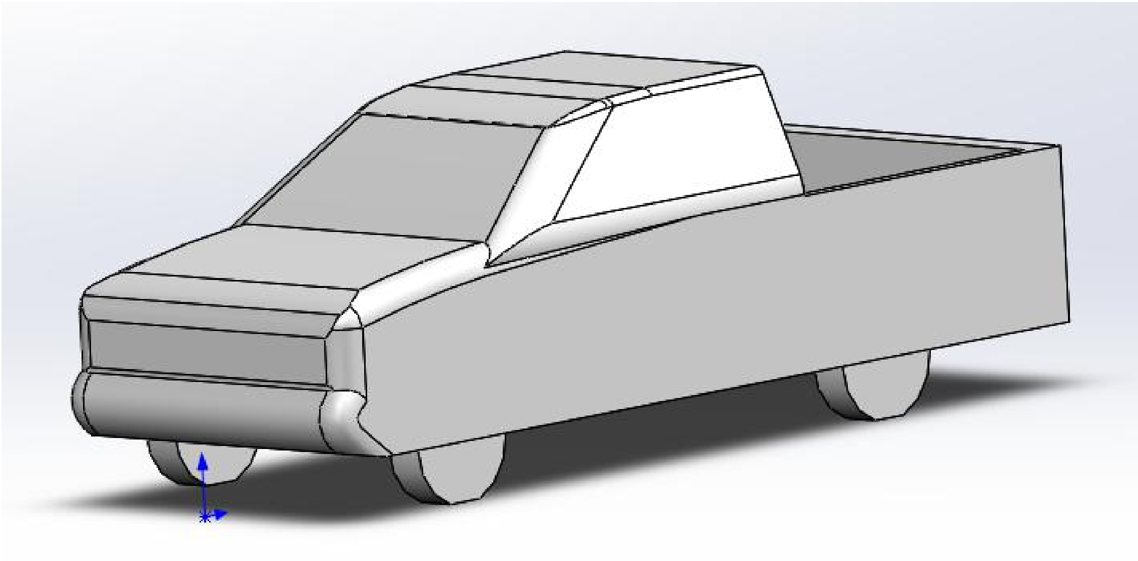

Figure 3.1. 1/12 pickup vehicle model

Criteria for selecting generic extended cab pickup vehicle (baseline model)

- Many government and private organizations are using extended cab pickup vehicles for various purposes, and these vehicles make many trips to different parts of our country.
- Most of the trips made are of high speed.
- The other criteria for selecting generic pickup vehicle is for validation purpose.

3.2.3 Aerodynamic drag reducing device

In this study one drag reducing device with different arrangement is employed and each arrangement are simulated using Ansys Fluent, and their values are compared with each other and to the baseline.

Rear spoiler which is externally attached to the rear end of the roof, is meant to push the flow separation a bit rearward and reduce the amount of drag by minimizing the wake region, and by throwing the turbulent air behind the truck. The spoiler will minimize the amount of swirling air in the bed of the vehicle.

The arrangements are such that, for model one (figure 3.2) the spoiler with 21mm slant length is attached to the rear end of the cab at an angle of zero-degree inclination. In the second model (figure 3.3), the spoiler with 21mm slant height is inclined upward at 12 degree. Only the slant length of the spoiler is reduced to 11mm keeping the inclination angle at zero degree in the third model (figure 3.4).

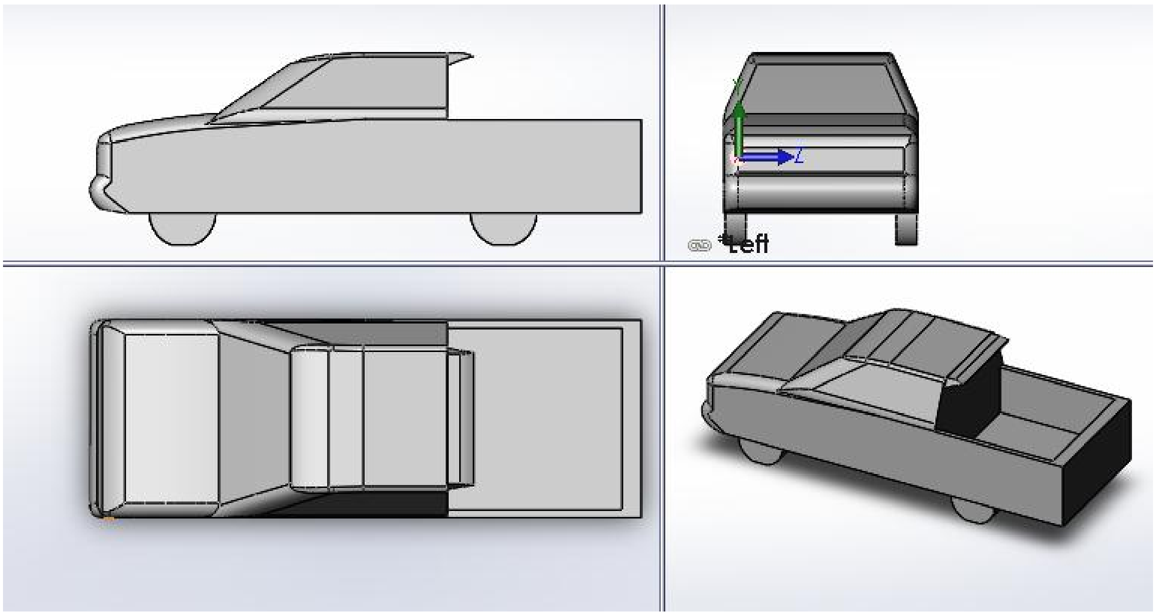

Figure 3.2. Model 1

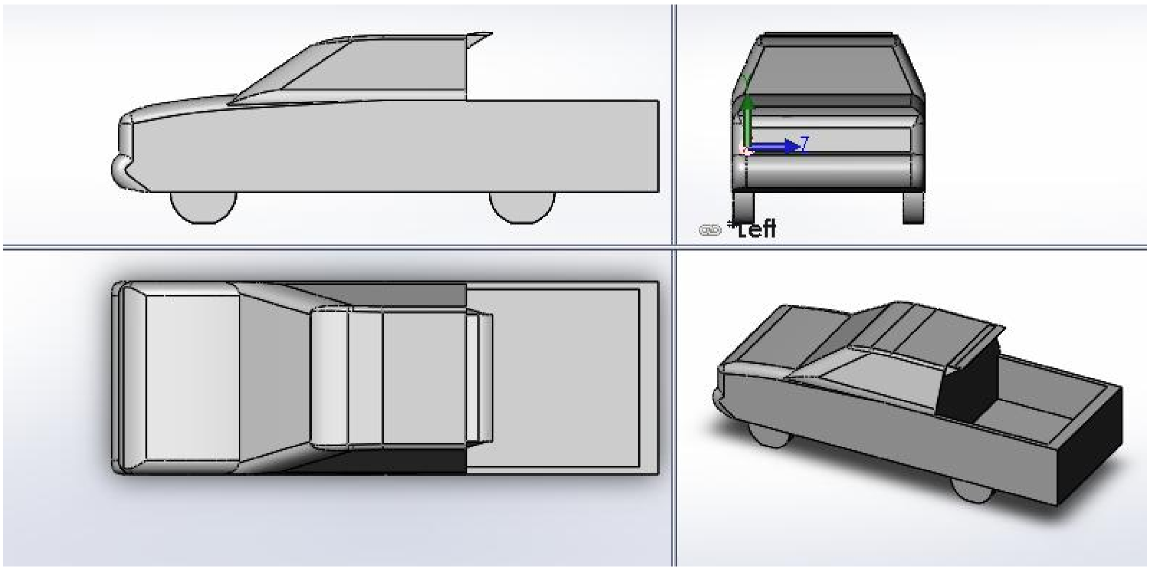

Figure 3.3. Model 2

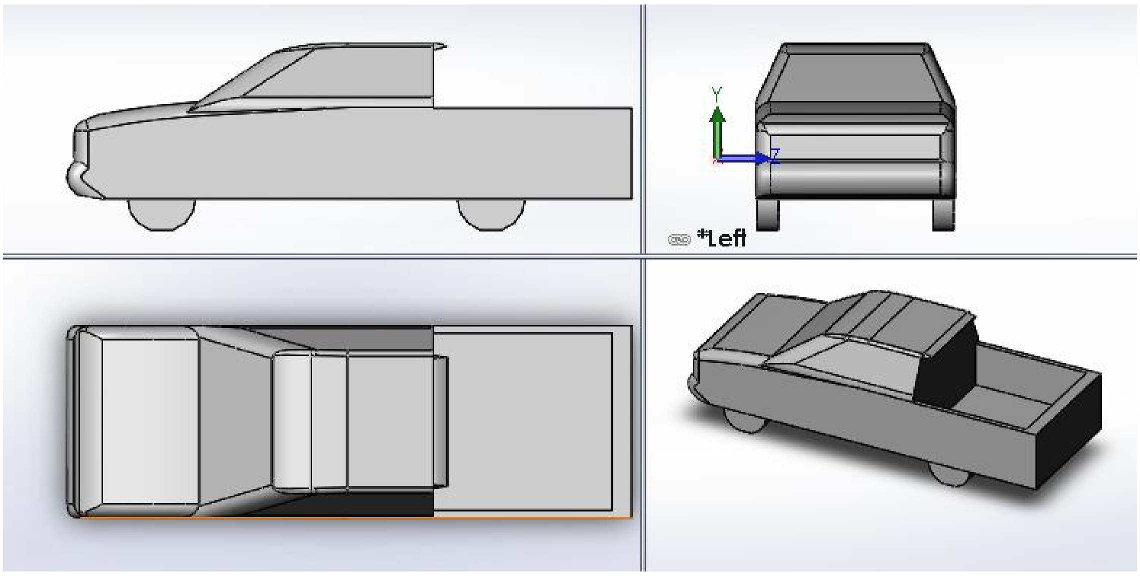

Figure 3.4. Model 3

The spoiler airfoil shape was selected from NACA catalogue. NACA6409 airfoil was selected and the coordinates are imported to SolidWorks for modelling. Then to increase its length rectangular feature was added and was connected with the baseline vehicle. For the first and second model the spoiler with 21mm length is named as the long spoiler as shown in figure 3.5, whereas the spoiler used in the third model(11mm) is named short spoiler (figure 3.6).

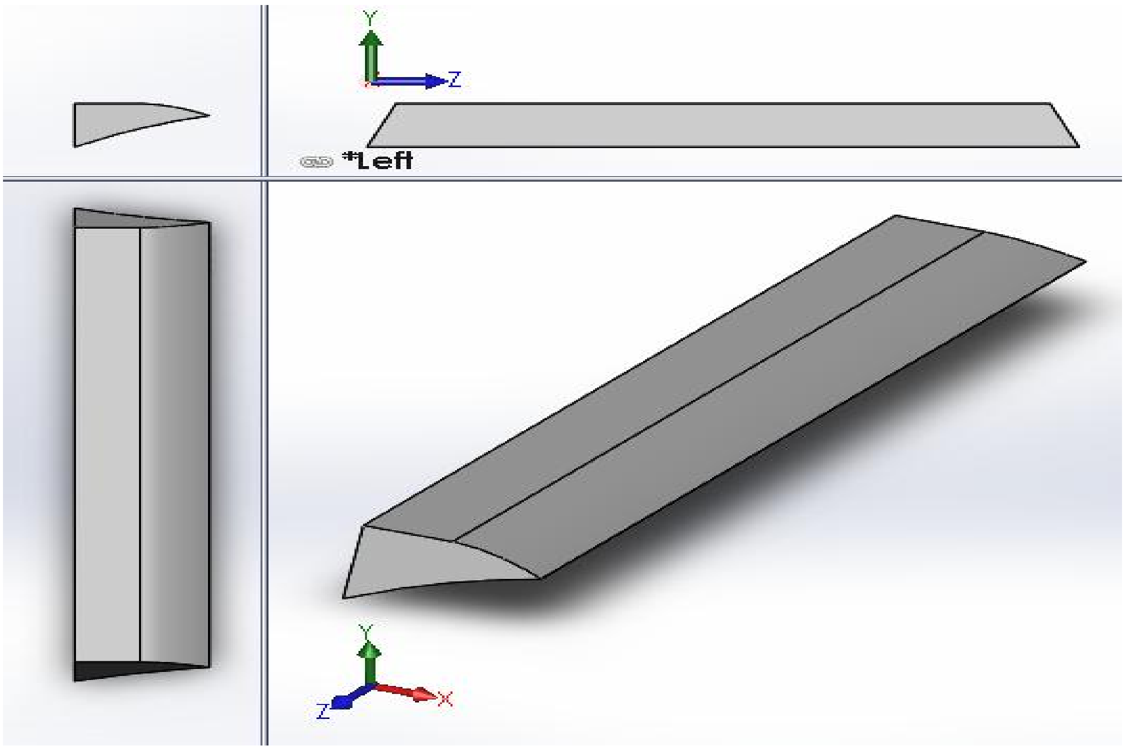

Figure 3.5. Long Spoiler

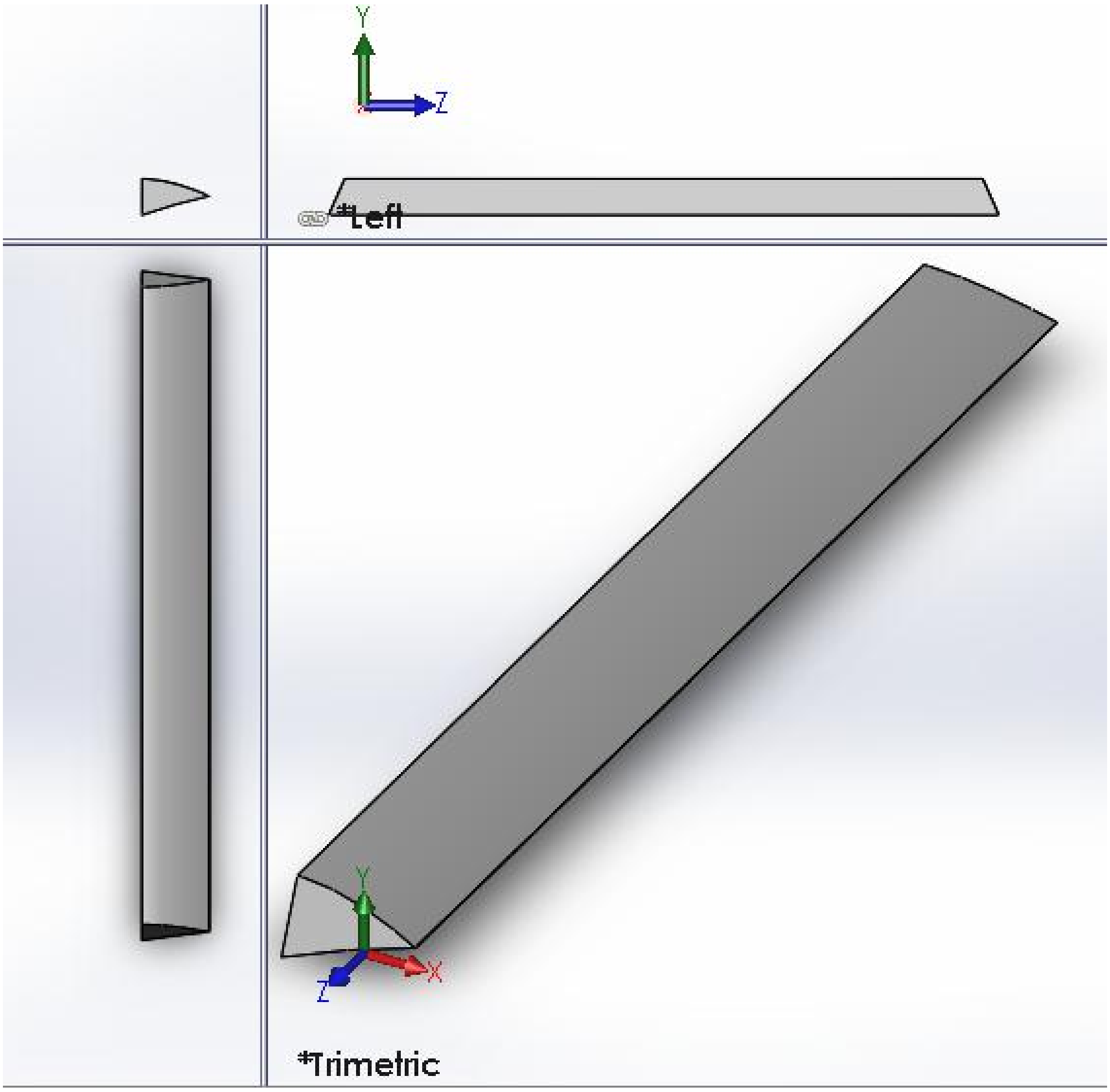

Figure 3.6. Short Spoiler

3.2.4 Turbulence Modeling.

In this study Realizable k-ε Turbulence Model (RKE) described in the turbulence modelling section was used. The solver used for the analysis is ANSYS 17.0 and it uses a control-volume method to solve the governing equations that can be solved numerically. The solver selected was the pressure based implicit solver. In this type the equations of continuity and momentum are solved sequentially. The flow is considered to be incompressible and steady in nature and the equations are solved using both first and second order upwind method.

Reasons for selecting Realizable k-ε Turbulence Model (RKE)

The realizable k-ε model is a relatively recent development and differs from the standard k-ε model in two important ways:

- The realizable k-ε model contains a new formulation for the turbulent viscosity.
- A new transport equation for the dissipation rate, ε, has been derived from an exact equation for the transport of the mean-square vorticity fluctuation.

The term "realizable" means that the model satisfies certain mathematical constraints on the Reynolds stresses, consistent with the physics of turbulent flows. Neither the standard k-ε model nor the RNG k-ε model is realizable.

An immediate benefit of the realizable k- ε model is that it more accurately predicts the spreading rate of both planar and round jets. It is also likely to provide superior performance for flows involving rotation, boundary layers under strong adverse pressure gradients, separation, and recirculation.

Both the realizable and RNG k- ε models have shown substantial improvements over the standard k- ε model where the flow features include strong streamline curvature, vortices, and rotation. Since the model is still relatively new, it is not clear in exactly which instances the realizable k- ε model consistently outperforms the RNG model. However, initial studies have shown that the realizable model provides the best performance of all the k- ε model versions for several validations of separated flows and flows with complex secondary flow features.

One limitation of the realizable k- ε model is that it produces non-physical turbulent viscosities in situations when the computational domain contains both rotating and stationary fluid zones [52].

3.3 CFD/ANSYS Fluent set up and procedure

ANSYS Fluent was used as the CFD software and it simulated the fluid flow around the CAD models which were generated using SolidWorks. The simulation process was divided into four separate sections such Geometry generation, Meshing, Setup, and Solution. For all simulations, for models with and without the drag reducing devices, the process was the same.

3.3.1 Geometry Generation

The first Step on the fluent setup was to define the geometry that would be modeled by CAD software to represent the air neighboring the pickup vehicle. After the vehicle model was uploaded an enclosure was generated surrounding it. For experimental study the enclosure was designed based on recommendation from Fluent for accurate results. Marco [58], suggests that the dimensions of the computational domain should be at least 3 car lengths in front of the car, and 5 lengths behind. Dimensions used for the enclosure are given in Table 3.1 below. In order to control the volume mesh near the car, an inner box may be helpful. This box should extend about half a car length in front, to the sides and to the top, and about a car length in the wake. The wind tunnel and computational domain around the vehicle is shown in figure 3.7.

Table 3.1. Dimensions for Wind Tunnel and Computational Domain

Dimension for wind tunnel enclosure			
Upstream length	Downstream length	Width	Height
1701mm	2268mm	1296mm	1296mm
Dimension for computational domain (Inner Box)			
Upstream length	Downstream length	width	height
216mm	648mm	292mm	365mm

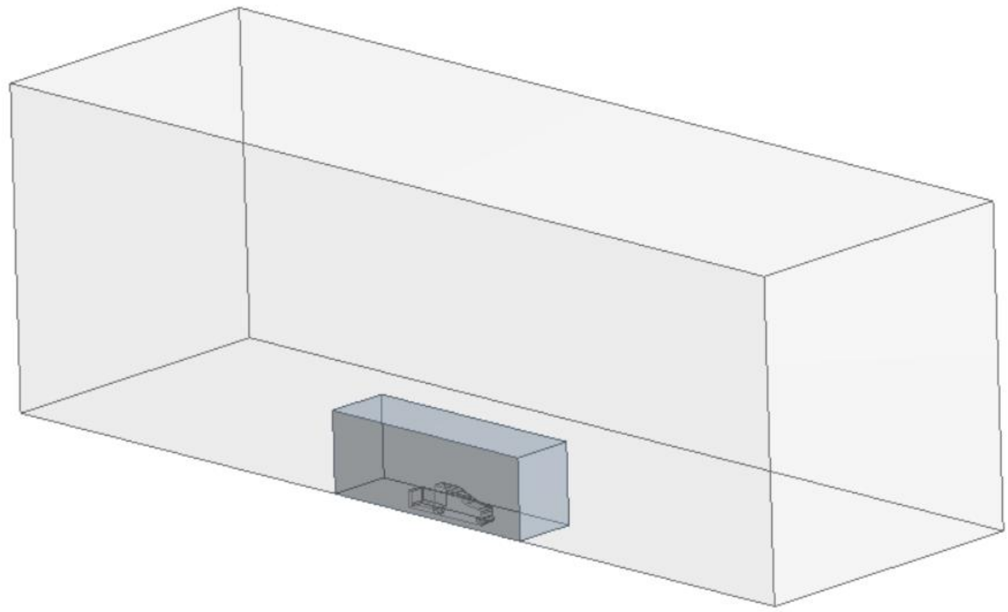

Figure 3.7. Model in Wind tunnel and Computational Domain

After the wind tunnel enclosure was constructed Boolean was created to subtract the volume of the generic vehicle from the volume of enclosure to create a new volume that represented only the air that surrounded the vehicle.

3.3.2 Meshing

Once the Boolean was created the Geometry Setup was completed and then meshing started. Tetrahedral and triangular mesh types were developed in this study. Just off the vehicle surface with exception of underbody and wheels cells of prismatic layers were developed. For best meshing, the inner box body sizing was 10mm element length and face sizing of 10mm was used on the vehicle. The fineness of the entire mesh is described by relevance used. Relevance of 100 means high accuracy and low speed of processing, while a relevance of -100 means low accuracy and higher speed of processing. For this study zero relevance with fine relevance center was used. The advanced size function is proximity and curvature, used for the progression from minimum size elements, near and around the curvature of the vehicle to maximum size elements far away from the vehicle toward the walls of the wind tunnel box. High Smoothing which increases the number of smoothing iterations and improving element quality by moving nodes and elements in the vicinity was used. Meshed baseline model and model one are shown in figure 3.8 and 3.9. Detailed meshing inputs are mentioned in table 6.1, 6.2, 6.3 and 6.4 in appendix C.

Lastly, named sections were created to differentiate among the faces, which is also used to establish the properties of each face. The plane in front of the vehicle was the velocity inlet while the plane behind was the pressure outlet. The side attached to the vehicle is the symmetry whereas the side far from the vehicle was named symmetry-side. The top face was named symmetry-top and the bottom face road. The car and the road were included in the program-controlled inflation. After creating the named sections, the fluid flow simulation was carried out.

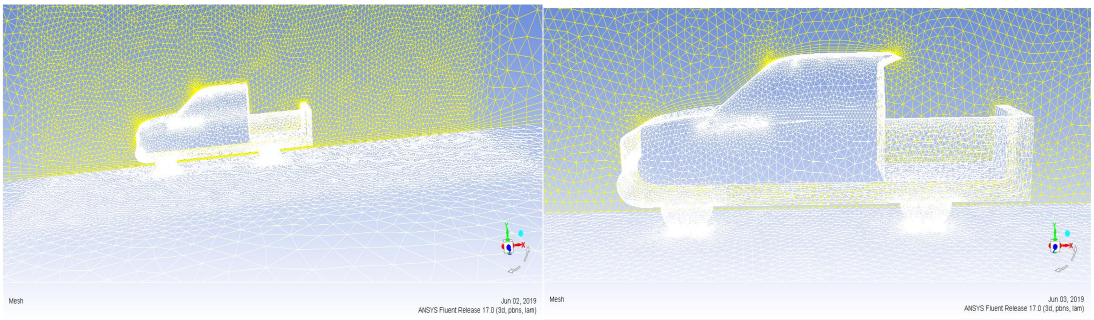

Figure 3.8. Baseline and Model 1 Mesh

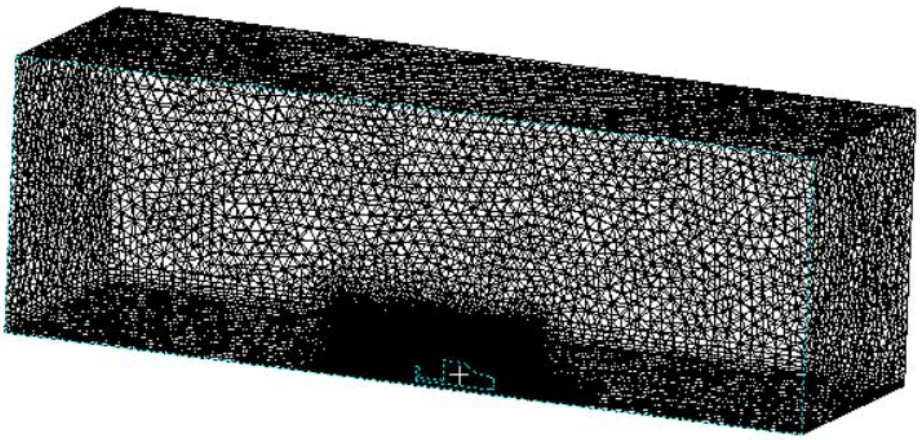

Figure 3.9. Baseline model meshed inside wind tunnel

3.3.3 Fluent setup and simulation procedure

Realizable k-ε model was employed in the fluent simulations for all models. The simulations were run with a velocity of 80kmph, 100kmph and 120kmph. In the simulation the air flew from the velocity-inlet towards the pressure-outlet with a selected amount of velocity. The turbulence intensity for the velocity inlet was reduced to 1%. Turbulence intensity can be defined as the root-mean-square of the velocity fluctuations over the mean flow velocity. A turbulence intensity of 1% is relatively low meaning steady air flow and the velocity introduced to the simulation had very low fluctuations and therefore very little turbulence. The area of each specific model was found using Fluent project area feature and was utilized in determining the drag coefficient of the vehicle model from the force that was calculated during the simulation. A coupled scheme was chosen for the pressure-velocity coupling. This scheme is more robust and efficient than other schemes for steady-state flows, such as the flow in this study. While employing a coupled scheme the flow Courant number was set to 50 while both the explicit relaxation factors for momentum and pressure was 0.25. The flow Courant number is the ratio between the computational distance step and the distance a disturbance travels in one-time step. Reducing this value improves the accuracy and steadiness of the simulation. The reduction in the explicit relaxation factors allowed for a more skewed mesh to be converged easier. They represent the percent of the solution being used from iteration to iteration throughout the simulation. The turbulent viscosity relaxation factor was set to 0.8 during first upwind and changed to 0.95 for second upwind. In order to monitor the calculations and simulations a monitor was created for drag, lift, moment and scaled residuals on the vehicle. Once the monitor was created it could be used to set the convergence criterion for the simulation. The convergence was set to none. The numerical computation was first started with the first order scheme to ensure numerical stability. After one hundred iterations, the numerical scheme was switched to the second order scheme for better numerical accuracy. This scheme was continued for another 500 iterations. Most of the scaled residuals and the global aerodynamic quantities such as the drag coefficient and the lift coefficient converged to 1e-3 long way before the 600^{th} iteration. Grid adaptations were carried out a few times based on the variations of the gradient of the total pressure, the variations of the gradient of the static pressure, and the y+ values on vehicle surfaces. The grid adaptation based on the variations of the gradient of the total pressure adds cells mainly in the vehicle wake region; the grid adaptation based on the variations of the gradient of static pressure adds cells in the stagnation point region and some additional cells in the vehicle wake region; and the grid adaptation based on the y+ value adds cells in regions near the vehicle surfaces. Also, y+ values at the vehicle surfaces were also checked to confirm that they fell into a range for which the wall-functions are valid and thus the turbulent wall boundary conditions used in the analysis and the numerical results of the analysis based on these boundary conditions are consistent with each other. In the cases studied, the wall y+ values were mainly in the range of 50 to 300, and wall-functions were indeed valid.

Once this convergence was met the simulation was complete and was stopped. Once convergence was reached the solution could be analyzed to determine the effectiveness of the spoilers. After the simulations were complete the post-CFD part of Fluent and Excel were utilized to fully analyze the solution and the air flow around the vehicle and spoiler. Contours of the pressure, turbulence, velocity magnitudes, and graphs were created.

CHAPTER FOUR

RESULT AND DISCUSSION

In this chapter the results of the baseline model, Model one, Model two, and Model three simulations with the help of figures and tables are depicted. Each results are briefly discussed.

4.1 Baseline Model

4.1.1 Results

Result of scaled residuals, drag and lift coefficient, pressure and velocity contour at speed of 80kmph 100kmph and 120kmph of model one which is the baseline model is depicted below.

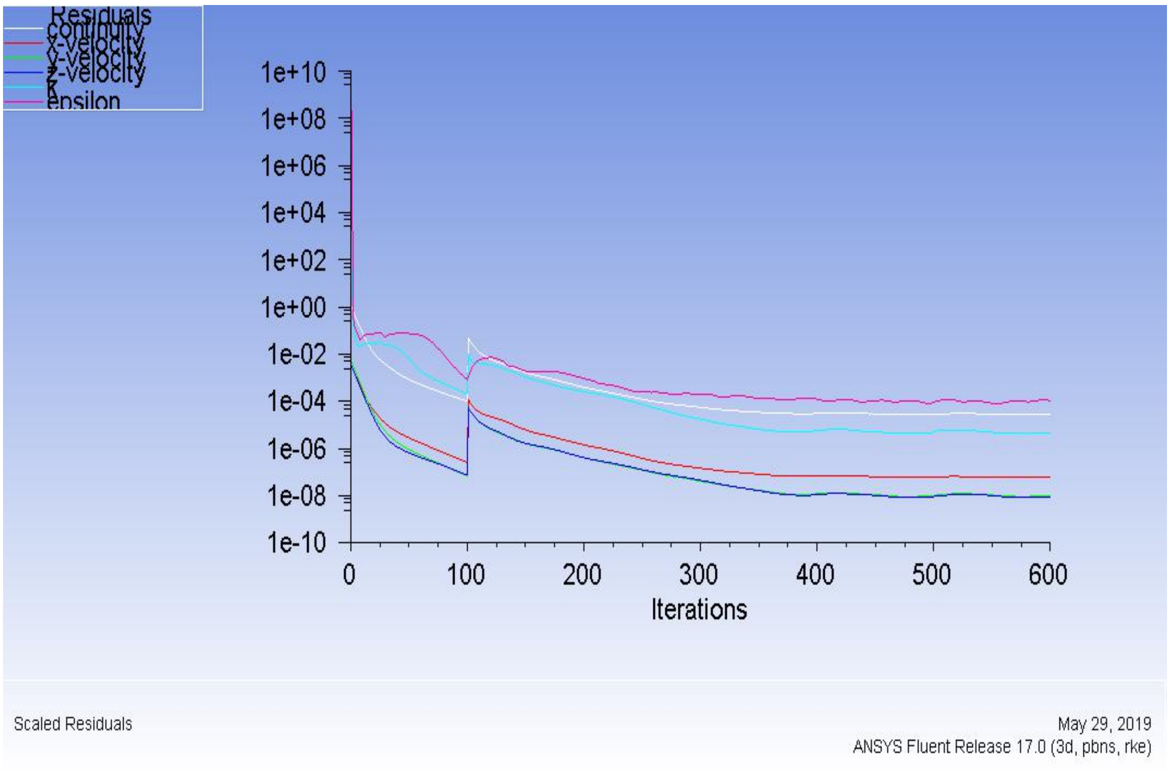

Figure 4.1. Scaled Residuals

The scaled residual for baseline model at 80kmph, 100kmph and 120kmph shows how the parameters converge with each iteration. It can be seen on figure 4.1 that how the graph changes after the 100th iteration. Here at the 100th iteration the scheme was changed from first order upwind to second order upwind.

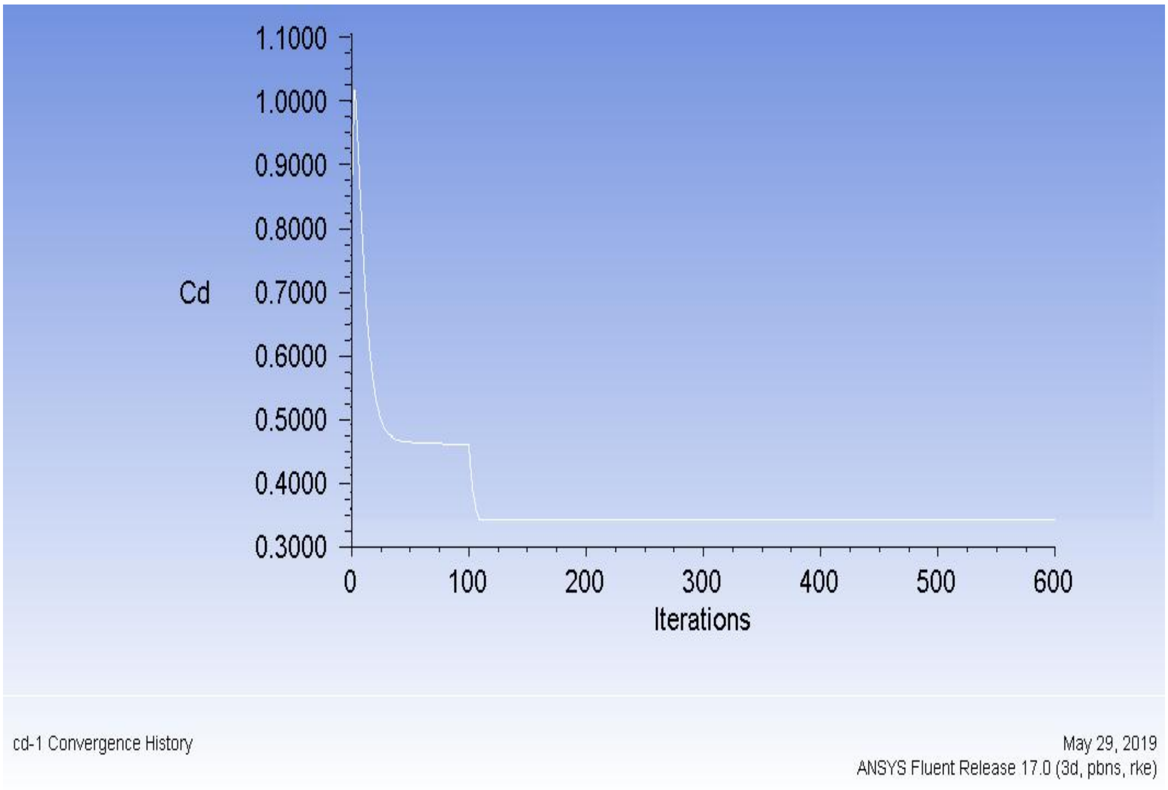

Figure 4.2. Drag coefficient of baseline model at 80kmph

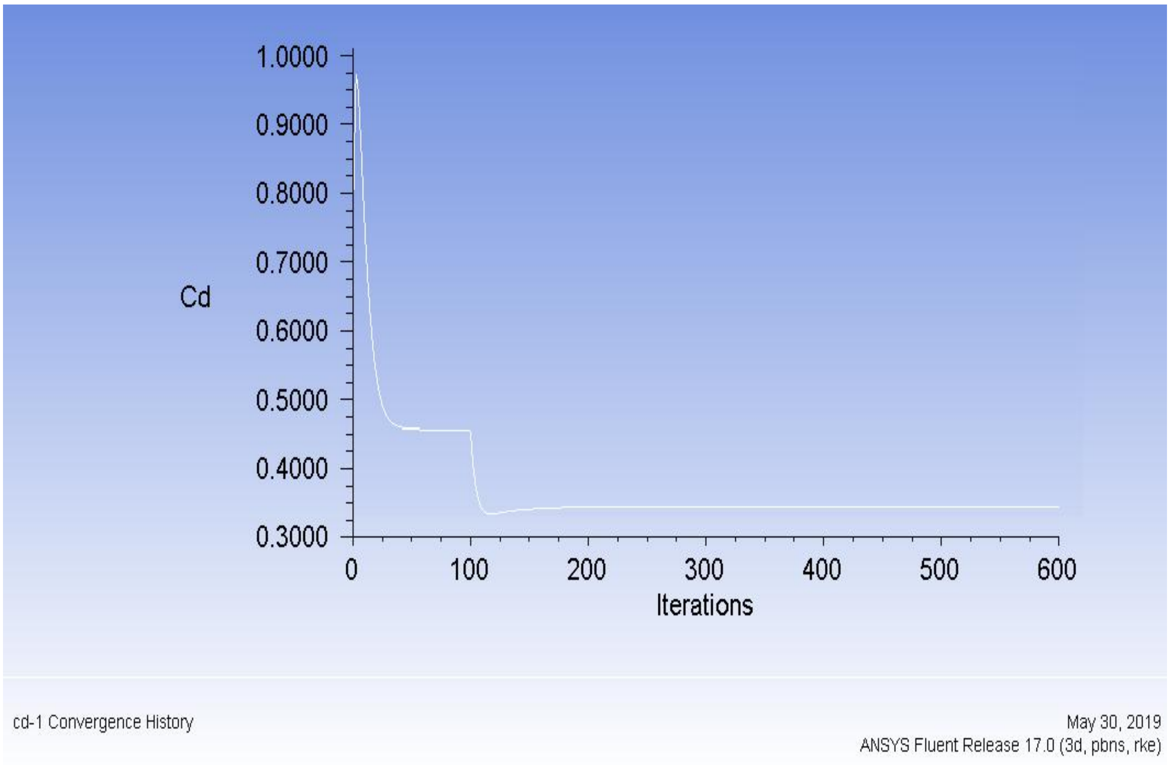

Figure 4.3. Drag coefficient of baseline model at 100kmph

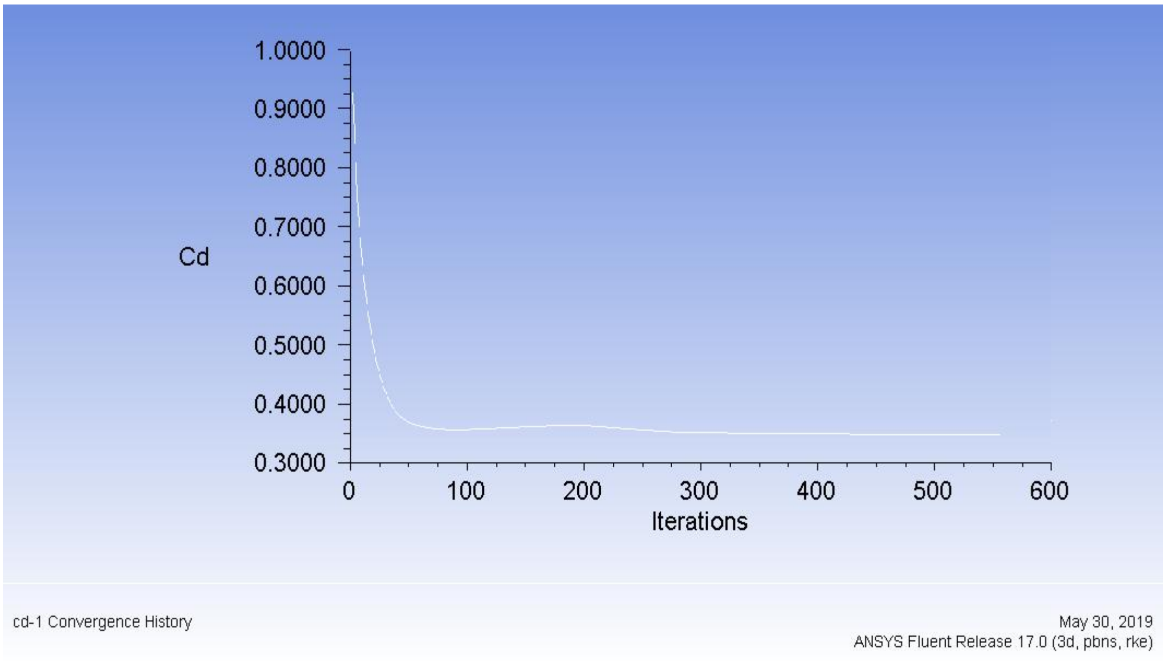

Figure 4.4. Drag coefficient of baseline model at 120kmph

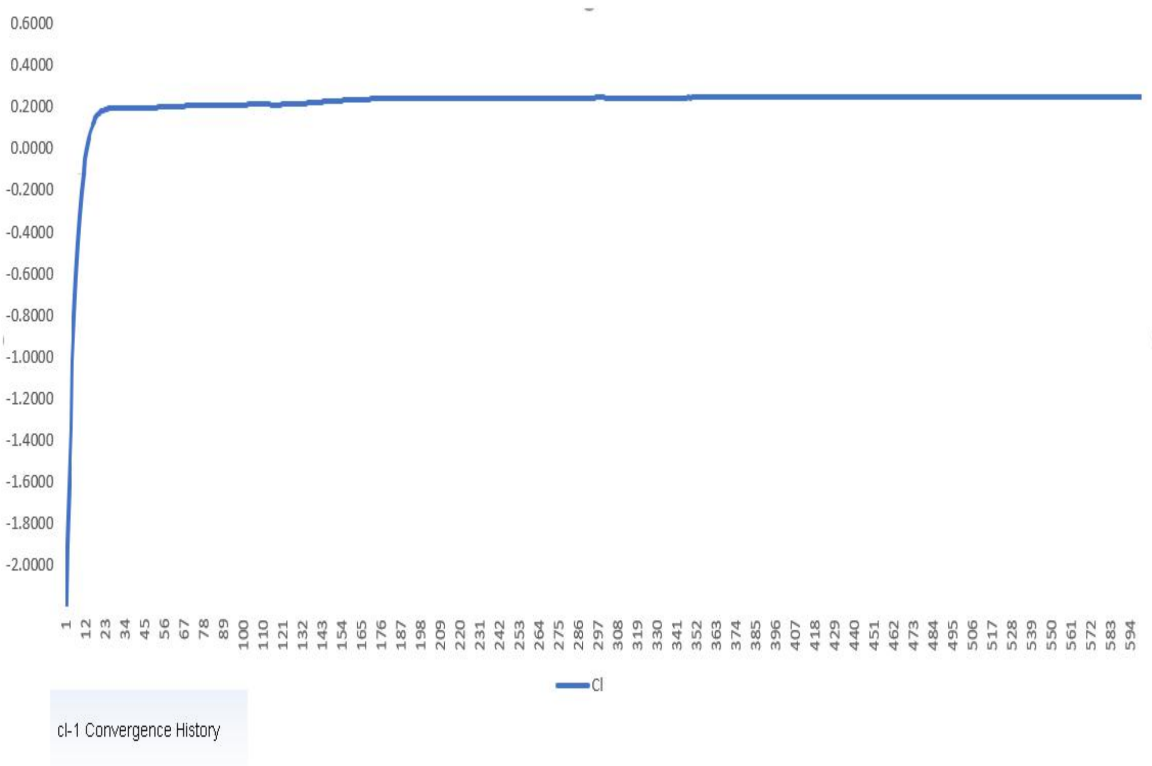

Figure 4.5. Lift coefficient of baseline model at 80kmph

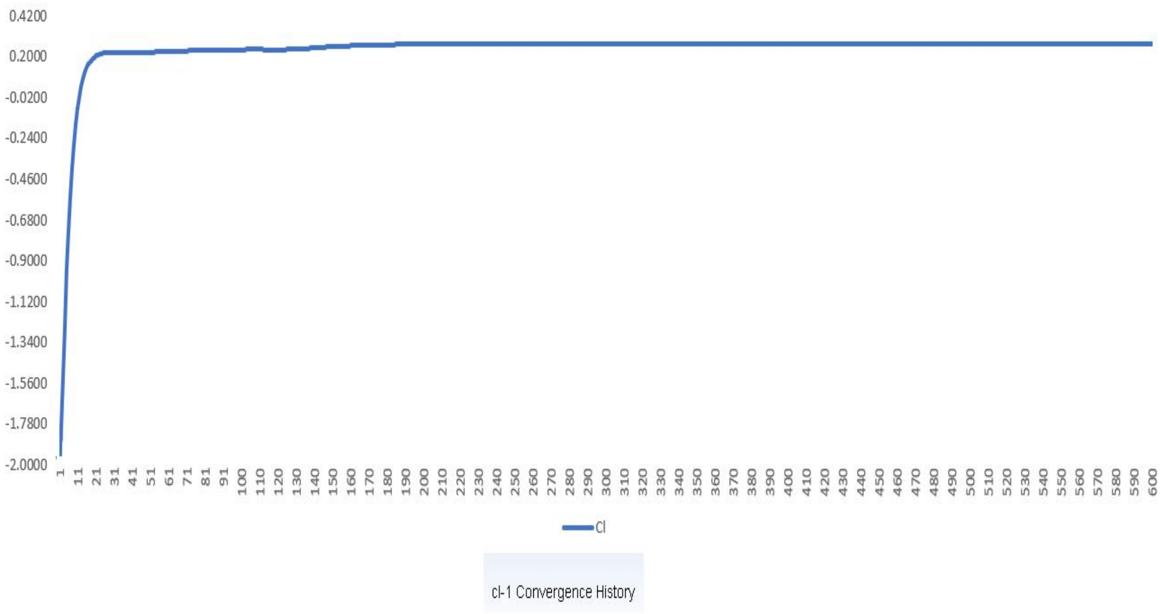

Figure 4.6. Lift coefficient of baseline model at 100kmph

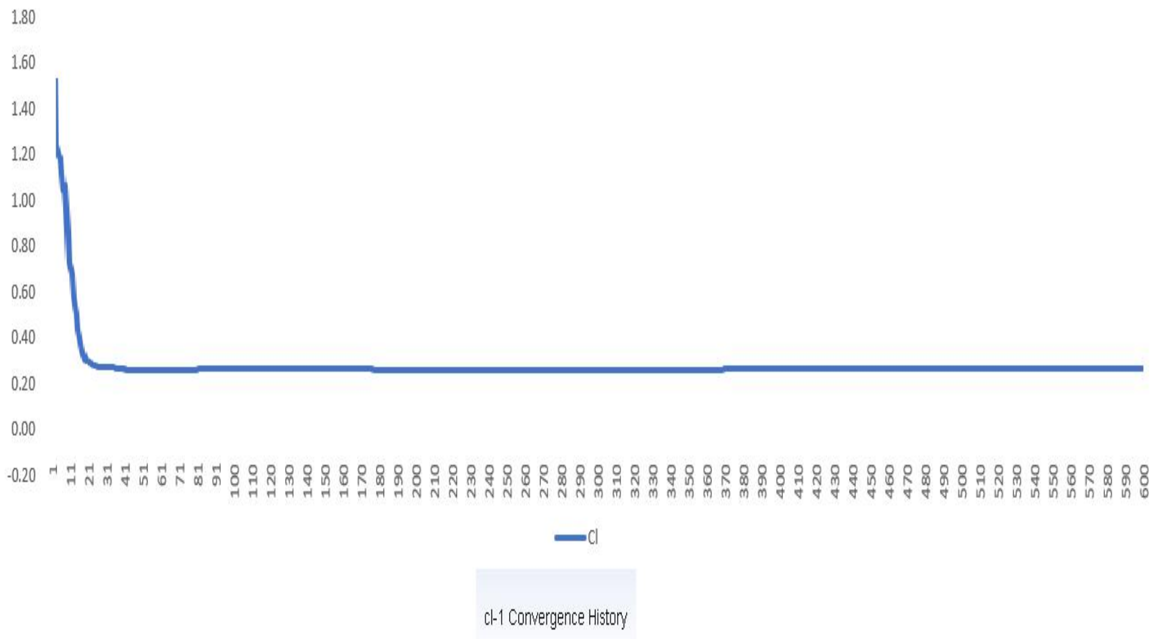

Figure 4.7. Lift coefficient of baseline model at 120kmph

Table 4.1. Drag and Lift coefficient of baseline at different speeds

Model	Speed(kmph)	*Cd*	Cl
Baseline Model	80	0.3446	0.2157
	100	0.3458	0.2188
	120	0.3489	0.2091

It can be noted from the above drag and lift coefficient figures (figure 4.2-4.7) and/or table 4.1 that even if both parameters converge way before the 600th iteration, the lift coefficient converges much earlier. Another thing is that the drag coefficient (fig 4.2-4.4) of the baseline model increases with increasing speed, whereas the lift coefficient (fig 4.5-4.7) decreases with speed. The decrease in lift coefficient at with speeds causes high downward force which is favorable that it increases vehicle stability at higher speed.

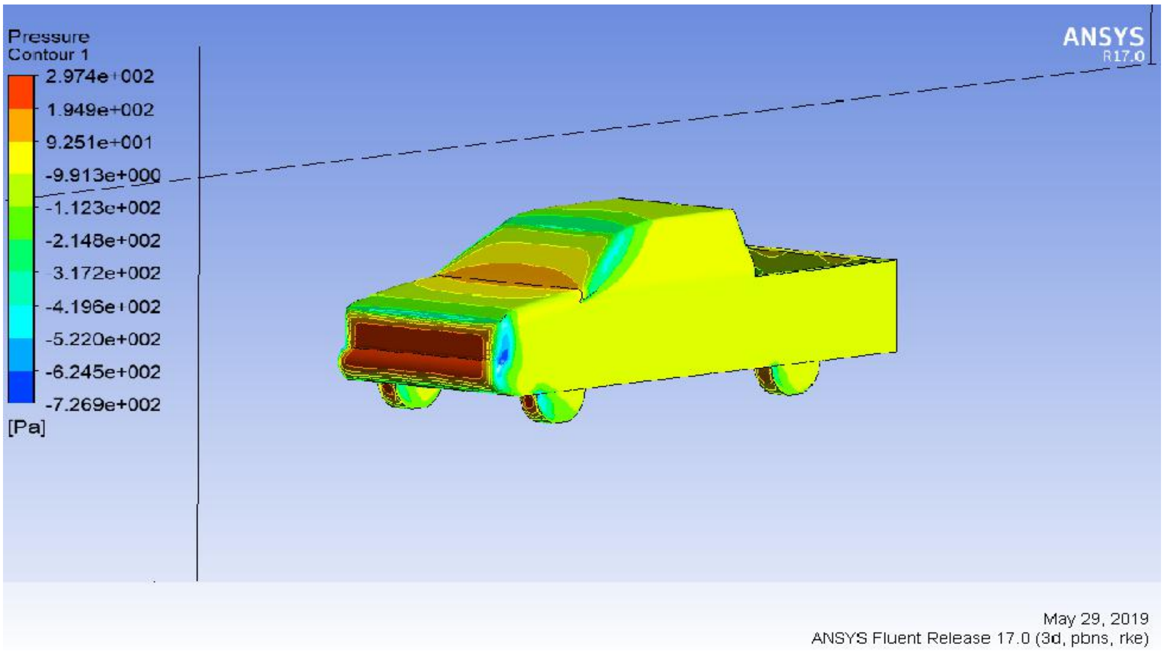

Figure 4.8. Pressure contour of baseline model at 80kmph

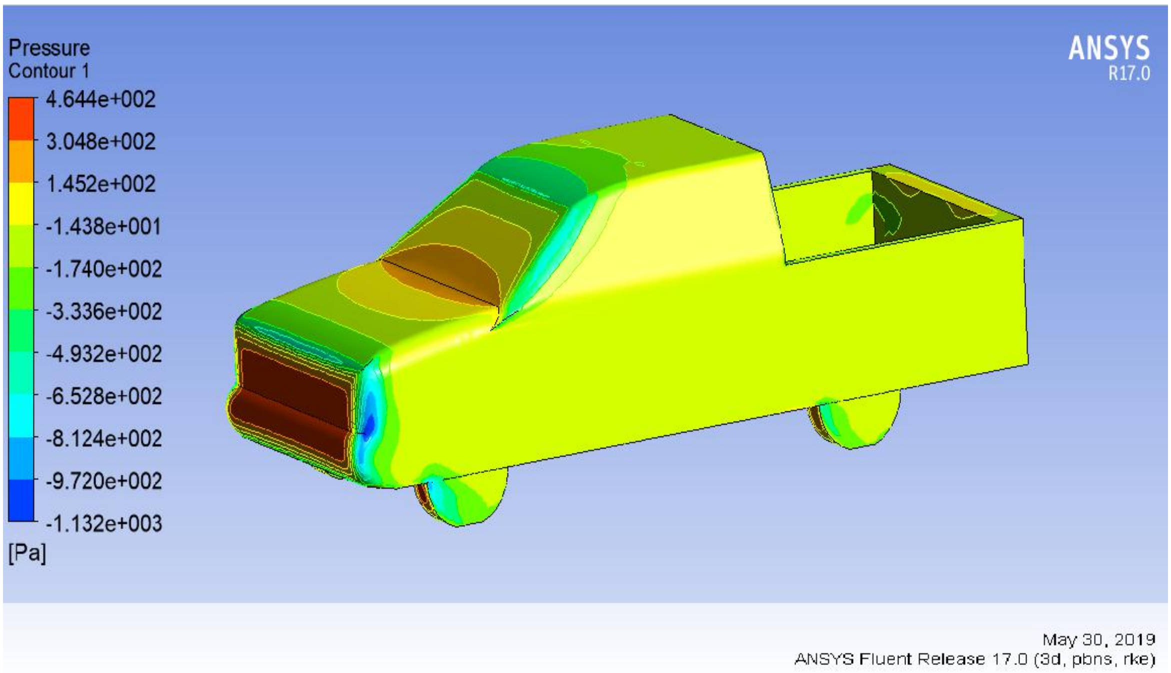

Figure 4.9. Pressure contour of baseline model at 100kmph

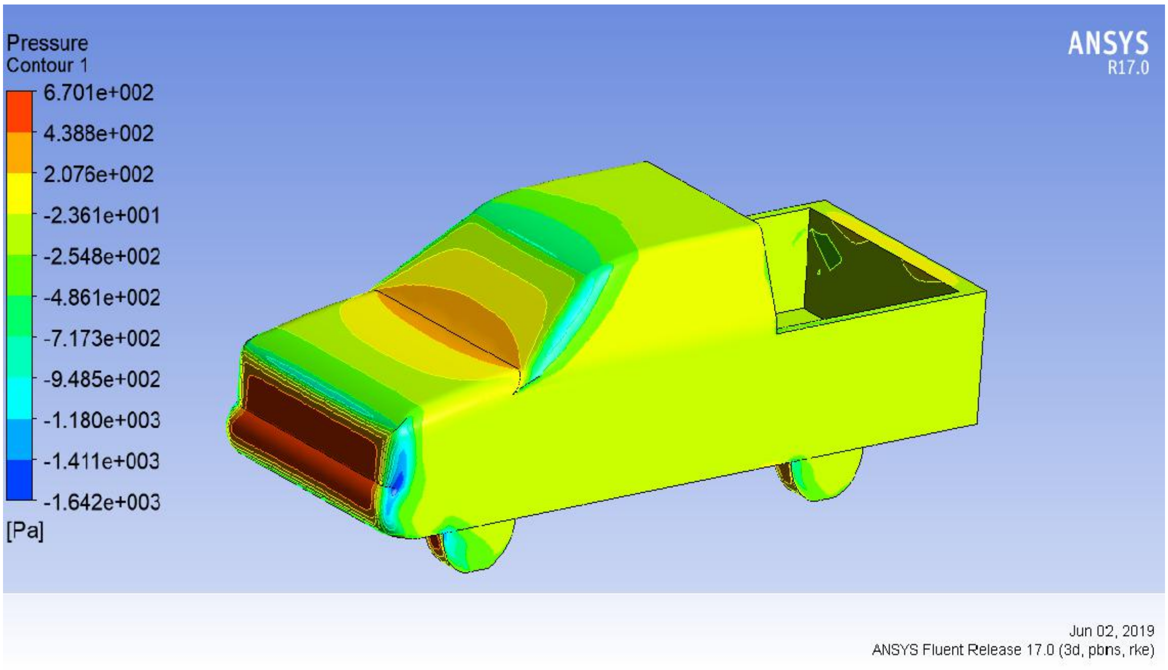

Figure 4.10. Pressure contour of baseline model at 120kmph

The pressure distribution on the surface of the baseline model can be seen on figure 4.8-4.10. From the figures we can see that the maximum pressure occurs on the grill and, at the junction between the engine hood and the windshield. We can also see that with increasing speed the maximum pressure increases which contributes to high amount of drag at higher speeds.

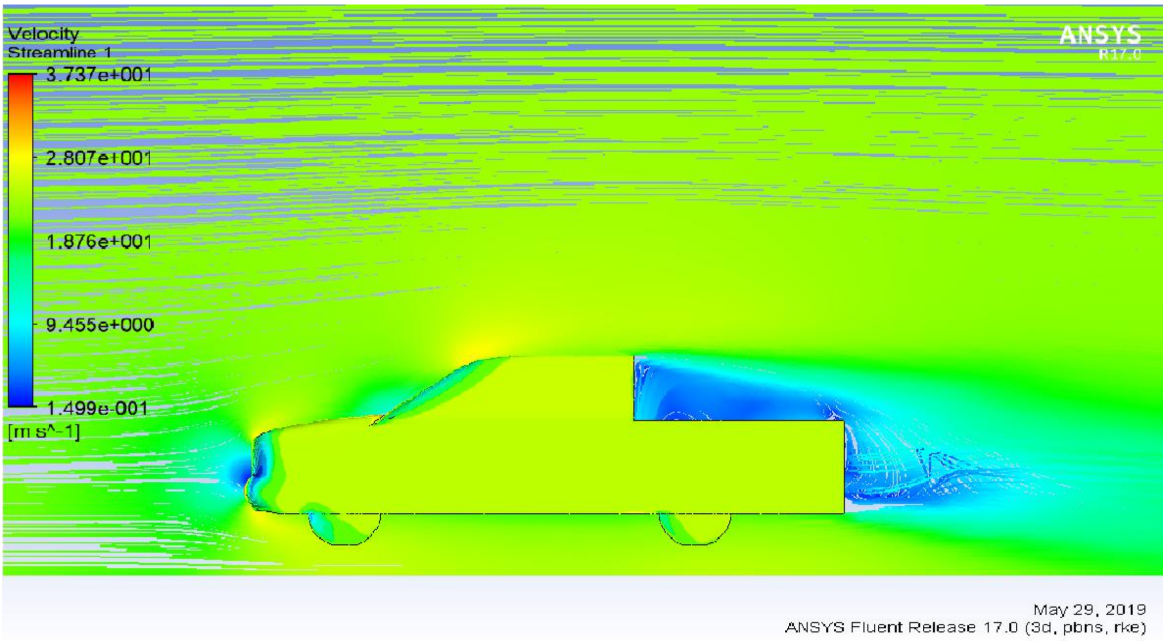

Figure 4.11. Velocity contour of baseline model at 80kmph

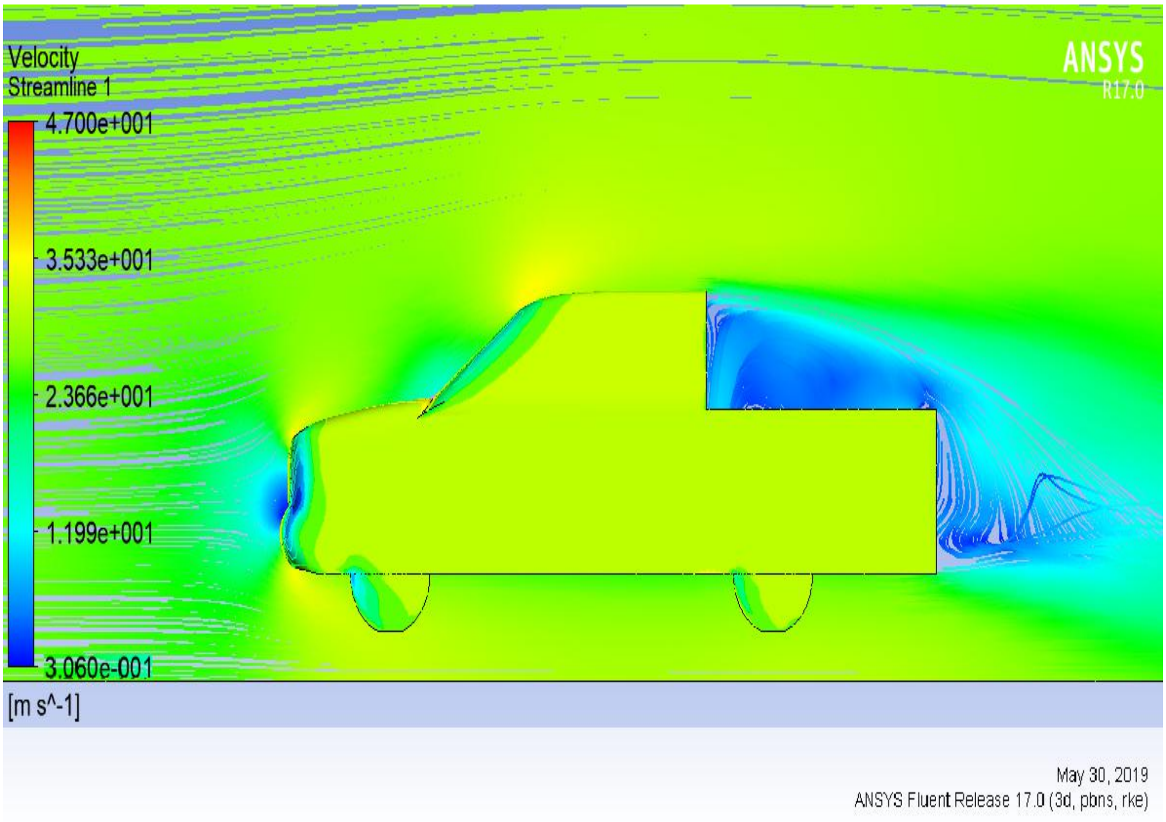

Figure 4.12. Velocity contour of baseline model at 100kmph

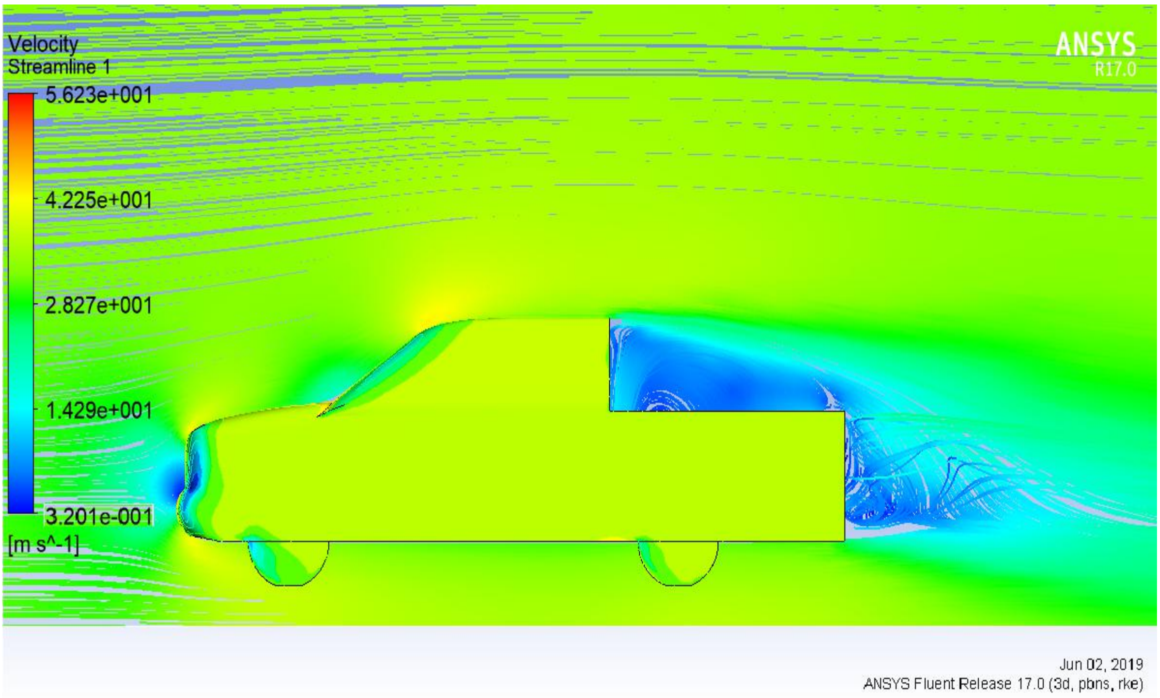

Figure 4.13. Velocity contour of baseline model at 120kmph

To determine the reduction in the drag coefficient from the addition of spoiler on the rear end of the roof the drag coefficient, lift coefficient and flow field around the bus without any drag reduction device was examined first. These simulations give the base drag coefficient for the study. After simulating the baseline model, the modified models were simulated next. After simulation all models were compared to the flow field, drag and lift coefficient of the baseline vehicle. To determine the percent reduction of parameter due to the spoiler the drag coefficients were compared.

To analyze the flow around the vehicle due to its motion it is important to look at the velocity field. This analysis was able to provide important information about the turbulence and air flow present around the vehicle. Figure (4.11-4.13) above illustrates the velocity contour obtained using Fluent for the pickup vehicle without any drag reducing device employed at three different speeds. A legend can be observed in Figure 4.11-4.13, representing the magnitude of the velocity of the air flow in m/s, with colors corresponding to the velocity contour shown. It should be noted that the velocities were 22.22 m/s, 27.78m/s, and 33.33m/s and the maximum velocity for each model in the flow field due to flow separation was nearly 37.37m/s, 47m/s and 56.23m/s and the minimum velocity was 0.1499m/s, 0.306m/s and 0.3201m/s respectively. The colors indicate the velocity magnitude. The green color in the contour represent the velocities close to the input velocity.

Sudden changes in the geometry of the vehicle created sections of maximum velocities. Such sections can be seen around the top and bottom horizontal edges of the windward face, on the front edge of the hood, and the bottom edge of the grill. Red color represents high velocity areas of the contour. These high velocities are surrounded by slowly decreasing velocities which are represented by orange through yellow colored sections in the contour. This was continued until, farther away from the vehicle, then the velocity evened out at the magnitude of the input velocity. Increase in the velocity from the input velocity to the maximum velocity causes flow to separate and makes the low velocity air to swirl inside the bed box.

Blue color sections in the contour represent low velocity areas present on the body. Low velocity area can be seen on the front of the grill, inside the bed box, and on the back of the vehicle tail. These low velocity areas produce high levels of turbulence and this turbulence increases the drag on the pickup. The drag increases due to the air trapped inside the bed box. In addition, the wake region behind the vehicle tail highly contributes to the increase in the drag coefficient.

Due to the absence of internal flow and under floor and body roughness, pressure drag occurs to highest percentage. Figure 4.14 below shows the surface pressure distribution along the symmetry plane and it indicates that the maximum value is at the truck's front surface where the stagnation point is generated. It can be noted that the pressure on the front of the cab decreases due to its streamlined shape and then increases gradually and again it decreases. On the roof of the vehicle the pressure starts to raise again and continues to raise till the tail of the vehicle. The pressure on the floor of the vehicle is almost constant.

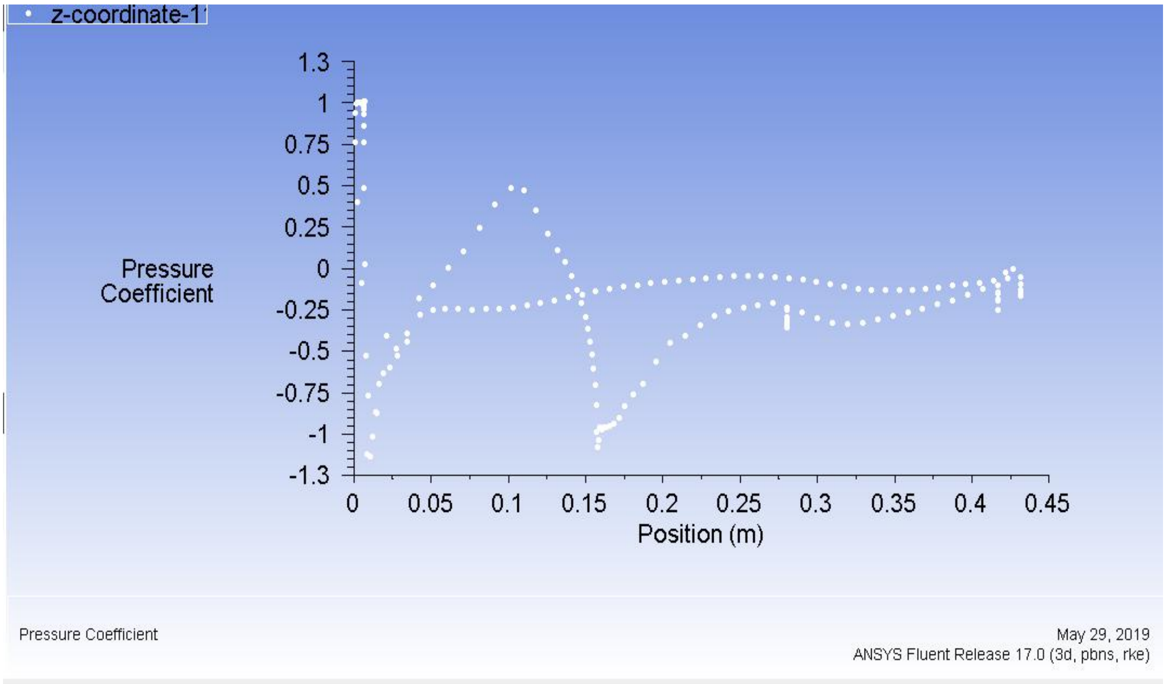

Figure 4.14. Surface pressure distribution along symmetry plane of baseline model

4.1.2 Validation of the result

This study was validated using results of previous studies conducted by Yang and Khalighi [13] and Pramod et al. [36].

Comparison of streamlines, and Surface pressure distribution on the vehicle was made between the results from Yang and Khalighi [13] and the present study as shown in figures (4.15-4.18) below.

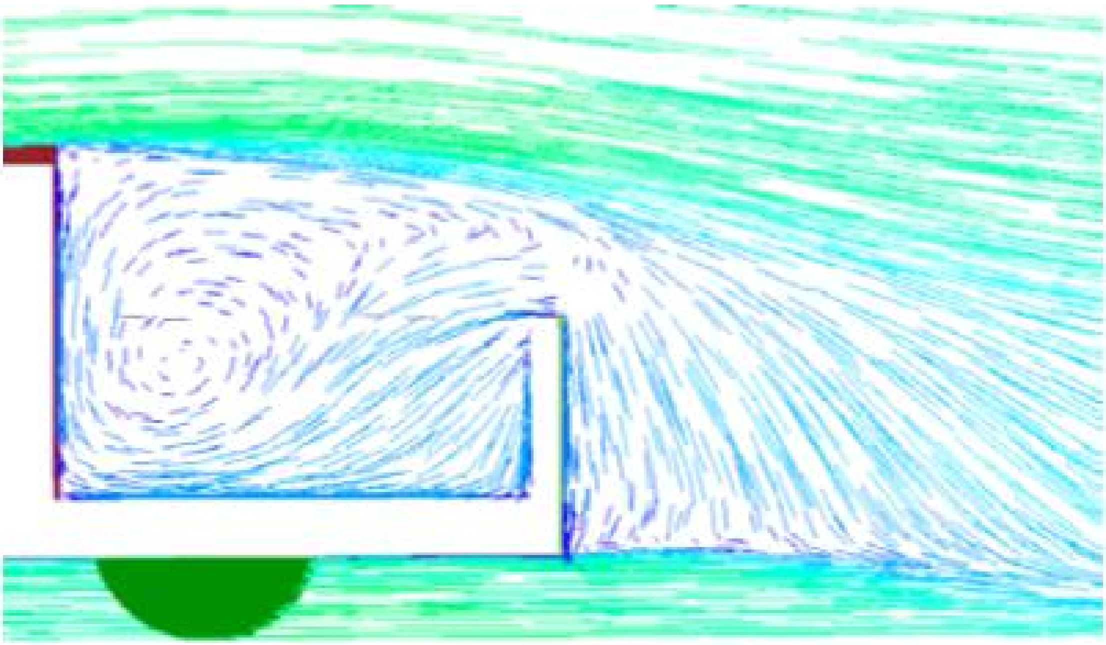

Figure 4.15.   Streamline on symmetry plane [13]

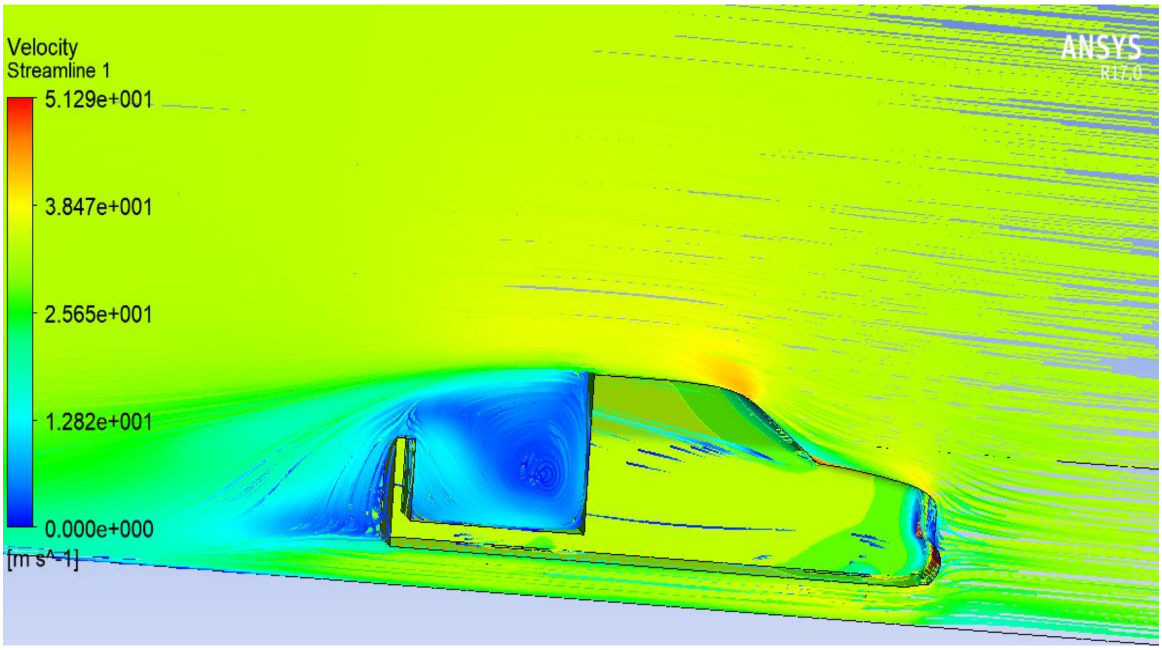

Figure 4.16. Streamline on symmetry plane

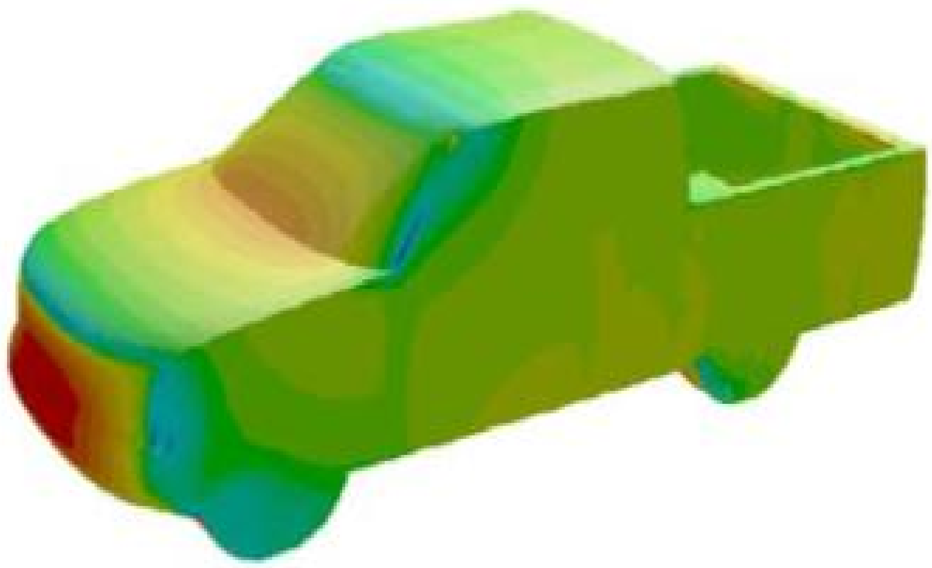

Figure 4.17. Pressure distribution [13]

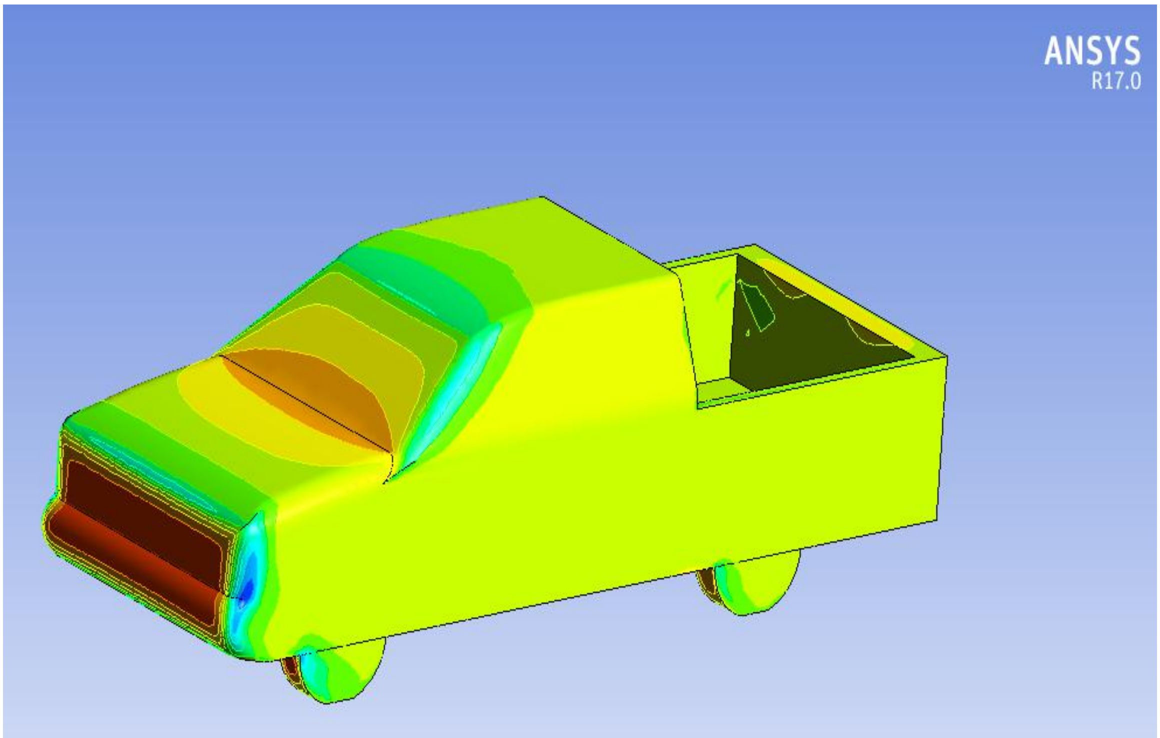

Figure 4.18. Pressure distribution

The other comparison was made between Pramod et al., and the present study on the surface pressure distribution along the symmetry plane. The figure 4.19 from Pramod is shown below whereas the surface pressure distribution of the present study is shown in figure 4.14.

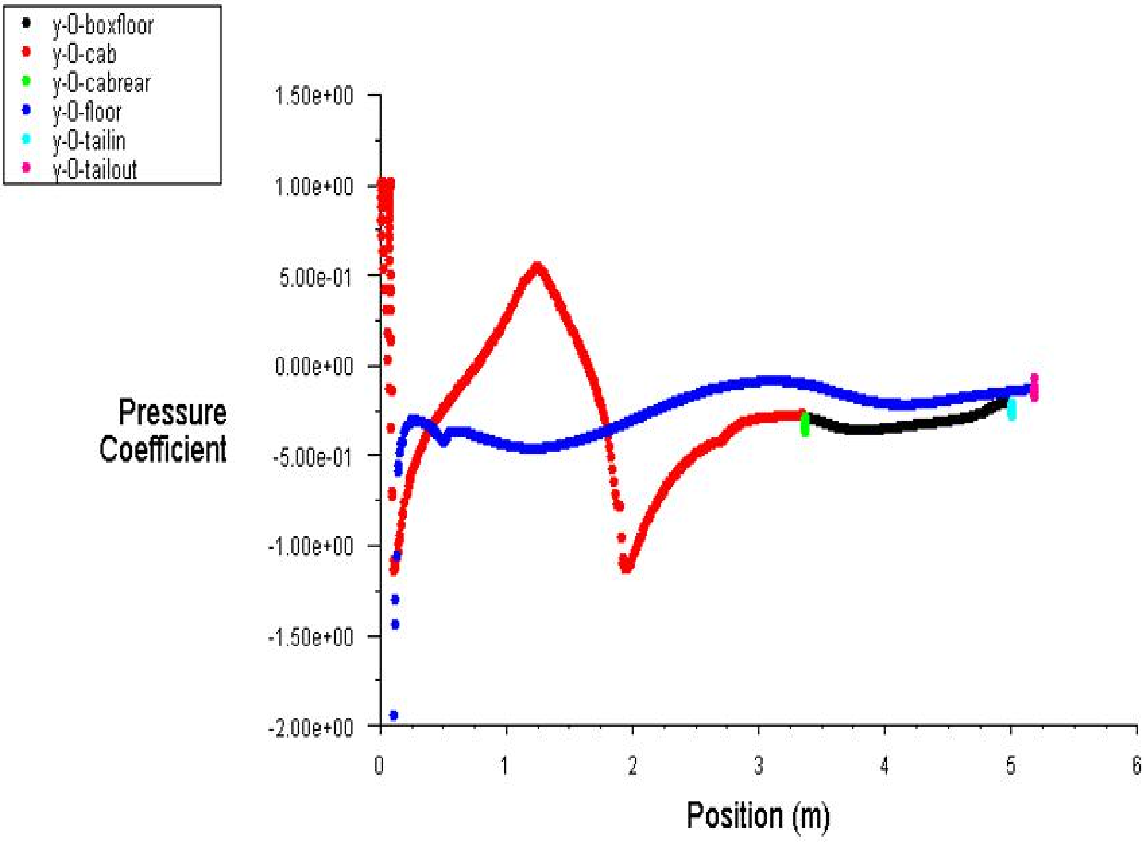

Figure 4.19. Surface pressure distribution along symmetry plane [36]

From above we can see that both the streamlines fashion, and pressure distribution on the pickup vehicle from yang and khalighi [13] and present study are the same. On both studies how the air swirls inside the bed box of the pickup vehicle and the way the air flows in the wake region are similar. It is interesting to note that the vehicle tires are also subjected to a high aerodynamic pressure as the flow velocity reduces in these areas. This can be seen on the tires of both (figure 4.17 and 4.18)vehicles, it can be seen the color of both vehicles tires turning red. Also, the surface pressure distribution along the symmetry plane between Pramod et al. [36] and present study is alike. The surface pressure distribution on the vehicle surface in both cases changes between maximum and minimum values, whereas on the under body of the vehicle the surface pressure change is very small.

Additionally, as noted in the literature section of this paper the drag coefficients pickup vehicles range from 0.3 ≤ ≤ 0.5, therefore the drag coefficient found in this simulation is in range.

4.2 Model One

4.2.1 Results

Results of scaled residuals, drag and lift coefficients, pressure and velocity contours at speed of 80kmph 100kmph and 120kmph for model one are depicted here.

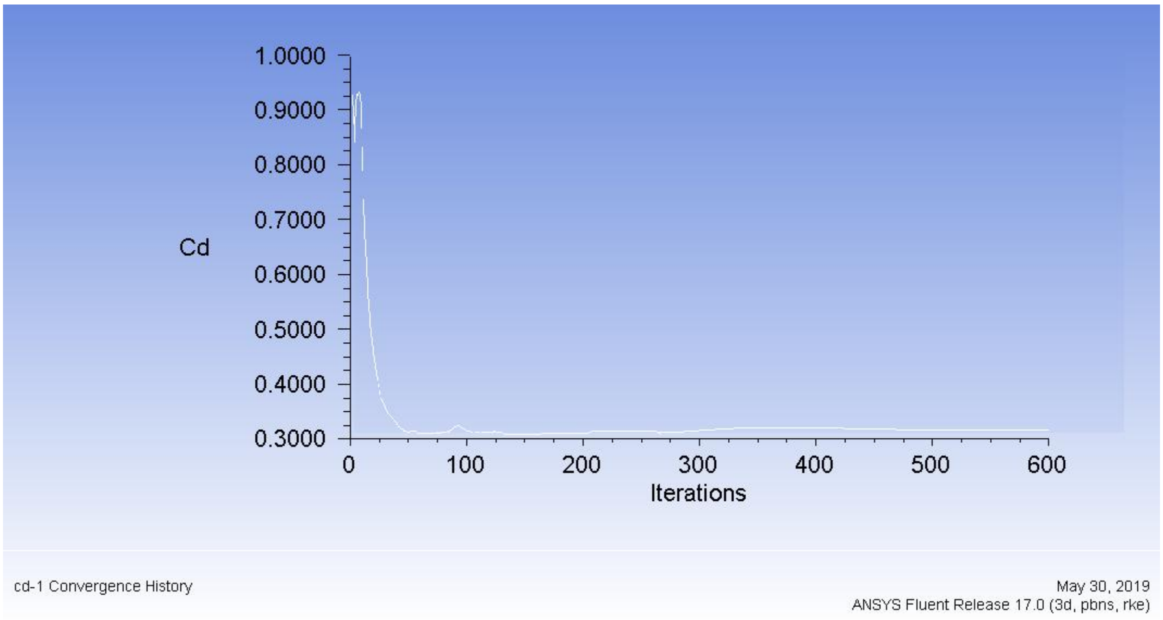

Figure 4.20. Drag coefficient of model one at 80kmph

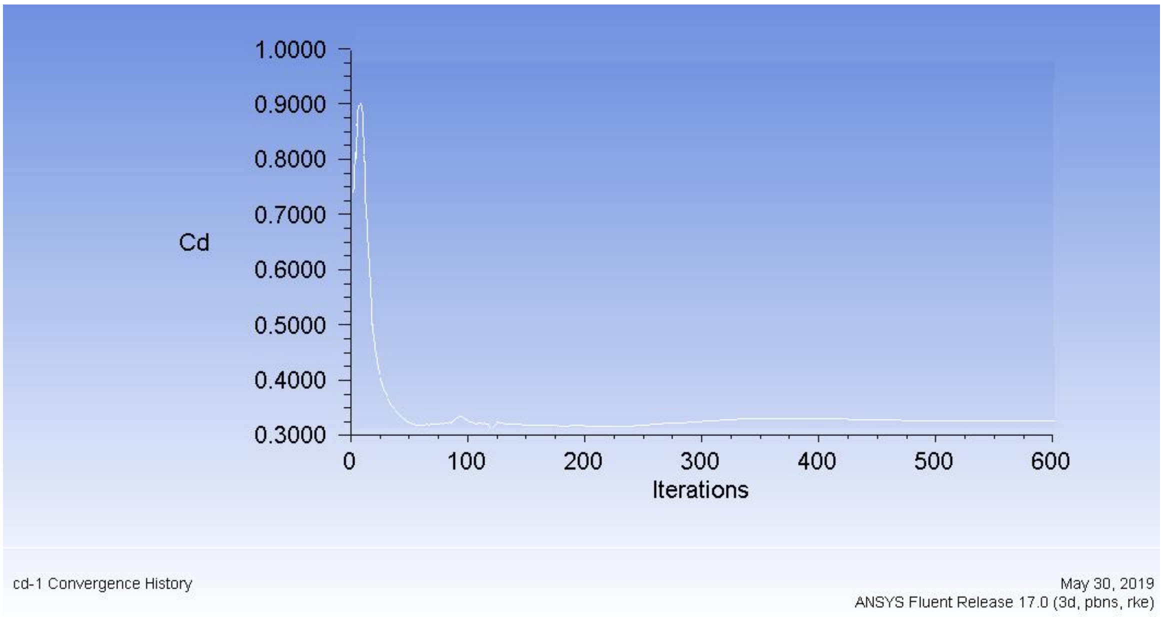

Figure 4.21. Drag coefficient of model one at 100kmph

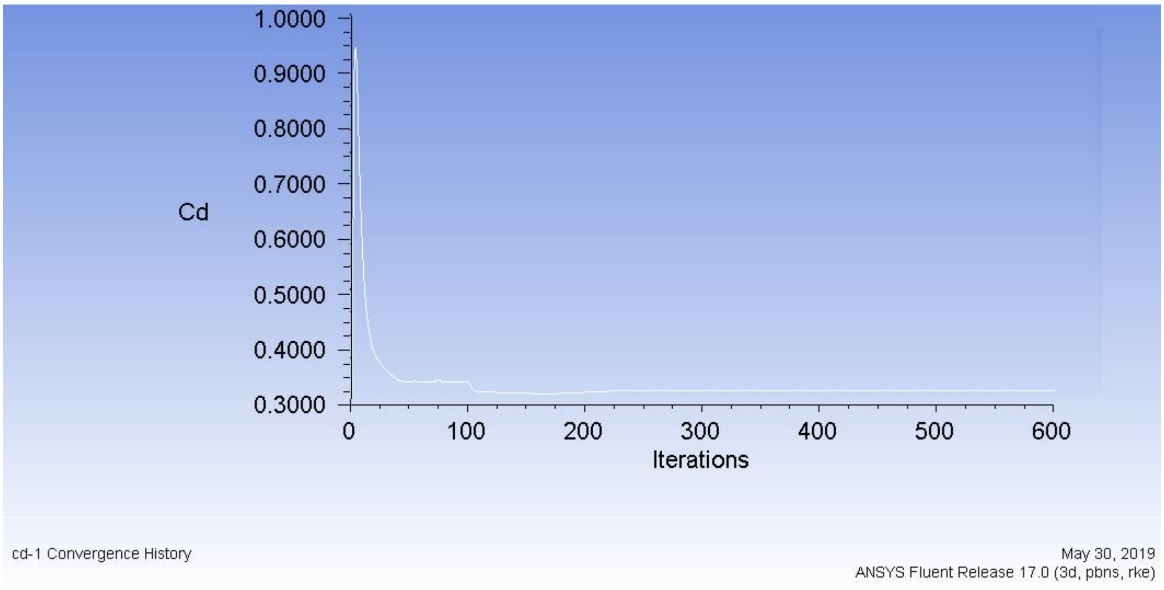

Figure 4.22. Drag coefficient of model one at 120kmph

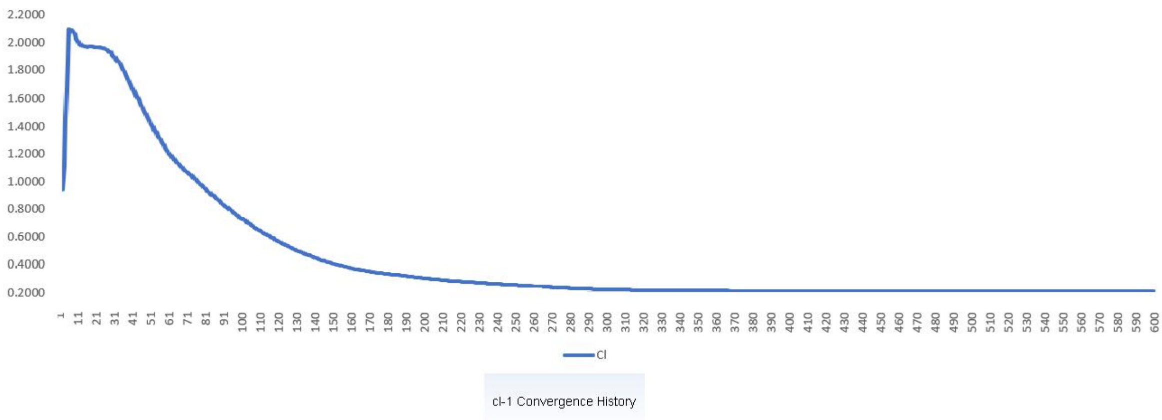

Figure 4.23. Lift coefficient of model one at 80kmph

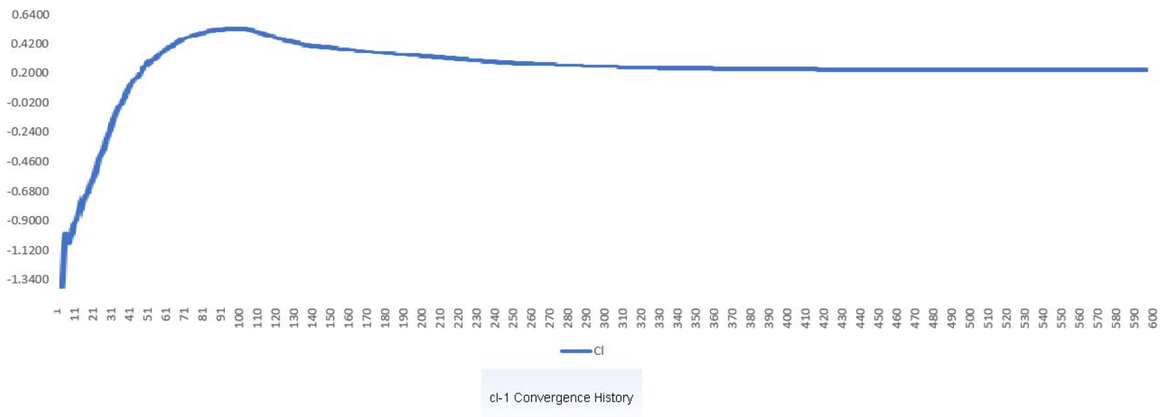

Figure 4.24. Lift coefficient of model one at 100kmph

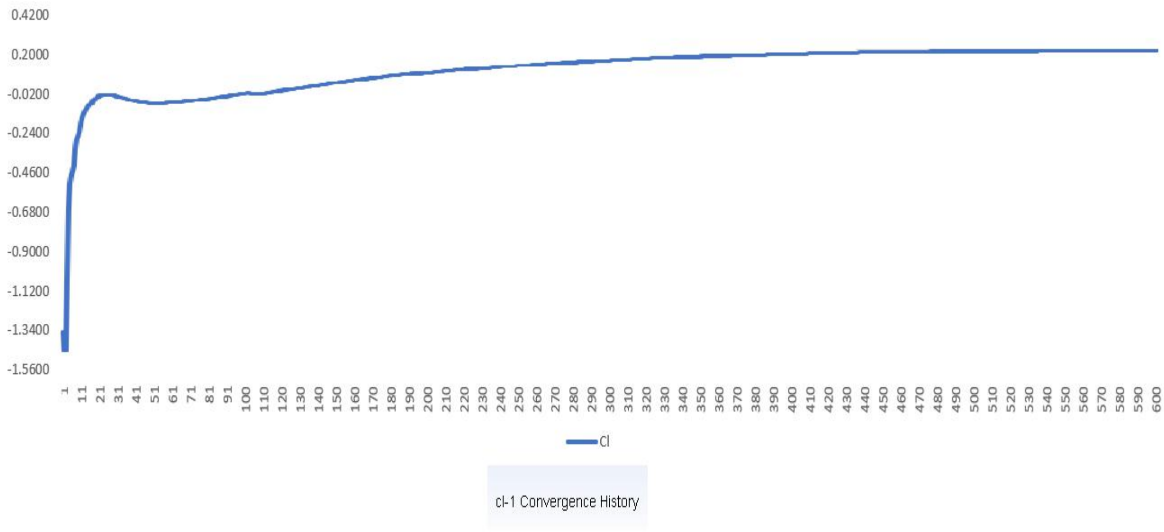

Figure 4.25. Lift coefficient of model one at 120kmph

Table 4.2. Drag and lift coefficient of model one at different speeds

Model	Speed(kmph)	*Cd*	Cl
Model One	80	0.3222	0.2134
	100	0.3241	0.2027
	120	0.3287	0.2001

The drag coefficient figures (4.20-4.22) given above for model one show that the drag coefficient increases with increasing speed, but the amount of drag is lower than that of the baseline model. And here also in model one the lift coefficient figure 4.23-4.25 decreases with increasing speed. The figures 4.23, 4.24 and 4.25 show how the lift coefficient converges with each iteration. The results of drag and lift coefficients are shown in table 4.2. The increase in downward force is very necessary for stability of vehicle at high speed.

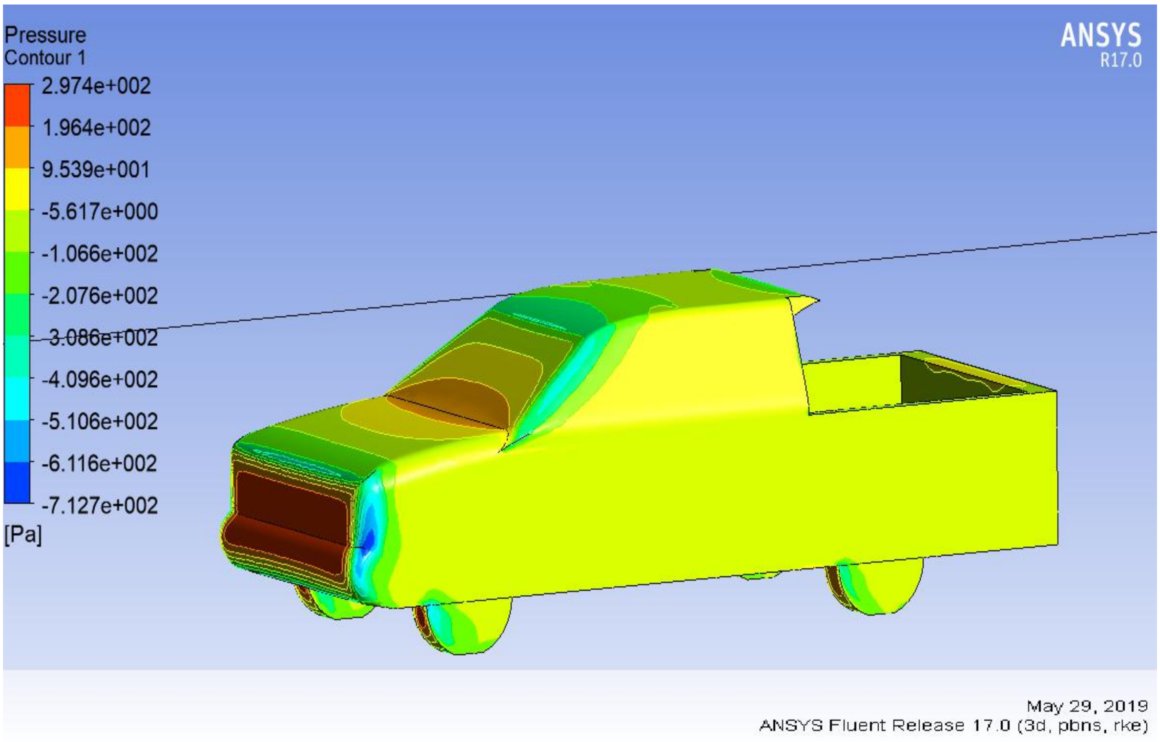

Figure 4.26. Pressure contour of model one at 80kmph

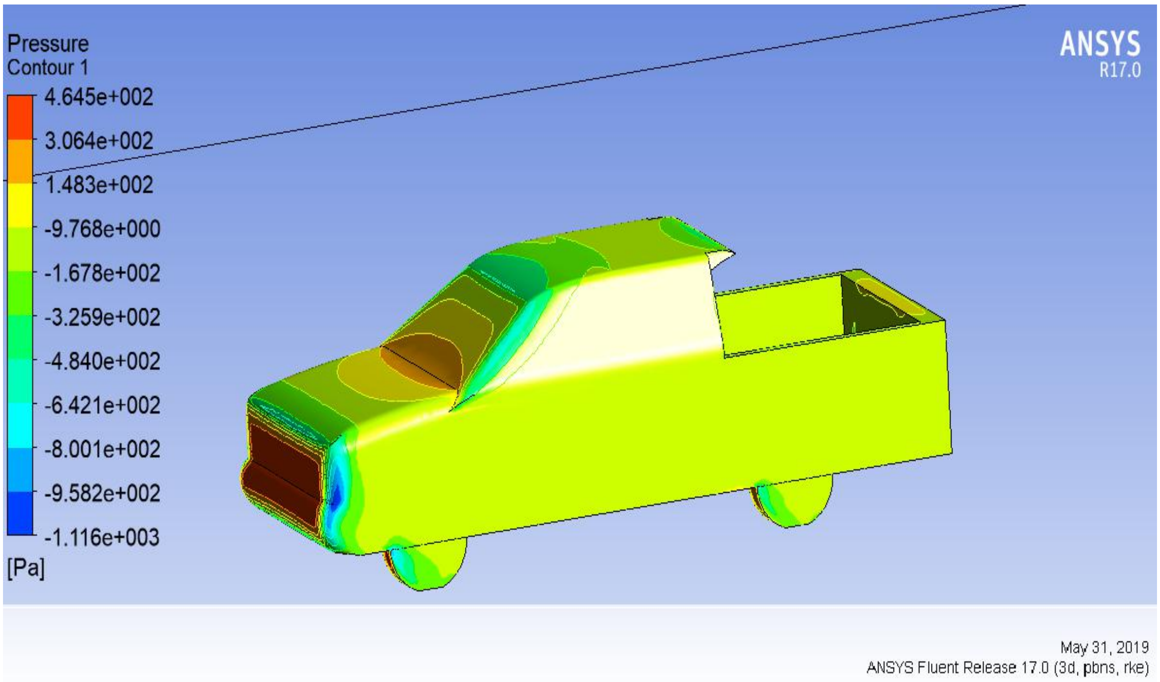

Figure 4.27. Pressure contour of model one at 100kmph

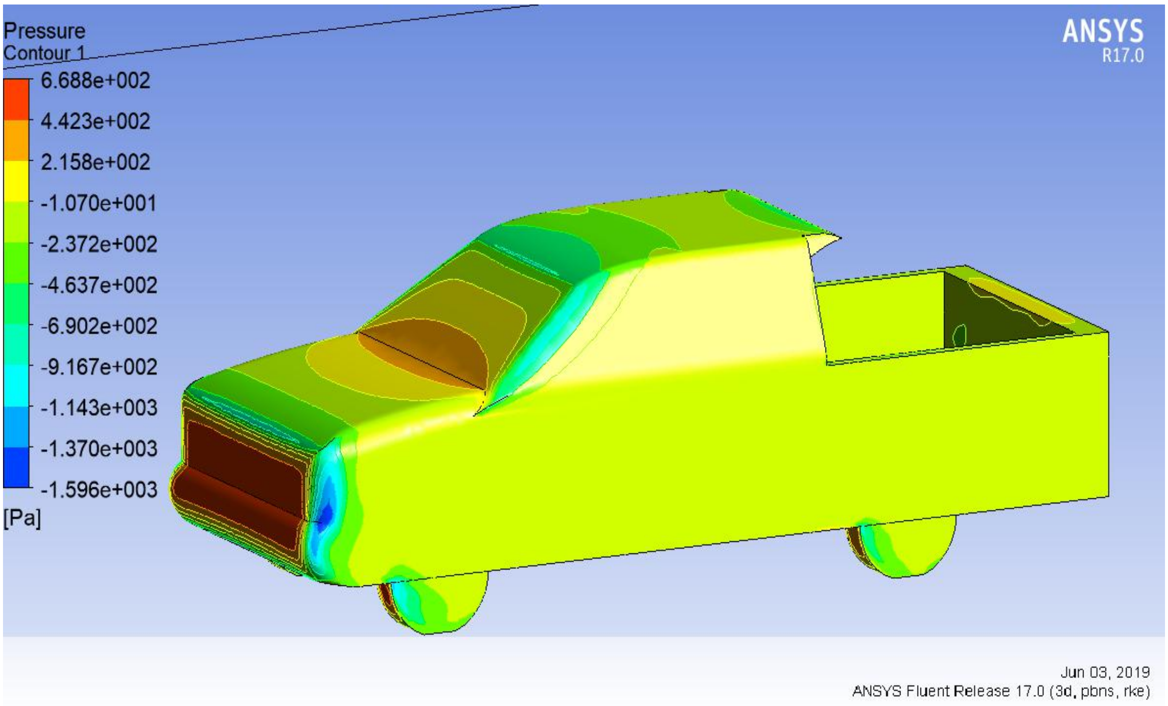

Figure 4.28. Pressure contour of model one at 120kmph

From the pressure contour figures 4.26-4.28 we can see how the maximum pressure varies with the increasing speed of the model. The stagnation pressure on the grill of the vehicle is the peak pressure. The second peak is on surface of the windshield and the engine hood. Due to the sudden change in the profile of the model on the cab rear pressure reduction occurs on the top of the spoiler.

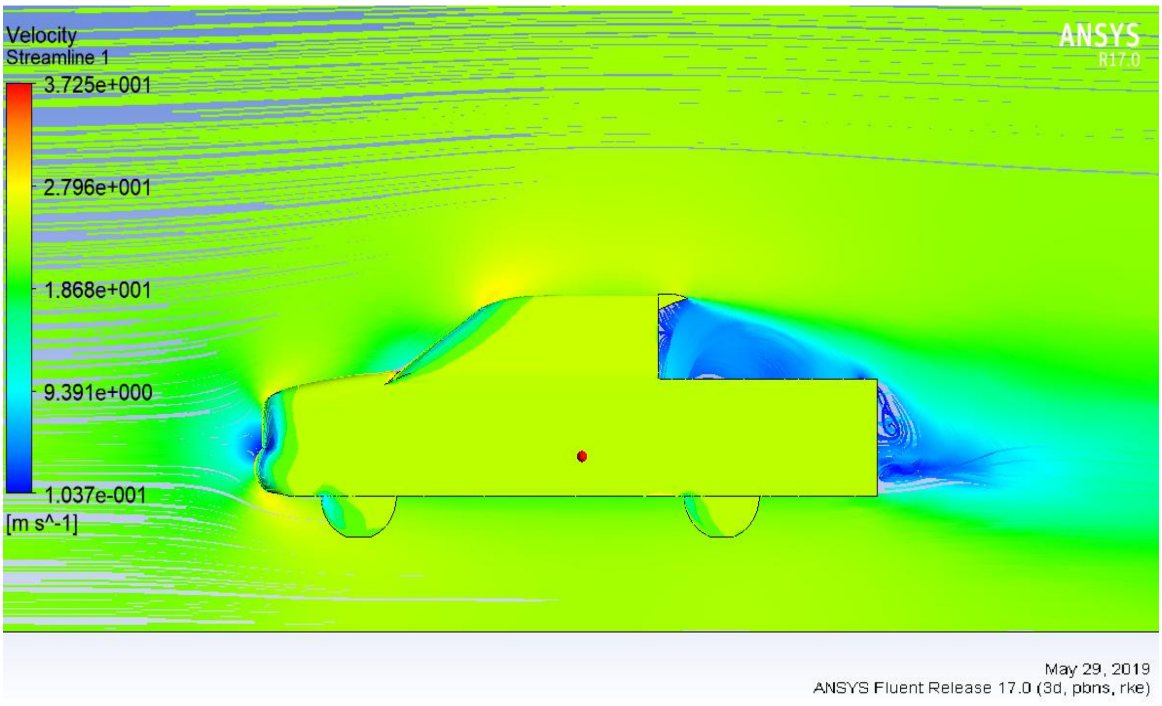

Figure 4.29. Velocity contour of model one at 80kmph

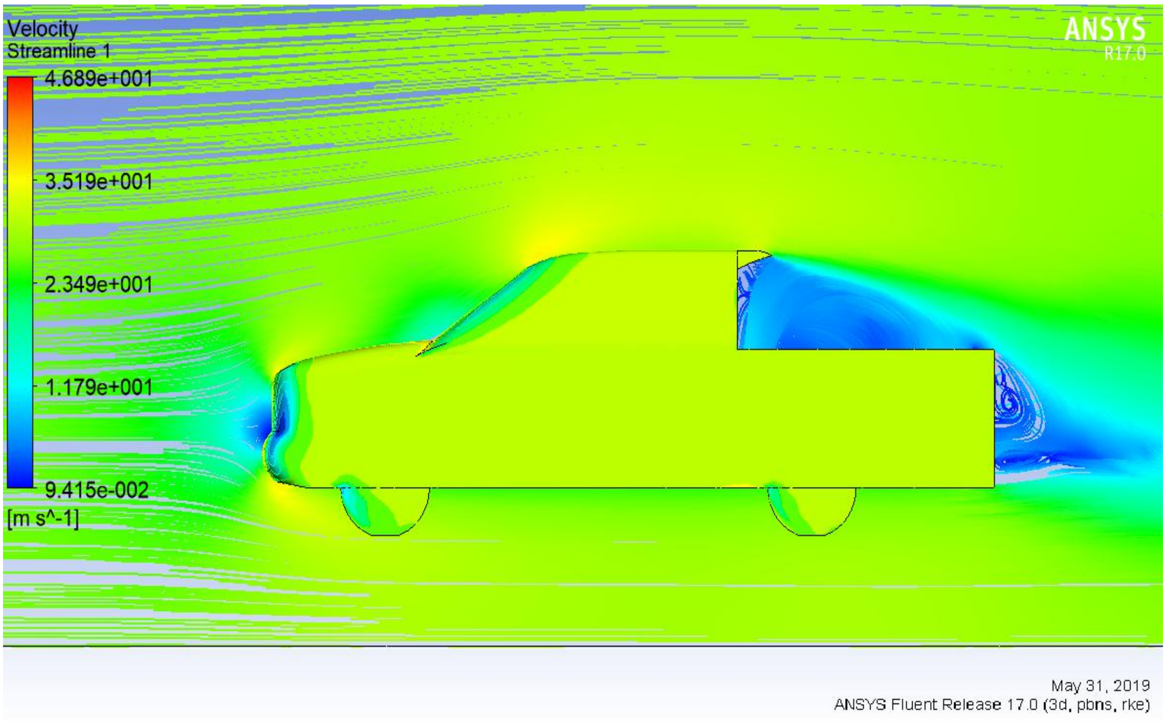

Figure 4.30. Velocity contour of model one at 100kmph

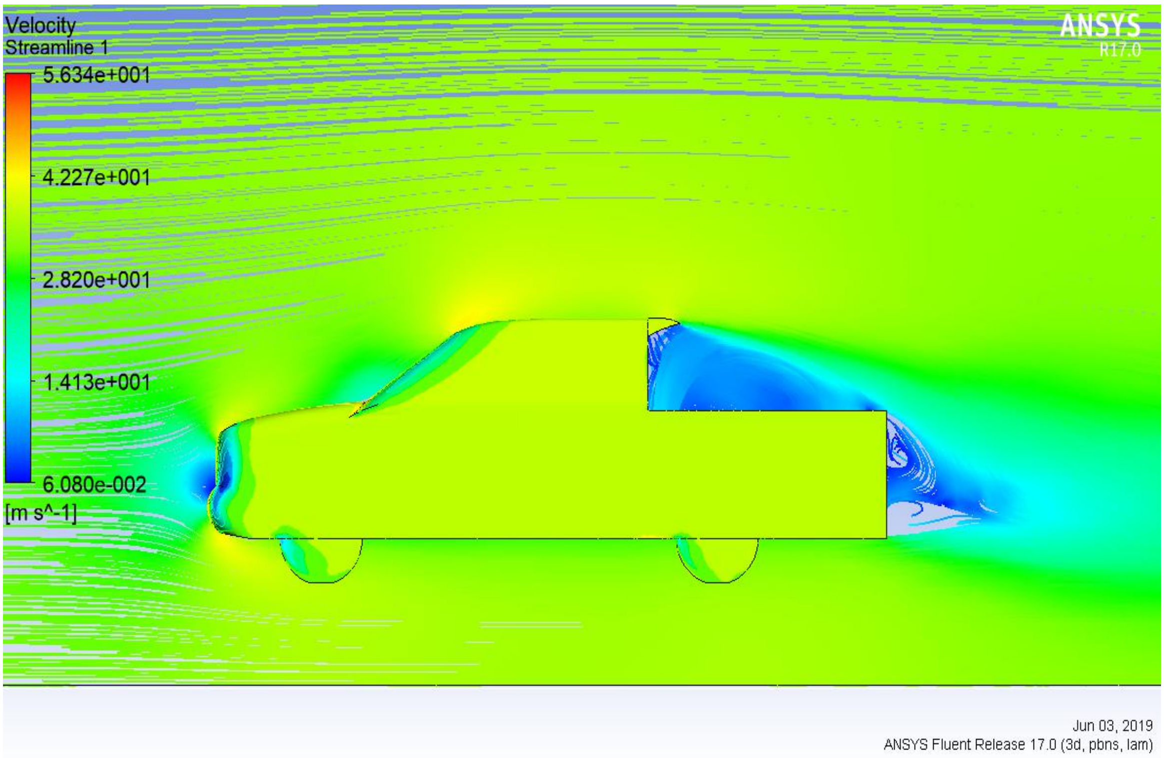

Figure 4.31. Velocity contour of model one at 120kmph

This model is 15mm spoiler attached to the rear end of the baseline model roof at zero inclination angle. The simulation procedure was the same as model one. The scaled residuals were similar with the baseline model.

Here we can examine how the spoiler changed the air flow around the vehicle. From the baseline model and model one (figure 4.29-4.31) the difference in contour can clearly be seen. It can be seen that the wake region behind the tail of the vehicle in model two has decreased than that of the baseline model. The decrement in wake region results in decrement in the drag coefficient of the pickup vehicle. Also, the amount of air swirling inside the bed box of the vehicle is reduced in model two. The reduction in the amount of the air in bed box is because of the air being thrown and guided away from the bed box by the spoiler. The results of these differences can also be seen from the lift and drag curves.

It can be noted from the pressure contour and the surface pressure distribution figure 4.26-4.28 and figure 4.32, that there is a decrease in pressure on the upper surface of the spoiler. This shows that even if the lift coefficient decreases with increasing speed, the amount it decreases is not as much as the drag reduced from the baseline model due to the spoiler. In other way, it shows that the drag coefficient is reduced in model two sufficiently, but the spoiler does not decrease lift greatly. We can also see that the percent difference in lift coefficient between the baseline model and model one decreases as the speed increases. Whereas on the under body of the vehicle the surface pressure distribution is the same as that of the baseline model. The surface pressure distribution figure is the same in fashion and shape for all speeds.

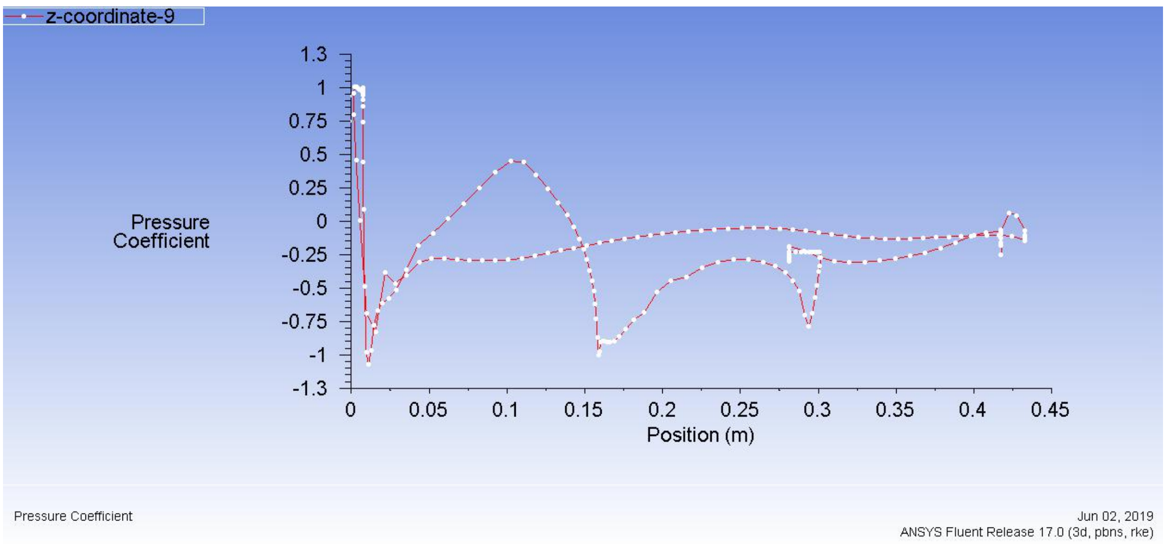

Figure 4.33. Surface pressure distribution along symmetry plane of model one

4.3 Model Two

4.3.1 Results

Result of scaled residuals, drag and lift coefficient, pressure and velocity contour at speed of 80kmph 100kmph and 120kmph for model two are depicted here.

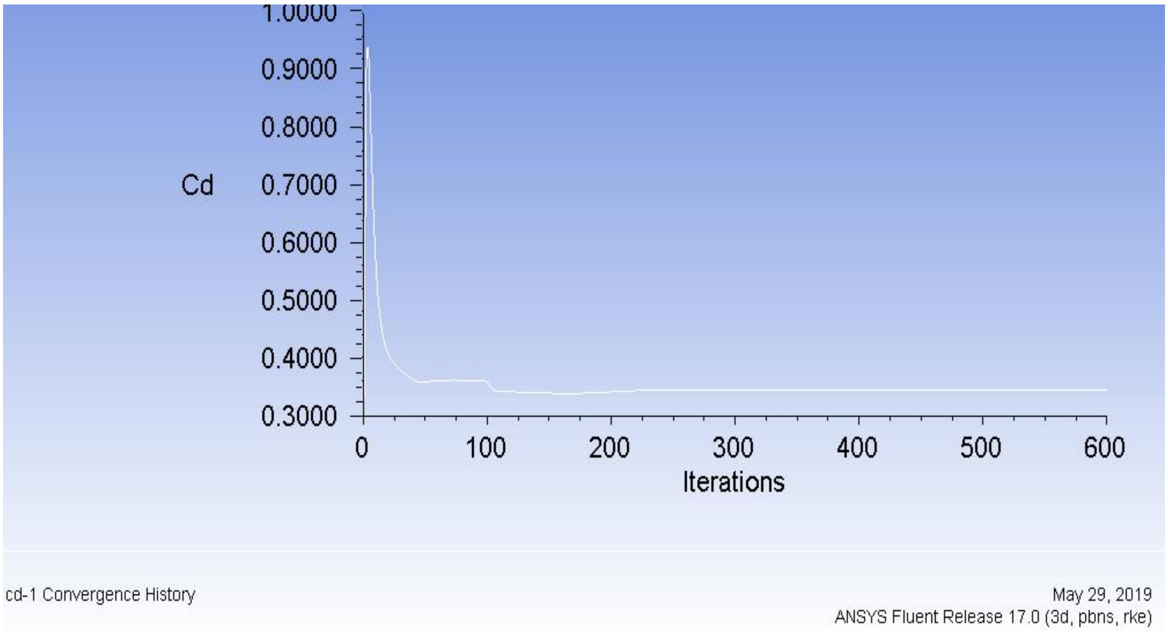

Figure 4.34. Drag coefficient of model two at 80kmph

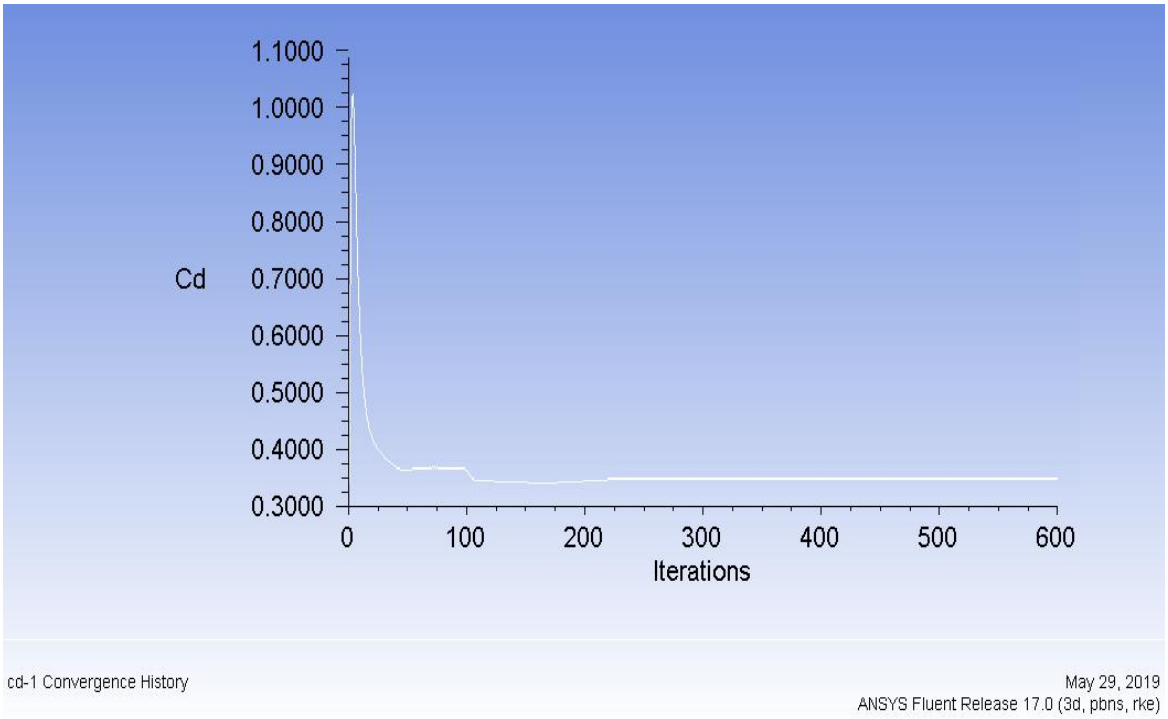

Figure 4.35. Drag coefficient of model two at 100kmph

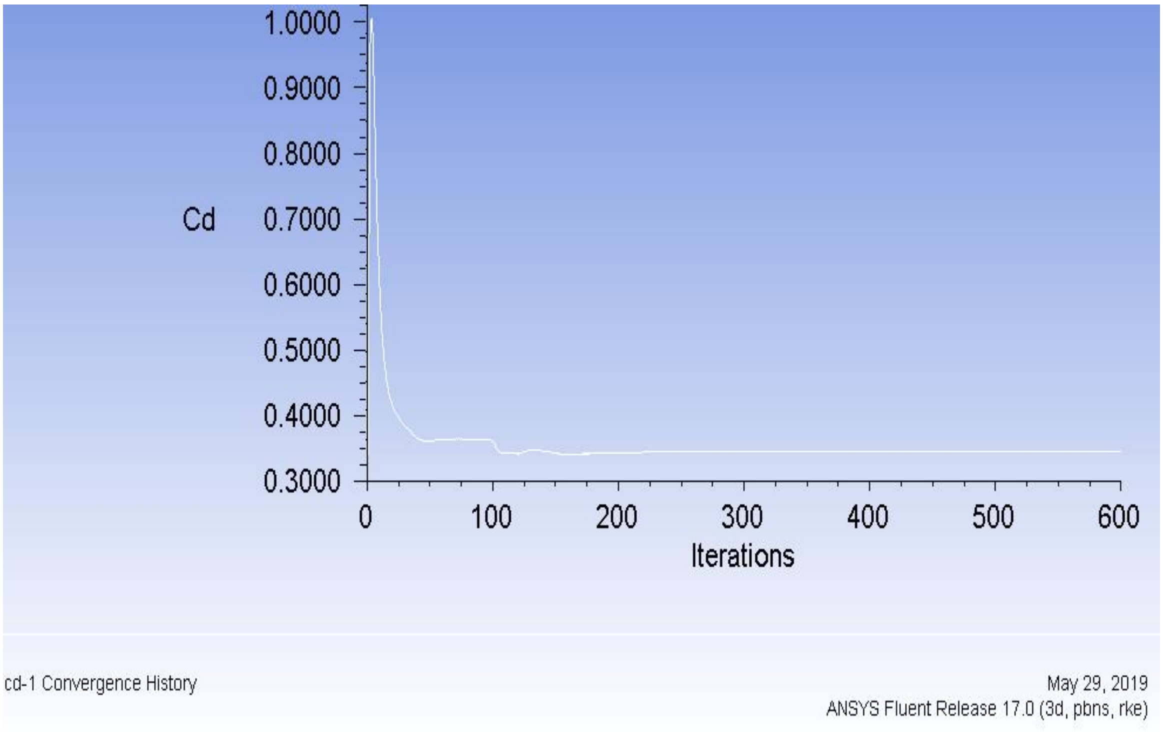

Figure 4.36. Drag coefficient of model two at 120kmph

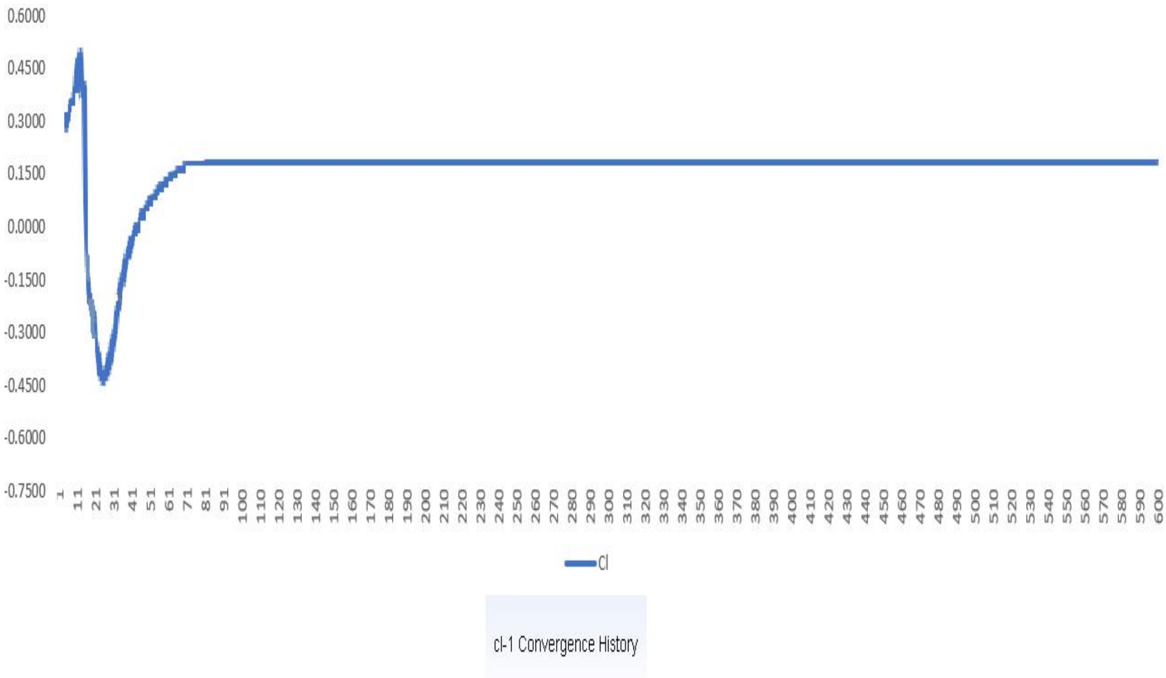

Figure 4.37. Lift coefficient of model two at 80kmph

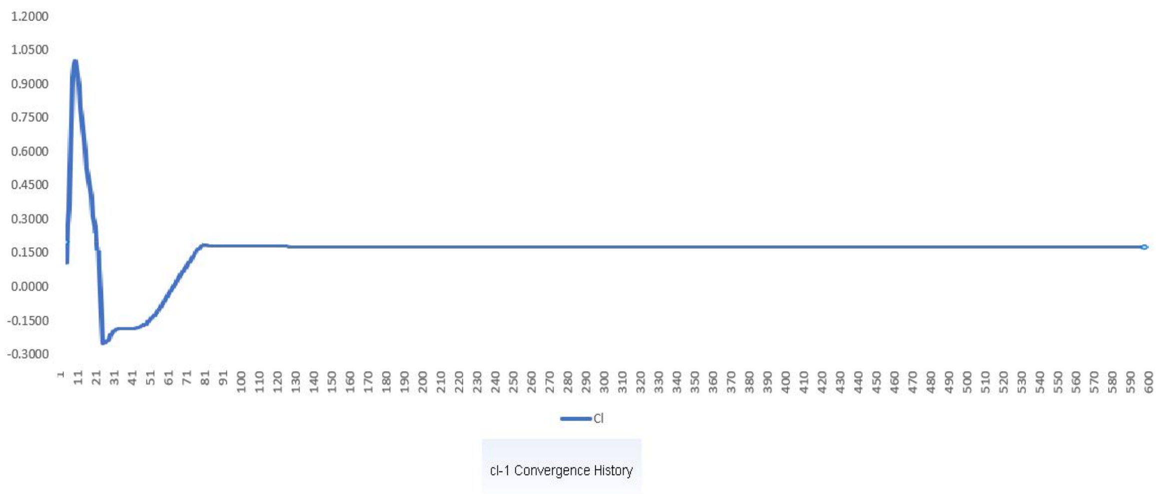

Figure 4.38. Lift coefficient of model two at 100kmph

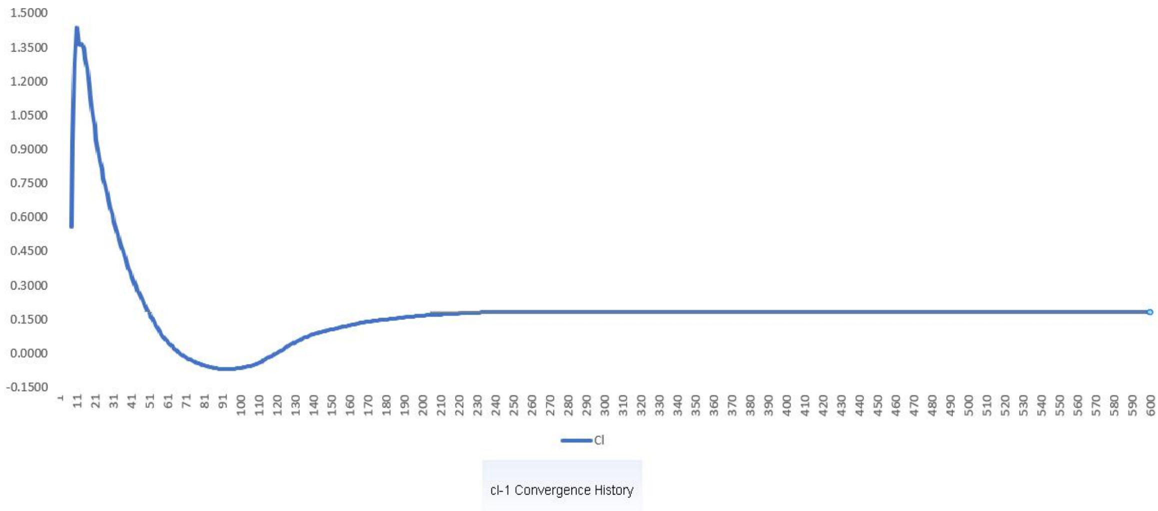

Figure 4.39. Lift coefficient of model two at 120kmph

Table 4.3. Drag and lift coefficient for model two at different speeds

Model	Speed(kmph)	*Cd*	Cl
Model	80	0.3429	0.1789
Two	100	0.3435	0.1741
	120	0.3498	0.1621

Here also the drag coefficient is reduced than the baseline model, but the it is higher than model one (figure 4.34-4.36). And like all the drag increases with increasing speed. The reduction in lift coefficient from the baseline model as the speed increases is greater than that of model one (figure 4.37-4.39). The figures of lift coefficient show how the amount of lift converges with each iteration. The converged values are shown in table 4.3. This means that the model two has higher stability at higher speed at a cost of increased drag than model one.

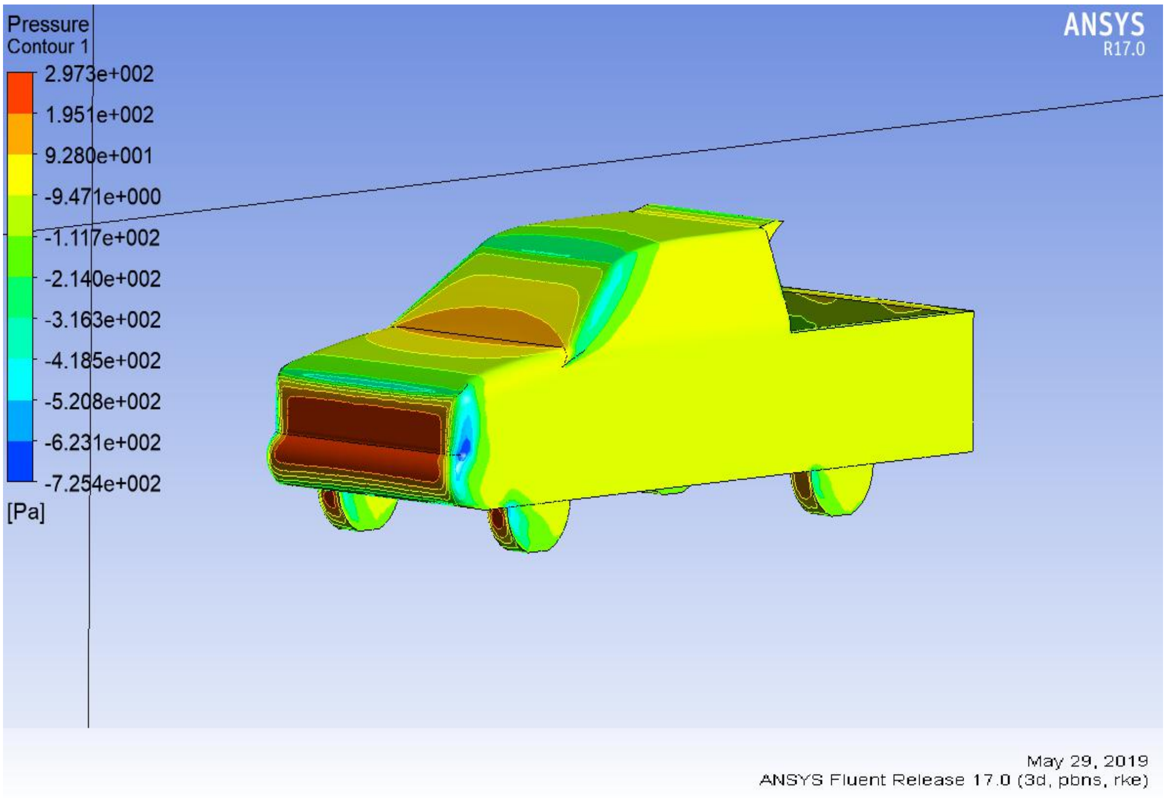

Figure 4.40. Pressure contour of model two at 80kmph

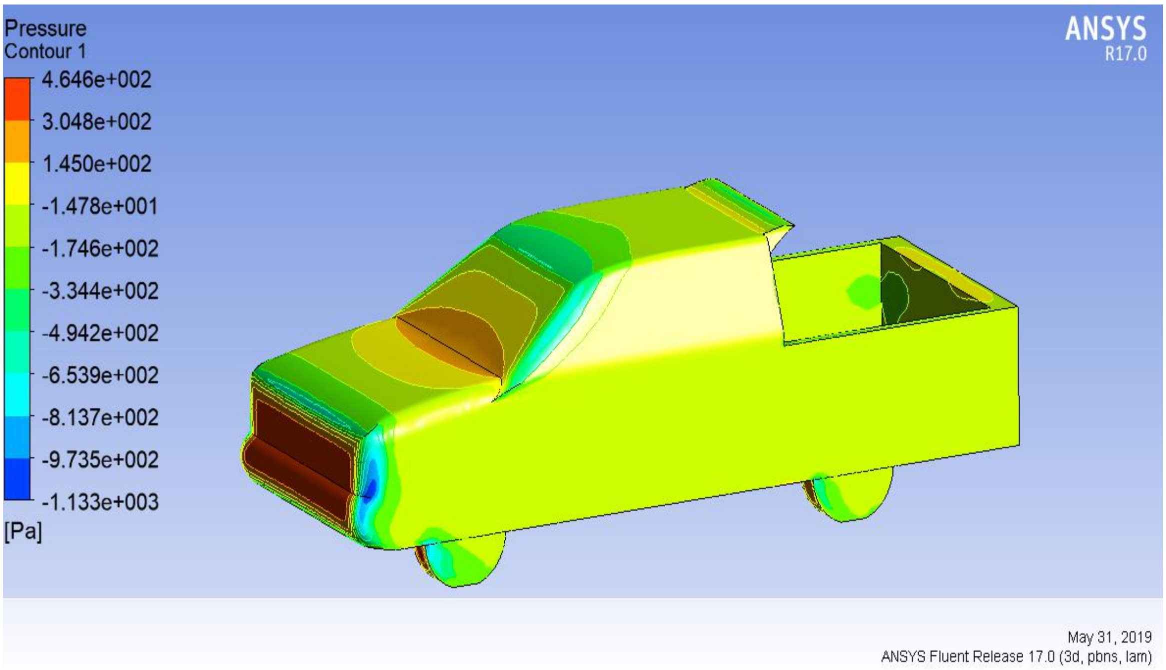

Figure 4.41. Pressure contour of model two at 100kmph

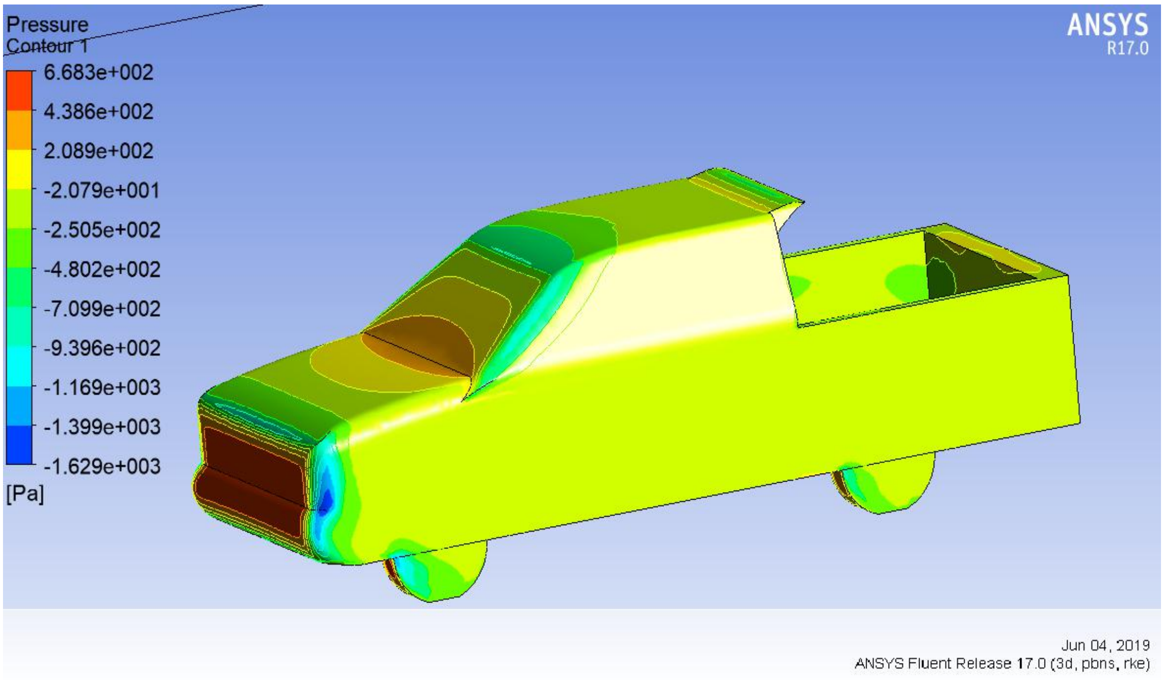

Figure 4.42. Pressure contour of model two at 120kmph

Pressure contour figures 4.40-4.42 show that the maximum pressure occurs at stagnation point colored by red on the grill of the vehicle. The second peak pressure occurs at the junction between the engine hood and the windshield. With increasing speed the maximum pressure increases. The increase in the surface pressure increases the drag coefficient which can be seen from table 4.3.

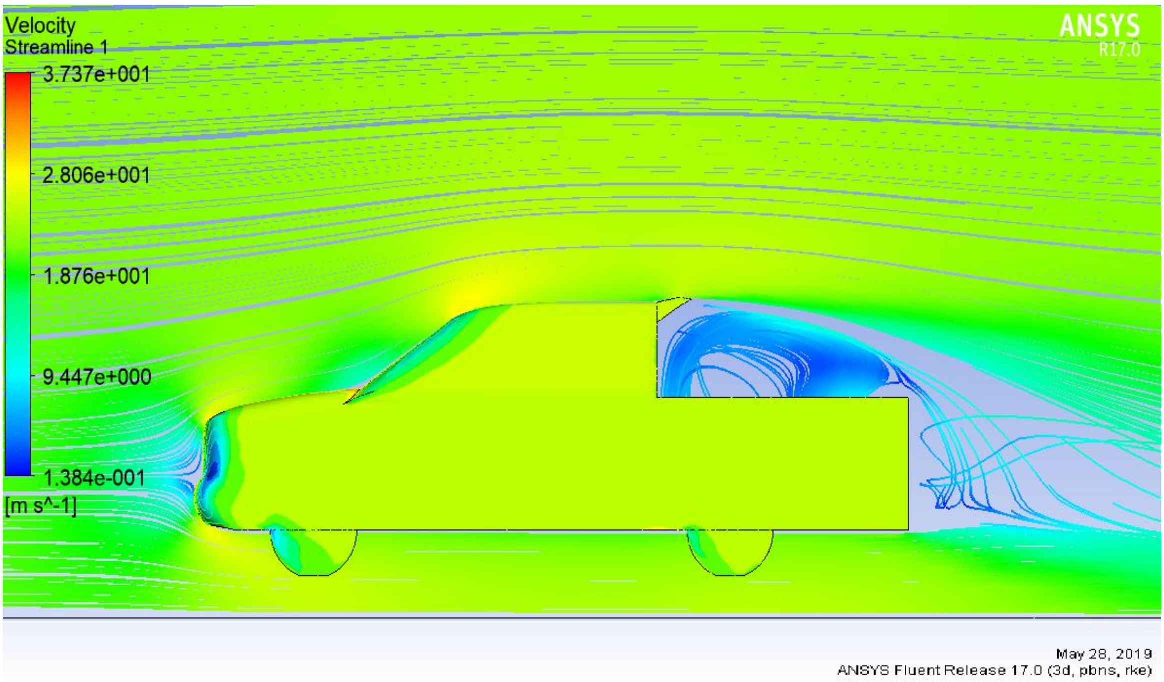

Figure 4.43. Velocity contour of model two at 80kmph

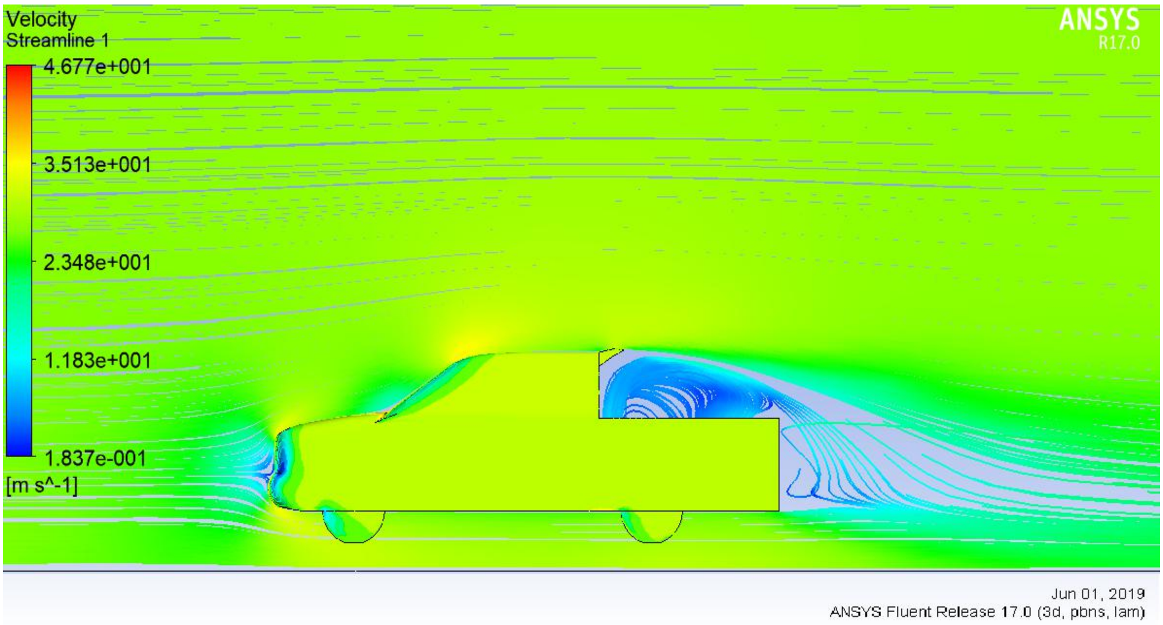

Figure 4.44. Velocity contour of model two at 100kmph

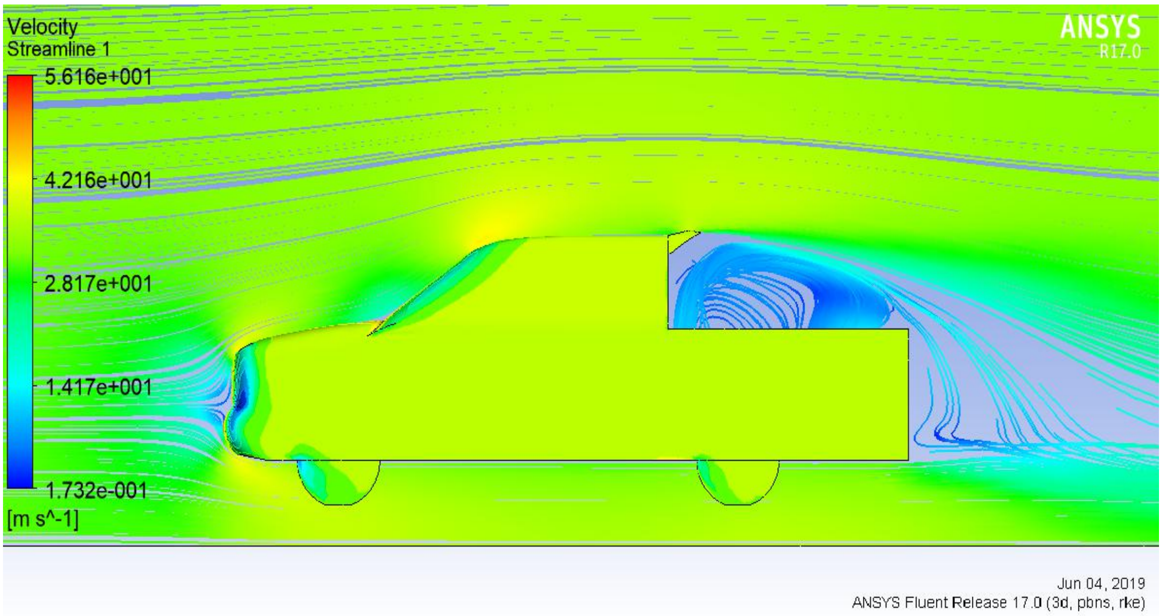

Figure 4.45. Velocity contour of model two at 120kmph

This model is baseline model attached with short spoiler on its rear roof end. The test procedure was the same as model one and model two. The scaled residuals were similar with the baseline model and model two. And the surface pressure distribution is the same in shape and fashion for all speeds.

We can see from the lift coefficient figures (figure 4.37-4.39) that the downward force increases sufficiently at higher speeds. The decrease in lift coefficient is higher than that of the baseline model and model one. So, at higher speeds at the expense of drag model two is stable than the other models.

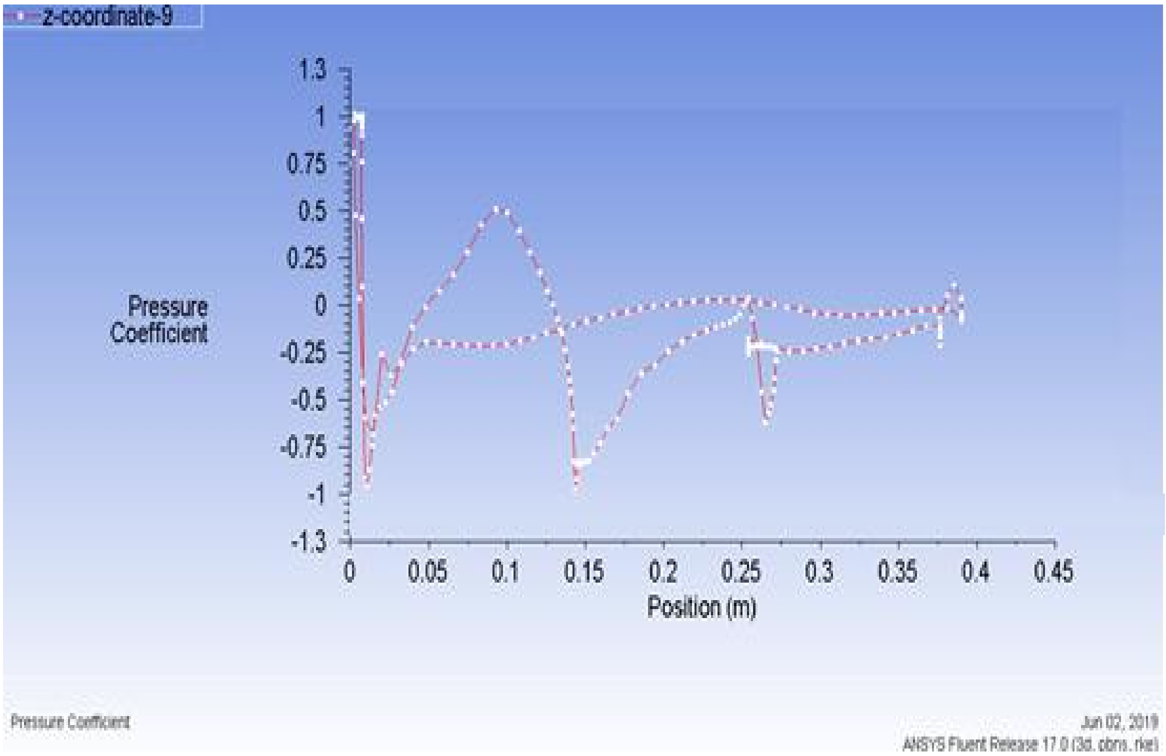

Figure 4.46. Surface pressure distribution for model two

Reduction in pressure on the surface of the spoiler can be seen from the pressure contour and surface pressure distribution figures (figure 4.40-4.42 and figure 4.46). However, the reduction on model two is only limited to the rear tip of the spoiler. The amount in reduction is low that its influence on the downward force is reduced, which can be seen at lift coefficient decrement which is higher than that of model one.

4.4 Model Three

4.4.1 Results

Result of scaled residuals, drag and lift coefficient, pressure and velocity contour at speed of 80kmph 100kmph and 120kmph for model four are depicted.

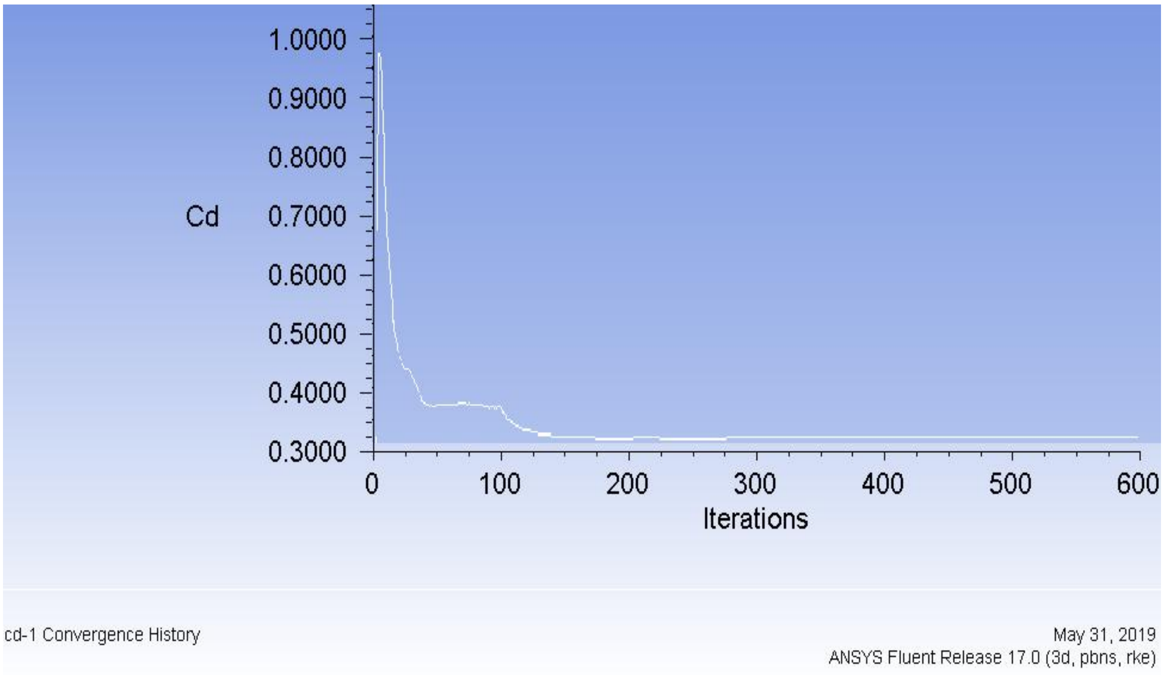

Figure 4.47. Drag coefficient of model three at 80kmph

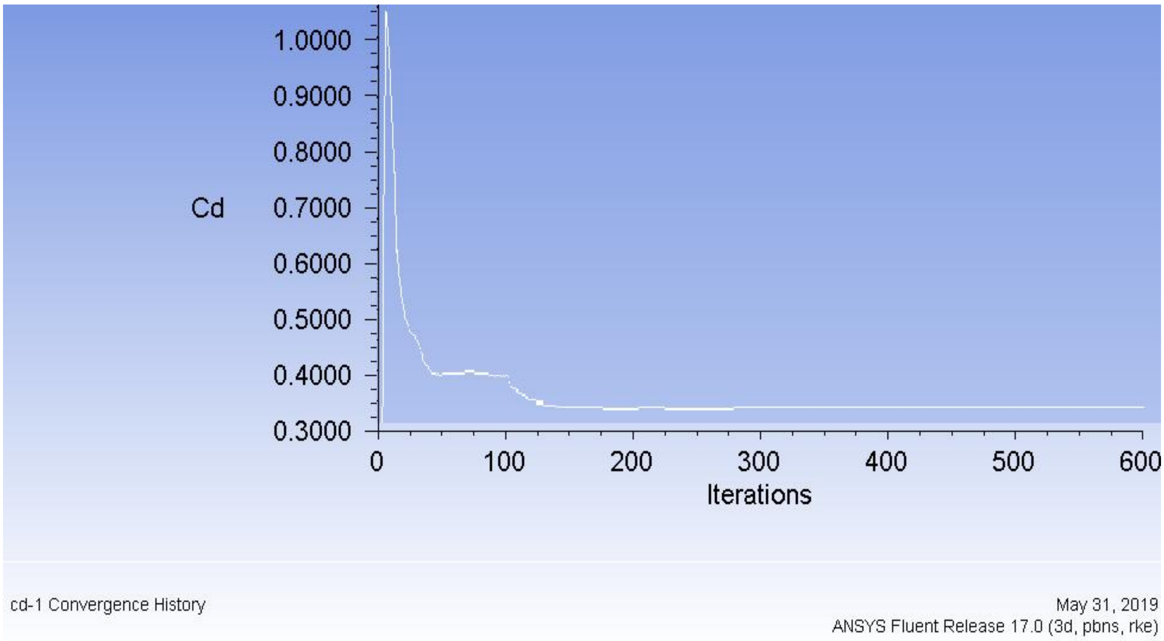

Figure 4.48. Drag coefficient of model three at 100kmph

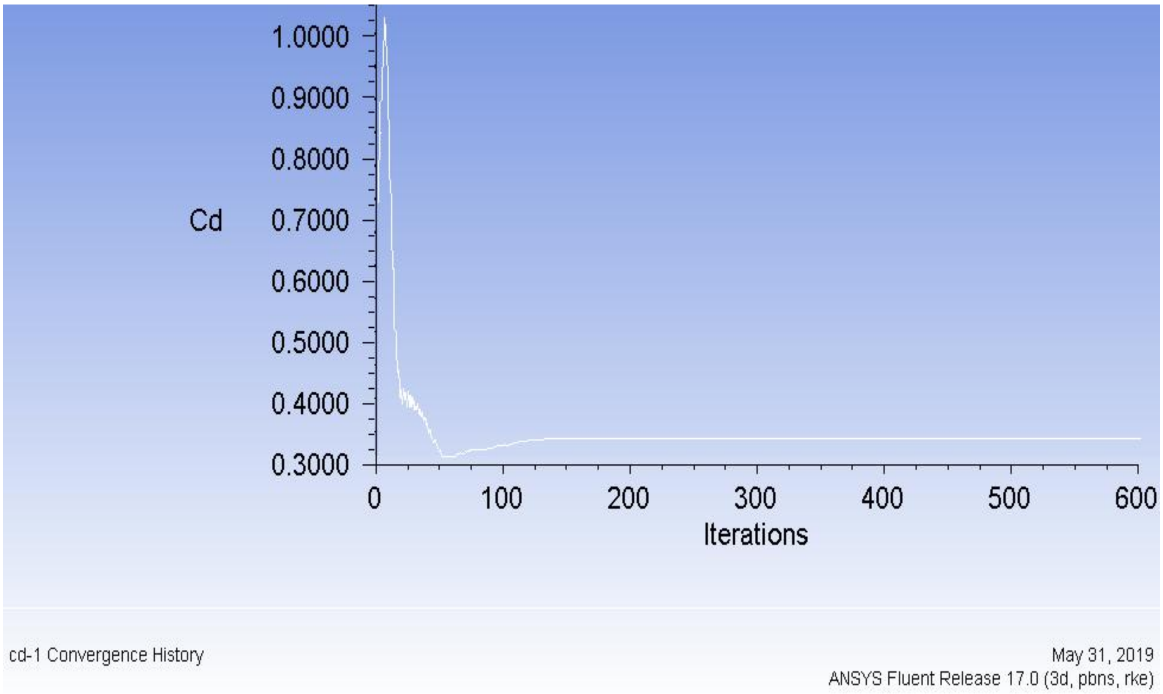

Figure 4.49. Drag coefficient of model three at 120kmph

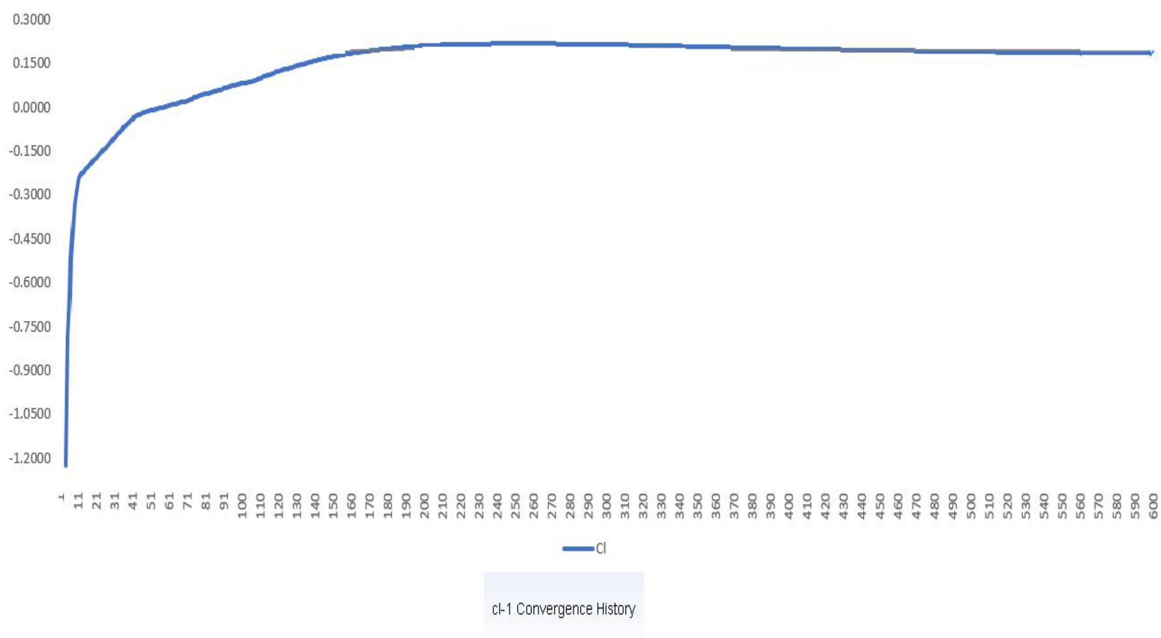

Figure 4.50. Lift coefficient of model three at 80kmph

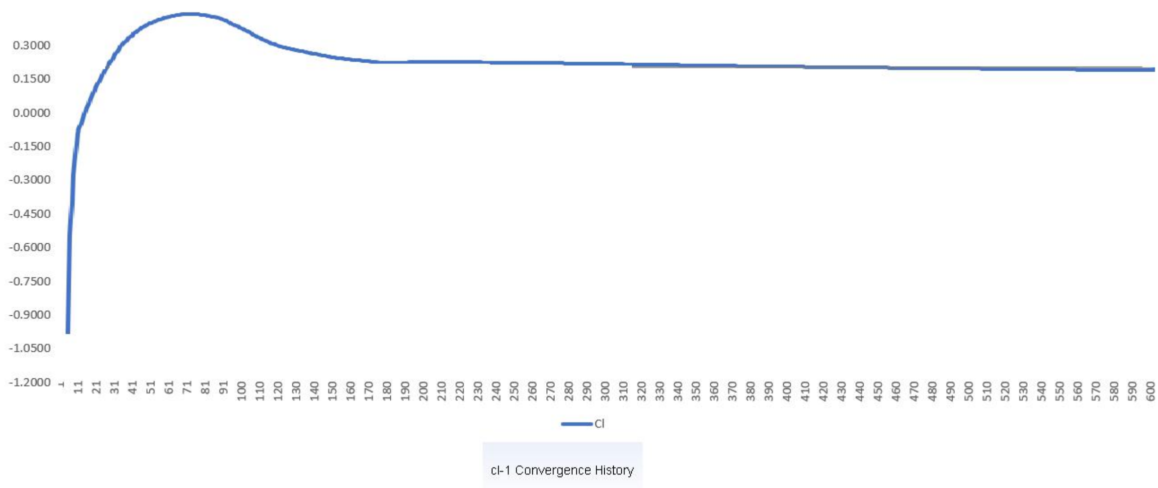

Figure 4.51. Lift coefficient of model three at 100kmph

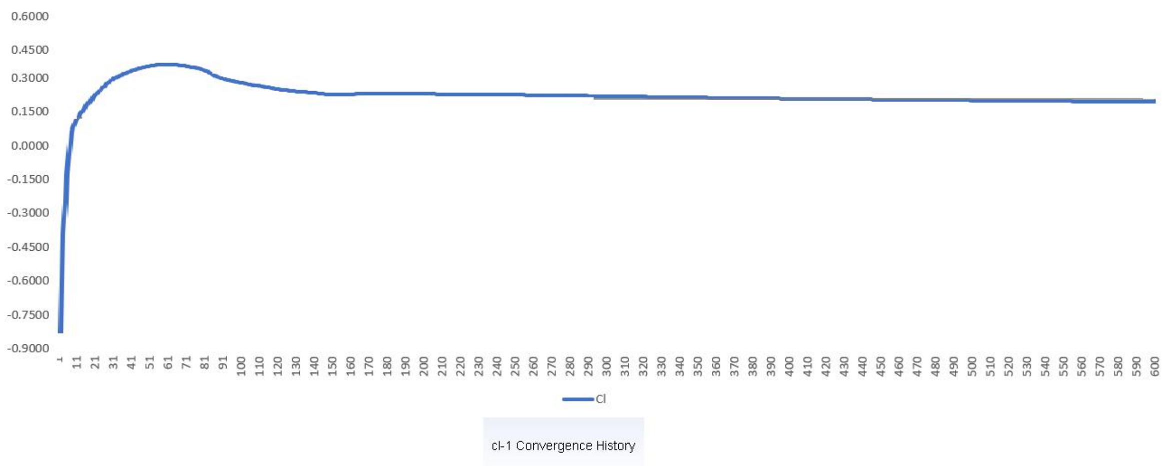

Figure 4.52. Lift coefficient of model three at 120kmph

Table 4.4. Drag and lift coefficient of model three at different speed

Model	Speed(kmph)	*Cd*	Cl
Model Three	80	0.3235	0.1848
	100	0.3266	0.1887
	120	0.3346	0.1795

The reduction in drag coefficient for this model is higher than that of baseline model but, less than the two other models (figure 4.47-4.47). It is known that the drag coefficient increases with increasing speed, these also holds true for model three. The lift force decreases (figure 4.50-4.52) as its speed increases thereby improving the stability of the model at higher speed. Figure 4.50-4.52 show how the lift coefficient converges with each iteration. Table 4.4 shows the converged values of drag and lift coefficients.

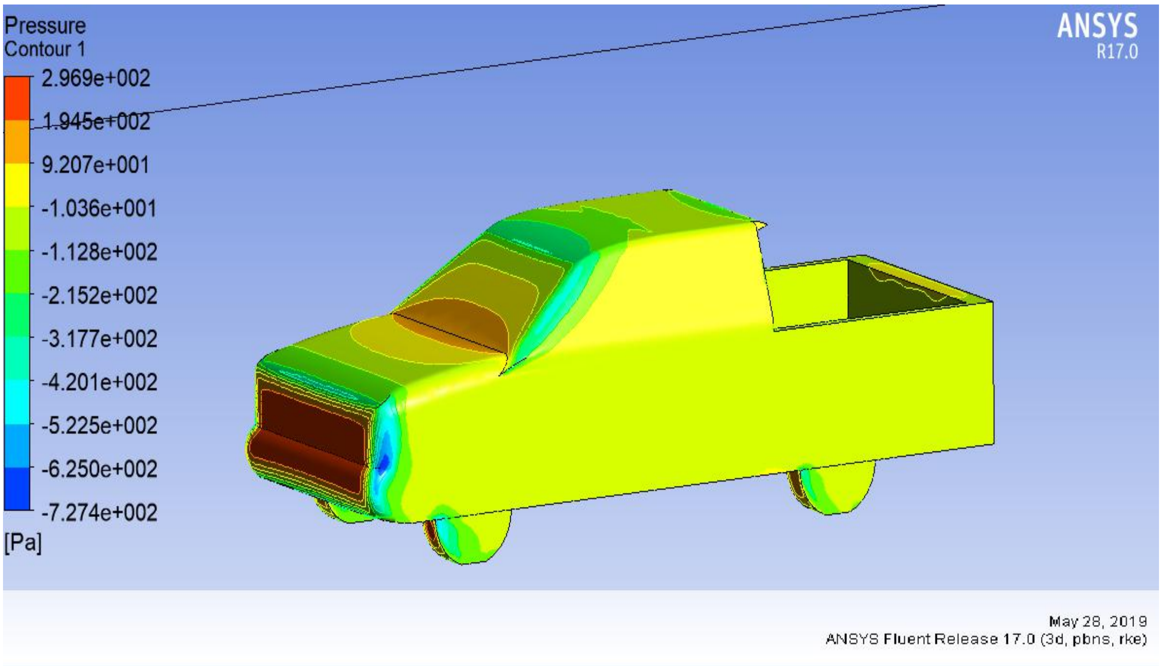

Figure 4.53. Pressure contour of model three at 80kmph

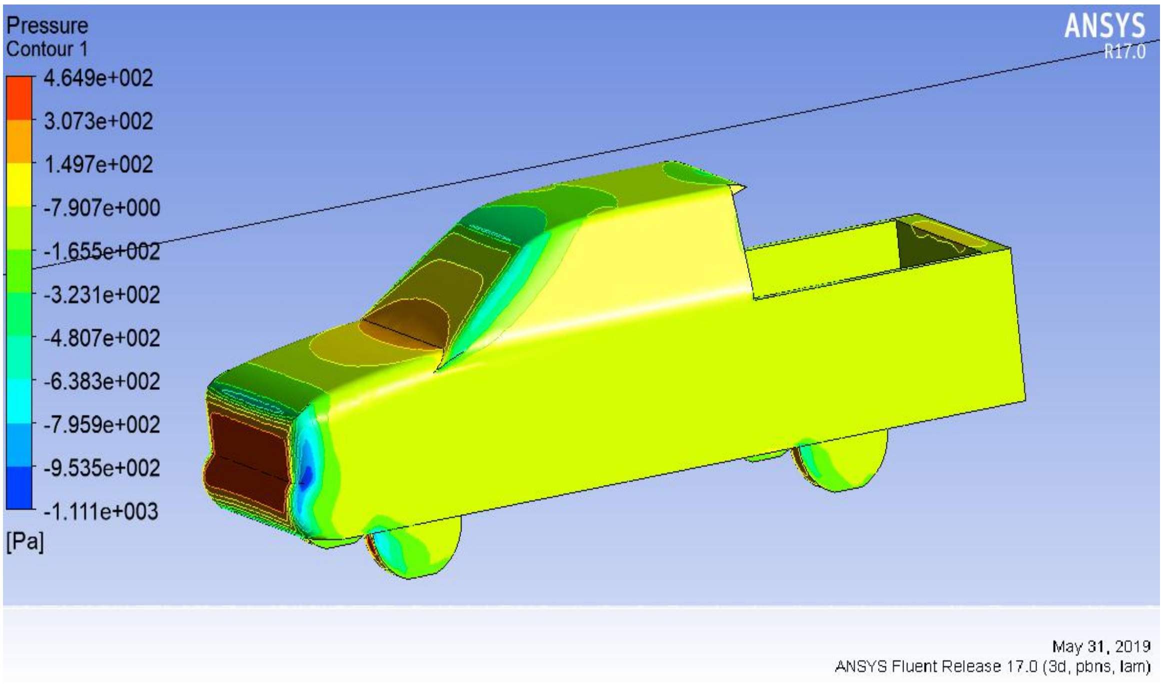

Figure 4.54. Pressure contour of model three at 100kmph

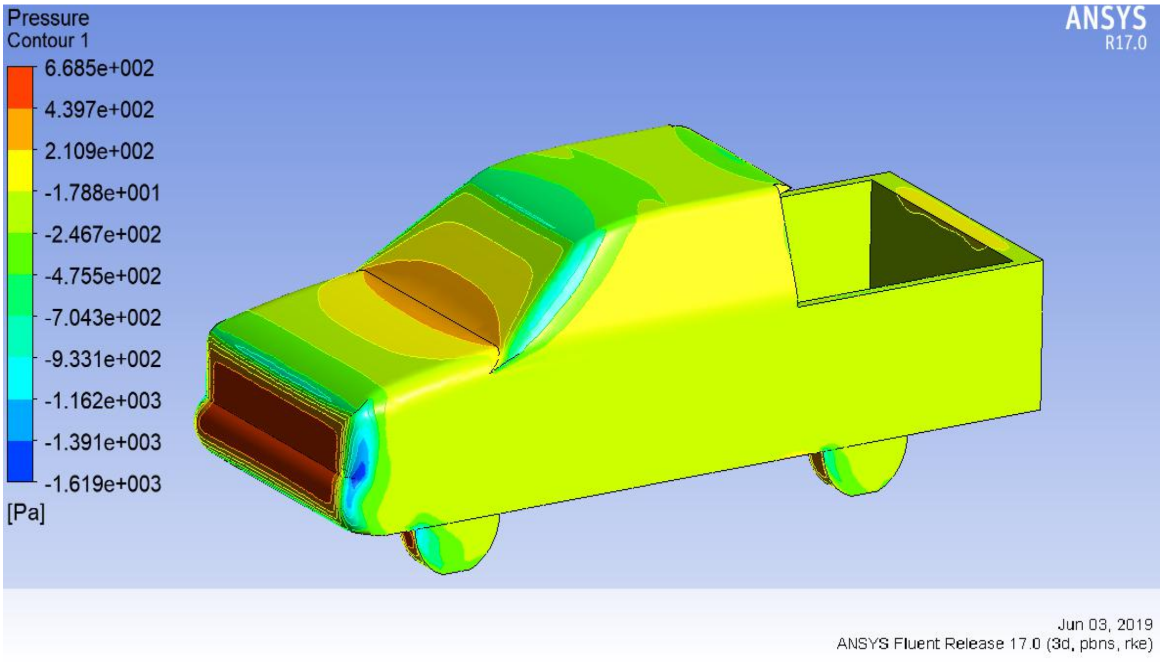

Figure 4.55. Pressure contour of model three at 120kmph

The pressure distribution o the surface of model three is shown in figures 4.53-4.55. From the figures we can see that how the pressure increases with increasing speed. The drag coefficient of model three increases with the increasing of speed. The increase in the amount of drag is because of the increase in the amount of forward resistant force which increases the pressure on the vehicle.

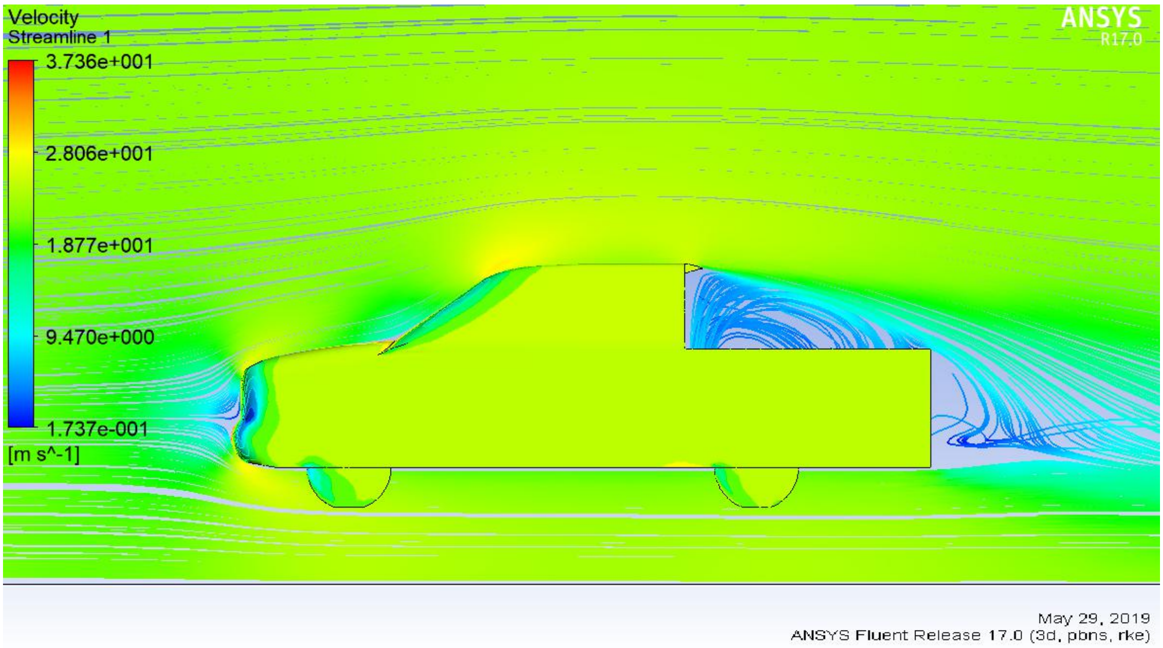

Figure 4.56. Velocity contour of model three at 80kmph

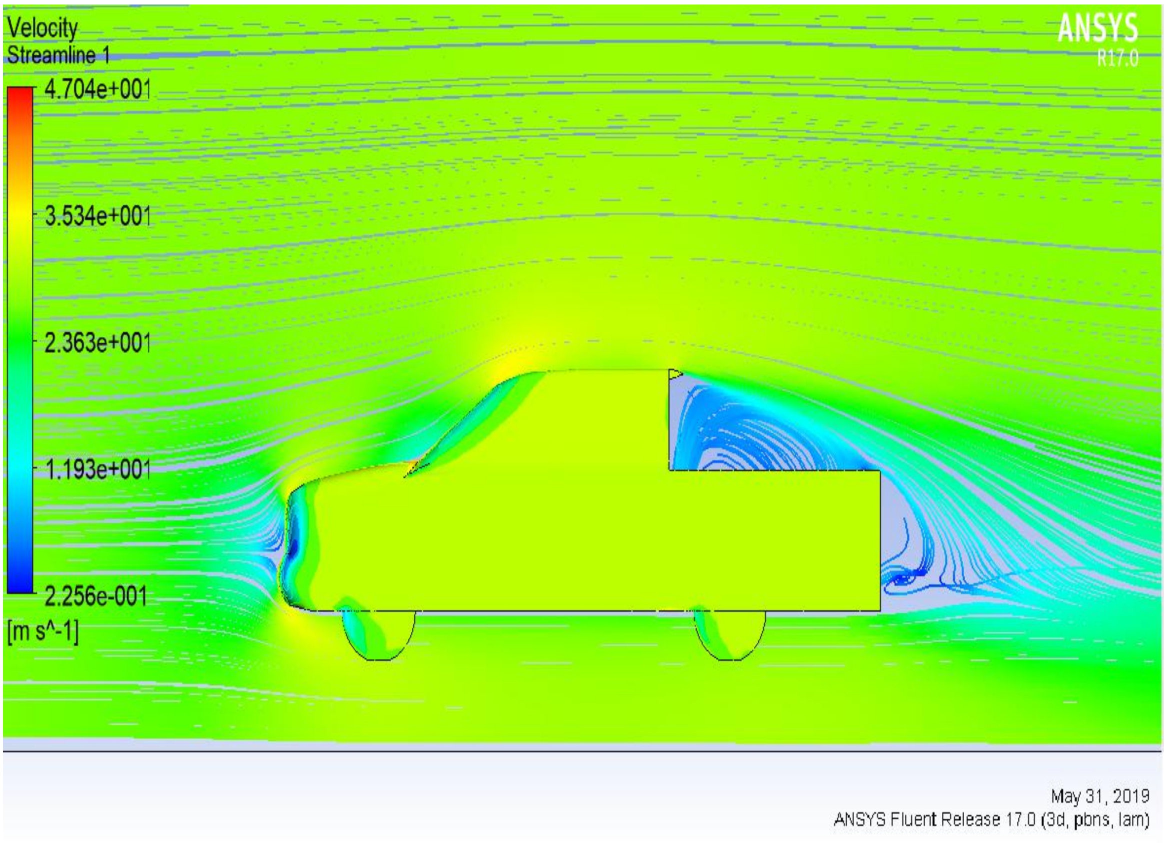

Figure 4.57. Velocity contour of model three at 100kmph

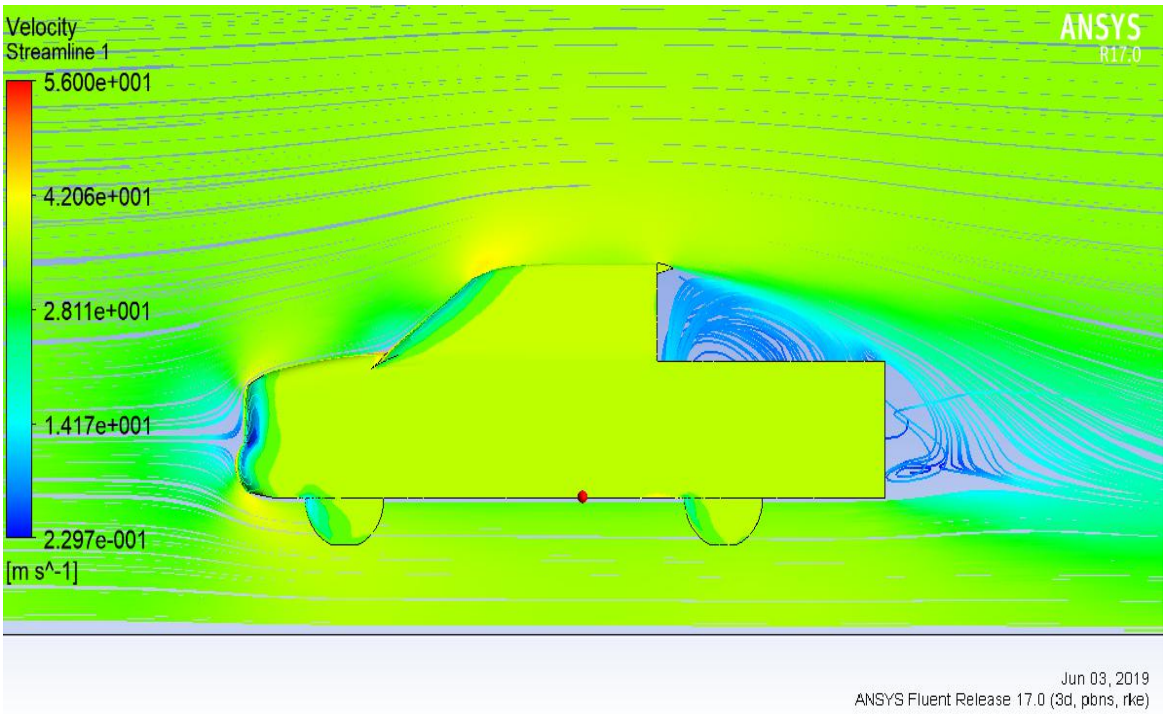

Figure 4.58. Velocity contour of model three at 120

This model is the last model in the study. This model is the same as that of model one the only difference being the short spoiler. Here also the scaled residuals are the same as that of the baseline model. The simulation and other analysis carried out is the same as all other models. The surface pressure distribution on the model is the same for all speeds. They all resemble in shape and fashion. From the velocity streamline contour, we ca see that the wake region gets stronger and wider as the speed increases. However, the wake region of model three is smaller than that of model two.

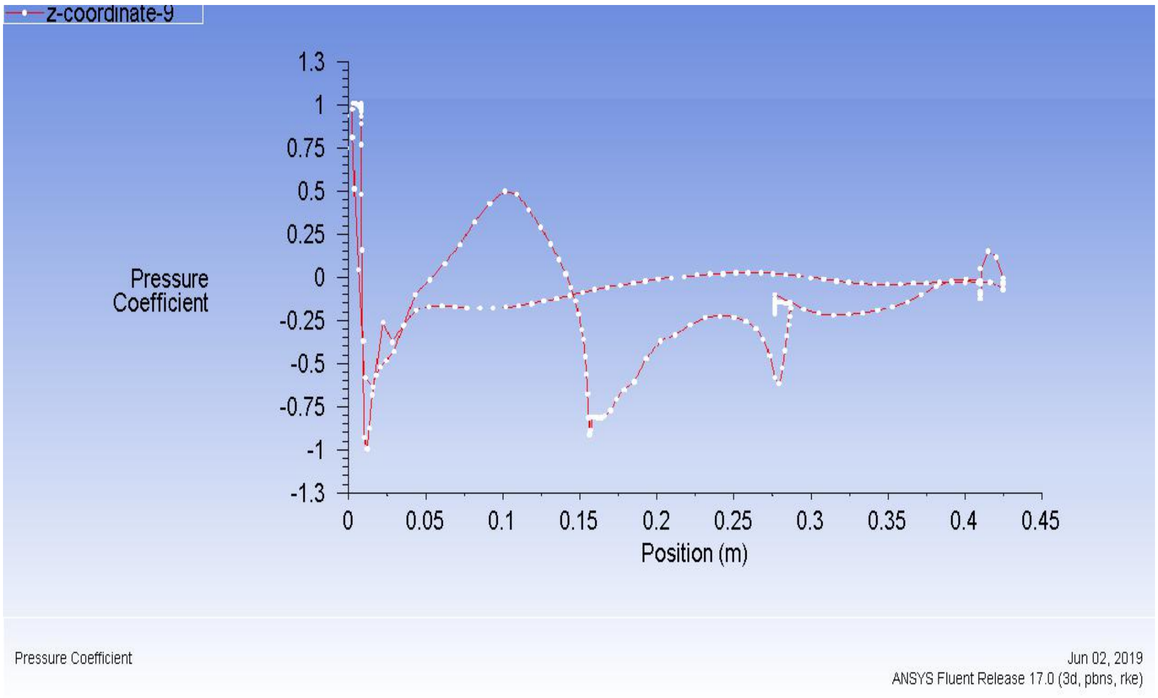

Figure 4.59. Surface pressure distribution along symmetry plane for model three

The surface pressure distribution changes on the surface of the model changes between maximum and minimum values. The pressure reduction on the spoiler is less than the baseline model and model one. In which case the amount of downward force is higher than both model one and baseline model. The change in the surface pressure on the body of model three can be seen from figure 4.59 above.

4.5 Comparison Between Models

From the graphs below the difference in drag and lift coefficient at 80kmph, 100kmph and 120kmph between all four models can be seen.

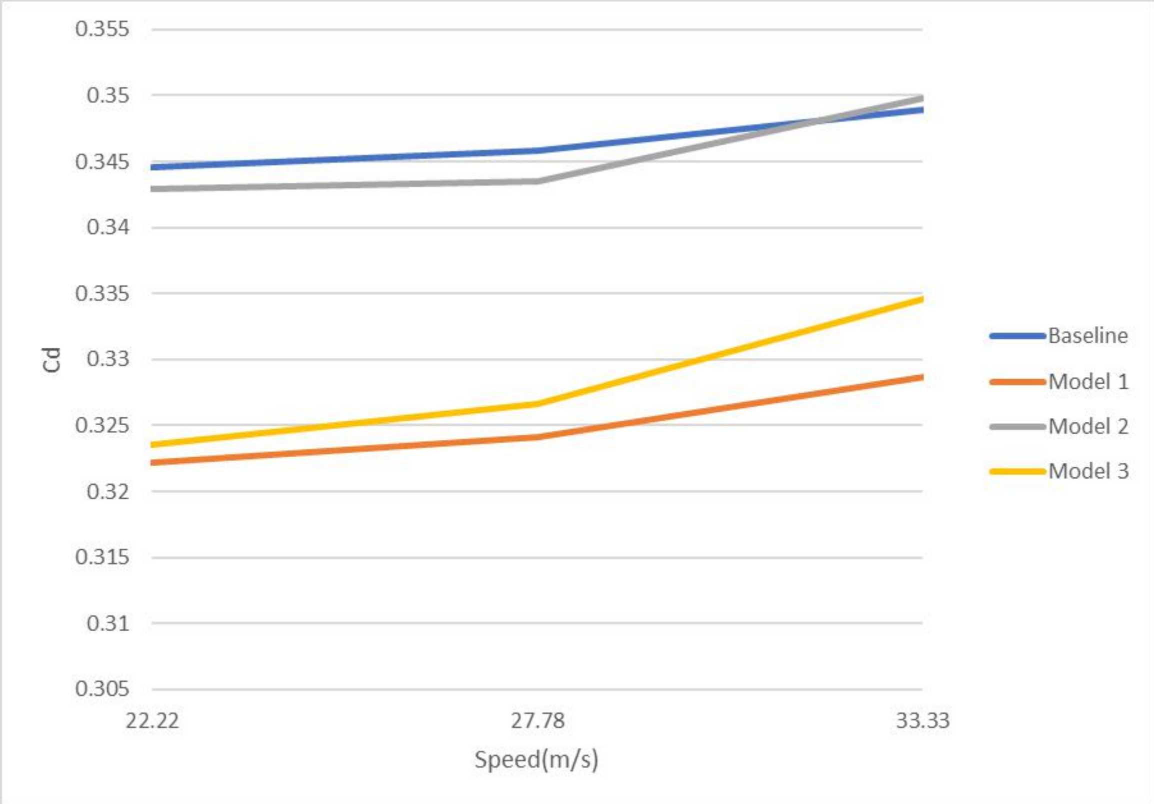

Figure 4.60. Drag coefficient of models at different speed

The drag coefficient of all models increases as their speed increases (figure 4.60). However, the slope is different for each model. The graph shows that the drag rises quickly at higher speeds. The quick rise in the slope is higher for model three than the other three models. Model two has low drag than baseline model, but as the speed approaches 120kmph the drag coefficient of model two starts to rise above the baseline model. At low speed model two has the lowest drag amount and the baseline model has the highest drag coefficient, and at speed about 120kmph model one has still the lowest amount of drag whereas model two has the highest drag. So, because of the reduced drag coefficient at both low and high speed model one saves more fuel and has less environmental effect because of its reduced fuel consumption and reduced emission.

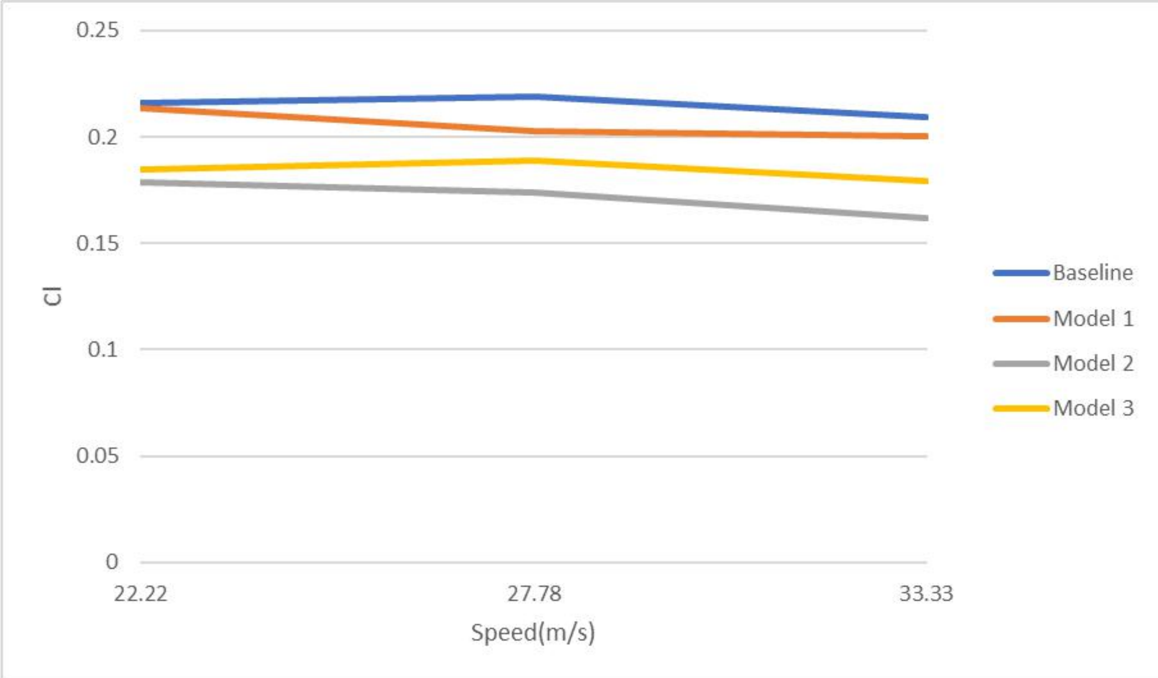

Figure 4.61. Lift coefficient of Models at different speed

For improved stability of vehicle at higher speeds the downward force should be high which is the result of reduced lift coefficient. From the figure 4.61, model two has the least lift coefficient which makes it the most stable of all model at high speeds. Least stable is baseline model with the highest lift force. The lift coefficient of all models decreases with increasing speed except for model one. Closely looking at the lift coefficient of model reveals that above the speed of 100kmph the lift coefficient starts to rise. Even if model one has the lowest of all drag coefficient, at high speeds the amount of lift gradually increases which affects the stability of the model. Hence, based on the result of the lift coefficient of all model's model two is the most stable model.

Table 4.5. Comparison of drag

	Models						
Speed (m/s)	**Baseline Cd**	**Model 1 Cd**	***% diff. from Baseline***	**Model 2 Cd**	***% diff. from Baseline***	**Model 3 Cd**	***% diff. from Baseline***
22.22	0.3446	0.3222	*-6.500290*	0.3429	*-0.493325*	0.3235	*-6.123047*
27.78	0.3458	0.3241	*-6.275303*	0.3435	*-0.665124*	0.3266	*-5.552342*
33.33	0.3489	0.3287	*-5.789624*	0.3498	*0.257953*	0.3346	*-4.098596*

Table 4.5 above summarizes the drag coefficient for the studied configuration along with the percentage difference from the Baseline case. Compared to the Baseline model, the entire studied configuration reduces the drag which is represented as drag coefficient. At

80kmph model one has the maximum improvement in drag reduction of 6.50% followed by model three with a drag-reduction improvement of 6.12%. The least improvement in drag reduction is achieved by model two which is 0.493%.

At 100kmph model one has the best drag reduction of 6.27%, model three has 5.55% drag reduction from the baseline model which is better than that of model two which has only 0.66% reduction.

At speed of 120kmph model one still has the maximum improvement in drag reduction by 5.78% followed by model three with a drag reduction improvement of 4.09%. At this speed the drag coefficient of model two has reached a point where it exceeds the drag coefficient of baseline model. So, driving model two at speed near and above 120kmph will increase the drag coefficient more than the baseline model.

Table 4.6. Comparison of Lift

	Models						
Speed (m/s)	**Baseline Cl**	**Model 1 Cl**	***% diff. from Baseline***	**Model 2 Cl**	***% diff. from Baseline***	**Model 3 Cl**	***% diff. from Baseline***
22.22	0.2157	0.2134	*-1.066291*	0.1789	*-17.06073*	0.1848	*-14.32545*
27.78	0.2188	0.2027	*-7.358099*	0.1741	*-20.42961*	0.1887	*-13.75688*
33.33	0.2091	0.2001	*-4.304160*	0.1621	*-22.47728*	0.1795	*-14.15590*

Table 4.6 above summarizes the lift coefficient of all models along with the percentage difference from the baseline model which were studied in this thesis. Model two has the maximum improvement in lift coefficient by 22.47% at 120kmph. At this speed the lift improvement for model one is 4.30% and for model three it is 14.15%. The least lift improvement at 80kmph is 1.06% which corresponds to model one, for the same speed the percentage lift coefficient difference from the baseline model is 17.06% for model two and 14.32% for model three. It is shown in the table above that model one has reduced the baseline lift by 7.35% at 100kmph. Whereas, model two and three have improved the amount of lift by 20.42% and 13.75% respectively.

Close investigation on the lift coefficient of model one reveals that the lift decreases as the speed increases to 100kmph, but further speeding increases the lift coefficient. So, as the speed of the model approaches 120kmph the stability of the vehicle is compromised because of the decrease in downward force.

4.6 Calculation of Fuel Consumption

Using formula from Bitchtas, D. [59] fuel saving of the given model relative to baseline model can be calculated. Percentage fuel reduction is three fifth of percentage of total drag reduction. The calculated values are given in the table below.

Table 4.7 Fuel Consumption Reduction

Model	speed(m/s)	% diff. from Baseline	Percent of Fuel Saving
Baseline	22.22		
	27.78		
	33.33		
Model One	22.22	-6.500290192	3.900174115
	27.78	-6.275303644	3.765182186
	33.33	-5.789624534	3.473774721
Model Two	22.22	-0.493325595	0.295995357
	27.78	-0.665124349	0.39907461
	33.33	0.257953568	-0.154772141
Model Three	22.22	-6.123041207	3.673824724
	27.78	-5.552342394	3.331405437
	33.33	-4.098595586	2.459157352

From table 4.7 we can see that maximum fuel amount of 3.90% can be reduced in model one travelling at 80kmph. Model one reduces 3.76% and 3.47% of fuel when compared to baseline model at speed of 100kmph and 120kmph respectively. The other high reduction is from model three with 3.67%, 3.33% and 2.45% at speed of 80kmph, 100kmph and 120kmph respectively. Model two has the least fuel reduction with 0.29% at 80kmph, and 0.39% at 100kmph. But, when model two travels at speed approaching 120kmph, instead of reducing it consumes more amount of fuel than the baseline model.

CHAPTER FIVE

CONCLUSION AND RECOMMENDATIONS

5.1 Summary

Computational fluid dynamics was used to analyze flow around a 1/12 scaled down Toyota pickup vehicle. A steady state formulation was used in the present analysis. The objective of the present study was to reduce aerodynamic drag of pickup vehicles using spoiler. The spoiler was attached to rear end of the baseline model at various arrangements. Model one had a long spoiler attached to the rear end of the baseline model at zero inclination angle. Model two was baseline model with long spoiler attached at 12 degree upward to its rear roof end, and finally model three was similar with model one the only difference being short spoiler.

All models were modeled using SolidWorks. Analysis was completed in ANSYS using realizable k-epsilon turbulence modeling. It was found that the large circulation region was formed in the box of the baseline truck and it created large pressure difference between the front and the rear of the truck, causing high drag. Different arrangements of spoilers were attached and analyzed which were meant to push the flow separation a bit rearward and reduce the amount of drag by minimizing the wake region, and by throwing the turbulent air behind the vehicle.

Comparison of streamlines and contour was made between the results from Yang and Khalighi [13] and the present study and again comparison of surface pressure distribution was made between Pramod et al. [36] and present study. It was seen that the present study was able to capture the flow structure around the vehicle as accurately as Yang and Khalighi [13] and the surface pressure distribution between Pramod et al. [36] and present study was similar. Hence, present CFD simulation is validated against the CFD simulation of the same truck by Yang and Khalighi [13], and Pramod et al. [36].

5.2 Conclusion

After the analysis on all models, the spoiler minimized the amount of swirling air in the bed of the vehicle and hence reduced the amount of drag coefficient compared to baseline model. The highest improvement of aerodynamic coefficient (Cd) of 6.50% was achieved for model one. The reduction in the amount of drag coefficient have helped models one, two, and three, especially model one to reduce total fuel consumption by 3.90%. On all model the amount of drag has increased with increasing speed. So, with respect to the length of the spoiler it can be seen that the model with long spoiler has better drag reduction than the model with short spoiler. Therefore, it is possible to say increasing the length of the spoiler to 21mm has reduced the amount of drag coefficient. Whereas inclining the spoiler to 12 degree has helped to reduce the lift coefficient greatly, but the amount of drag has increased more than the model without spoiler at higher speeds. The lift coefficient was reduced as well in comparison with that of the baseline model except for model one which increased when speed approached 120kmph. On all other models the lift coefficient has decreased for increased speed making the vehicle more stable at high speeds.

5.3 Recommendations

- For more accurate results a computer with high processing speed and capacity is recommended. This kind of computer will help in improving mesh quality and reducing processing time.
- Further improvement in drag and lift coefficients can be made possibly using optimization software and/or using synergetic effect of different aerodynamic add-on devices such as Airdam, Sideskirts and any other.
- Further improvement can be made by designing brand new spoiler and analyzing its effect, and by changing the location and angle of the spoilers.

5.4 Future Research

Future researches can be done by designing the spoiler itself. In the present paper the spoilers were chosen from NACA airfoil catalogue. Once the spoilers are designed different attaching angles can be analyzed.

Wind tunnel experiment on the models analyzed here can be performed to compare with results stated in this work.

REFERENCES

[1] Eckermann, Erik (2001). *World History of the Automobile*. SAE Press. pp. 14. ISBN 9780768008005

[2] Firoz, Alam et al. (2010) *Effects of Vehicle Add-Ons on Aerodynamic Performance*, Proceedings of the 13th Asian Congress of Fluid Mechanics pp 186-189.

[3] Faerber, H. A. (1956) *Das Autobuch*, Offenburg, Burda, pp 231.

[4] Landman D., Wood R. M, Seay W. S., (2009) *Understanding Practical Heavy Truck Drag Reduction Limits*, USA SAE Paper No. 2009-01-2890.

[5] Alexander, Diehl et al. (2002), *Reducing Drag Forces in Future Vehicles*, Chalmers, University of Technology.

[6] Vivek, Yakkundi and Shankar, Mantha (2018) *Effect of Spoilers on aerodynamic properties of a car,* International Journal of Scientific Research and Review pp.271-280 ISSN NO: 2279-543X.

[7] Jiyan, Patel et al. (2017) *Fluid Dynamics Simulation of a Car Spoiler*, unpublished research proposal submitted to Chandubhai S Patel Institute of Technolgy, 11pp.

[8] Rubel, Chandra Dasa,and Mahmud, Riyada (2017) 'CFD Analysis of Passenger Vehicleat Various Angle of Rear End Spoiler', *10th International Conference on Marine Technology*. Pp. 160-165. Elsevier Ltd 1877-7058.

[9] Karthick, Bala et al. (2015) 'CFD Analysis and Optimization of a Car Spoiler', *International Journal of Mechanical Engineering and Research,* pp 128-133. ISSN 0973-4562 Vol. 5 No.1.

[10] Rakibul, Hassan (2014) 'Numerical Study on Aerodynamic Drag Reduction of Racing Cars', *10th International Conference on Mechanical Engineering*, pp. 308-313. Elsevier Ltd1877-7058.

[11] Kelbessa, Kenea and Kiran, Kumar (2016) 'Design and Analysis of a New Rear Spoiler For SUV Vehicle Mahindra Bolero Using CFD', *IRJET*, pp. 914-924. e-ISSN: 2395 -0056.

[12] Sathish, Kumar et al. (2017) 'Design, Analysis and Manufacturing of a Car Rear Spoiler for Drag Reduction', *IARJSET*, pp. 89-96. ISSN (Print) 2394-1588.

[13] Zhigang, Yang and Bahram, Khalighi (2005) 'CFD Simulations for Flow over Pickup Trucks', General Motors Corporation, Society of Automotive Engineers. 2005-01-0547.

[14] Jeong, Jae (2016) 'Salient drag reduction of a heavy vehicle using modified cab-roof fairings', *Journal of Wind Engineering and Industrial Aerodynamics*, pp. 138-151. Elsevier 0167-6105.

[15] Chaitanya, Chilbule et al. (2014) 'Analyzing the profile modification of truck-trailer to prune the aerodynamic drag and its repercussion on fuel consumption', *12th Global Congress on Manufacturing and Management*, pp. 1208-1219. Elsevier 1877-7058.

[16] Alamaan, Altaf (2014) 'Passive drag reduction of square back road vehicles', *Journal of Wind Engineering and Industrial Aerodynamics*, pp. 30-43. Elsevier 0167-6105/& 2014.

[17] Mohab, Hassaan (2018) 'On the Effect of Boat Tails on a Simplified heavy Vehicle Geometry Under Crosswind', *Journal of Wind Engineering and Industrial Aerodynamics,* pp. 172-186. Elsevier 0167-6105.

[18] Chunhui, Zhang (2017) 'Full Vehicle CFD Investigation on the Influence of Front end configuration on radiator performance and cooling drag', *Applied Thermal Engineering*, pp.1328-1340. Elsevier 1359-4311.

[19] A. Premoli,et al. (2016) 'Comparison between steady and moving railway vehicles subjected to crosswind by CFD analysis', *Journal of Wind Engineering and Industrial Aerodynamics* pp. 30-40. Elsevier 0167-6105.

[20] Ping, He (2018) 'An aerodynamic design optimization framework using a discrete adjoint approach with Open FOAM', *Computers and fluids*, pp. 286-303. Elsevier 0045-7930.

[21] T. Avadiar et al. (2018) 'Characterization of the wake of the Driver estate vehicle', *Journal of Wind Engineering and Industrial Aerodynamics*, pp. 243-259 Elsevier 0167-6105.

[22] S. Luckhursta et al. (2018) 'Computational investigation into the sensitivity of a simplified vehicle wake to small base geometry changes', *Journal of Wind Engineering and Industrial Aerodynamics*, pp. 2-15. Elsevier 0167-6105.

[23] Sumit, Krishnan (2016) ‘Investigating the Drag Coefficient of Scaled Model Car by Using Wind Tunnel’, *IJRET*, pp. 16-19. eISSN: 2319-1163 | pISSN: 2321-7308.

[24] V. Malviya (2008) ‘comparative computational analysis of drag-reducing devices for tractor-trailers, *University of Huddersfield UnitedKingdom*.

[25] Upendra and S. Rohatgi (2012) ‘Methods of Reducing Vehicle Aerodynamic Drag’, *ASME 2012 Summer Heat Transfer Conference,* Puerto Rico, USA.

[26] Giacomo, R. et al. (2017) ‘Aerodynamic performances of rounded fast back vehicle’, *Journal Automobile Engineering*, Vol.231(9)1211–1221.

[27] Ram, Bansal and R.B,.Sharma (2014) ‘Drag Reduction of Passenger Car Using Add-On Devices’, *Journal of Aerodynamics Volume*, Hindawi Publishing. ArticleID678518.

[28] Hyeon-Seok, Shim et al. (2017) ‘Optimization of bobsleigh bumper shape to reduce aerodynamic drag’, *Journal of Wind Engineering &Industrial Aerodynamics*, Elsevier 164(2017)108–118.

[29] Ziyu, Guo et al. (2018) ‘Optimization of the aerodynamic drag reduction of a passenger hatchback car’, *Journal of Aerospace Engineering* Proc IMechE Part G 0(0)1–18.

[30] Yiping, Wang et al. (2016) ‘Reduction in the aerodynamic drag around a generic vehicle by using a non-smooth surface’, *Journal Automobile Engineering*, Vol. 231(1) 130–144.

[31] Xu, Gong et al. (2014) ‘Surrogate model for aerodynamic shape optimization of a tractor-trailer in crosswinds’, *Automobile Engineering*, Elsevier 226(10)1325–1339.

[32] Cooper K R. (2006) ‘Full-Scale Wind Tunnel Tests of Production and Prototype, Second-Generation Aerodynamic Drag Reducing Devices for Tractor-Trailers’, SAE Paper No.2006-01-3456, USA.

[33] Abdellah, Ait et al. (2015) ‘Aerodynamic Drag Reduction for a Generic Truck Using Geometrically Optimized Rear Cabin Bumps’, *Journal of Engineering*, Volume 2015, Article ID 789475. Pp. 1-14.

[34] J, Ha et al. (2009) 'Flow characteristics of a pickup truck with regard to the bed geometry variation', *Automobile Engineering*, pp. 881-891. DOI: 10.1243/09544070JAUTO1427.

[35] A Tewari. (2007) 'Atmospheric and Space Flight Dynamics'. *Lecture Notes in Mathematics*. *Chapter 10 Elements of Aerodynamics* pp. 233-267, Springer.

[36] Pramod, Krishnani et al. (2009) 'CFD Analysis of Drag Reduction Using External Devices on Pickup Trucks', *Proceedings of the 2010 ASME International Mechanical Engineering Congress & Exposition*, pp. 1-11. IMECE2010-39732.

[37] Wolf-Heinrich, Hucho and Gino Sovran (2006) 'Aerodynamics of Road Vehicles', Annual Revisions Fluid Mechanics, pp. 485-537. 0066-4189/93/0115-04855.

[38] Mohsen, Jahanmiri (2010) 'Active Flow Control: A Review', *Research report*, Printed at Chalmers Reproservice, pp. 1-33. ISSN 1652-8549.

[39] Seifert, A., Pack, L. G., (2002) "Active control of separated flow on a wall-mounted ''hump'' at high Reynolds numbers" AIAA J 2002;40(7):1363–72.

[40] Wright, M.C.M. and Nelson, P.A., (2001) Wind tunnel experiments on the optimization of distributed suction for laminar flow control, Proceedings of the Institution of Mechanical Engineers Part G: Journal of Aerospace Engineering, G215(6), 343-54.

[41] Choi, H., Jeon, W.-P., and Kim, J., (2008) "Control of Flow over a Bluff Body," Annual Review of Fluid Mechanics, Vol. 40, pp. 113–139.

[42] Schoppa, W., and Hussain, F., (1998) "A Large-Scale Control Strategy for Drag Reduction in Turbulent Boundary Layers," Phys. Fluids 10, pp. 1049–1051.

[43] Bellman, Agarwal M., Naber R., and Chusak,L. (2010) "Reducing energy consumption of ground vehicles by active flow control." American Society of Mechanical Engineers, 2010.

[44] Kourta, A., and Gilliéron, P. (2009) "Impact of the automotive aerodynamic control on the economic issues", Journal of Applied Fluid Mechanics, Vol.2 (2), pp69-75.

[45] Kourta, and Leclerc, C. (2013) "Characterization of synthetic jet actuation with application to Ahmed body wake".

[46] Park, J. H., Lee, J., and Kim, K. H. (2013) Aerodynamic drag reduction of Ahmed model using synthetic jet array,SAE International Journal of Passenger Cars-Mechanical Systems.

[47] Hahba, T., Springer, M., Lienhart, H., Kniesburges, and Becker, S. (2012) "passive flow control" on a car model, In 16th Int Symp on Applications of Laser Techniques to Fluid MechanicsLisbon, Portugal.

[48] André, Bakker (2006) 'Boundary Layers and Separation', *Applied Computational Fluid Dynamics, Lecture note*, http://www.bakker.org, AndréBakke ©Fluent Inc.pp. 1-39.

[49] Ahmed Ramm G. "Some Salient Features of the Time – Averaged Ground Vehicle Wake", SAE Technical Paper, 1984

[50] Saurabh, Banga et al. (2015) 'CFD Simulation of Flow around External Vehicle: Ahmed Body', Journal of Mechanical and Civil Engineering, pp. 87-94. Volume 12, Issue 4 Ver. III, e-ISSN: 2278-1684, p-ISSN: 2320-334X.

[51] Pletcher R. H., J. C. Tannehill, and, D. A. Anderson, 2013. "Computational Fluid Mechanics and Heat Transfer", CRC Press, New York.

[52] Matt, Cable (2009) '*An Evaluation of Turbulence Models for the Numerical Study of Forced and Natural Convective Flow in Atria'*, unpublished thesis submitted to Queen's University Kingston, Ontario, Canada p. 148.

[53] Launder, B. E., Spalding, D. B., *Lectures in Mathematical Models of Turbulence*, Academic Press, 1972.

[54] Yakhot, V., Orszag, S. A., "Renormalization Group Analysis of Turbulence: Basic Theory", *Journal of Scientific Computing*, 1(1):1-51, 1986.

[55] Shih, T.-H., Liou, W.W., Shabbir, A., Yang, Z., and Zhu, J., 1995, "A New - Eddy-Viscosity Model for High Reynolds Number Turbulent Flows - Model Development and Validation.", *Computers Fluids*, 24(3):227-238.

[56] Wilcox, D. C., 1998, "Turbulence Modeling for CFD," DCW Industries, Inc., La Canada, California.

[57] Menter, F.R., 1994, "Two-Equation Eddy-Viscosity Turbulence Models for Engineering Applications," *AIAA Journal*, 32(8):1598-1605.

[58] Marco, Lanfrit (2005) 'Best practice guidelines for handling Automotive External Aerodynamics with FLUENT', *Fluent Deutschland GmbH Birkenweg,* 14a. 64295 Darmstadt/Germany.

[59] Bitchtas, D. (2012) *Aerodynamic evaluation of heavy trailer upper surface curvature*, unpublished Master's thesis submitted to Cranfield University.

APPENDICES

Appendix A: Models inside Enclosure and Mesh

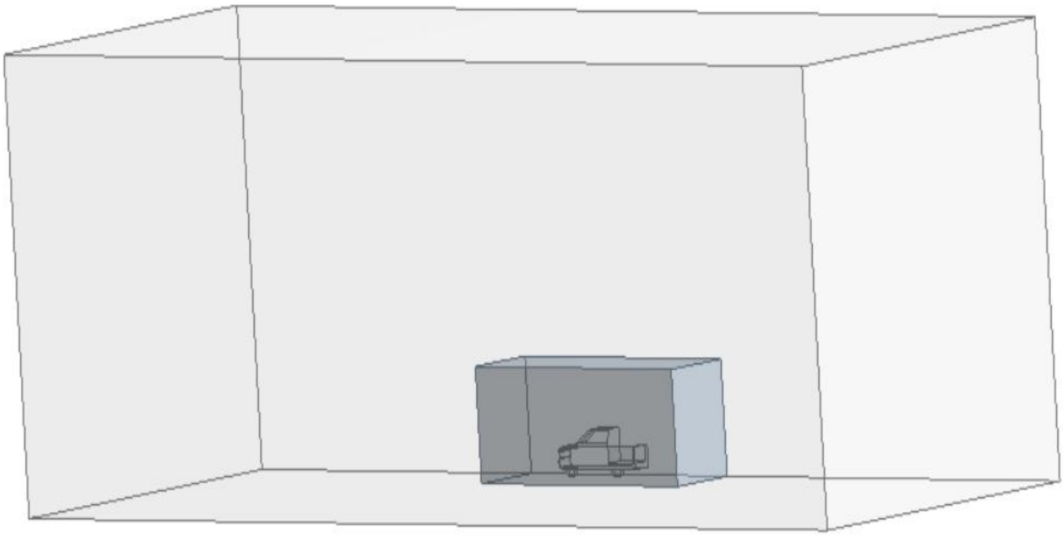

Figure A-1.Baseline model inside enclosure

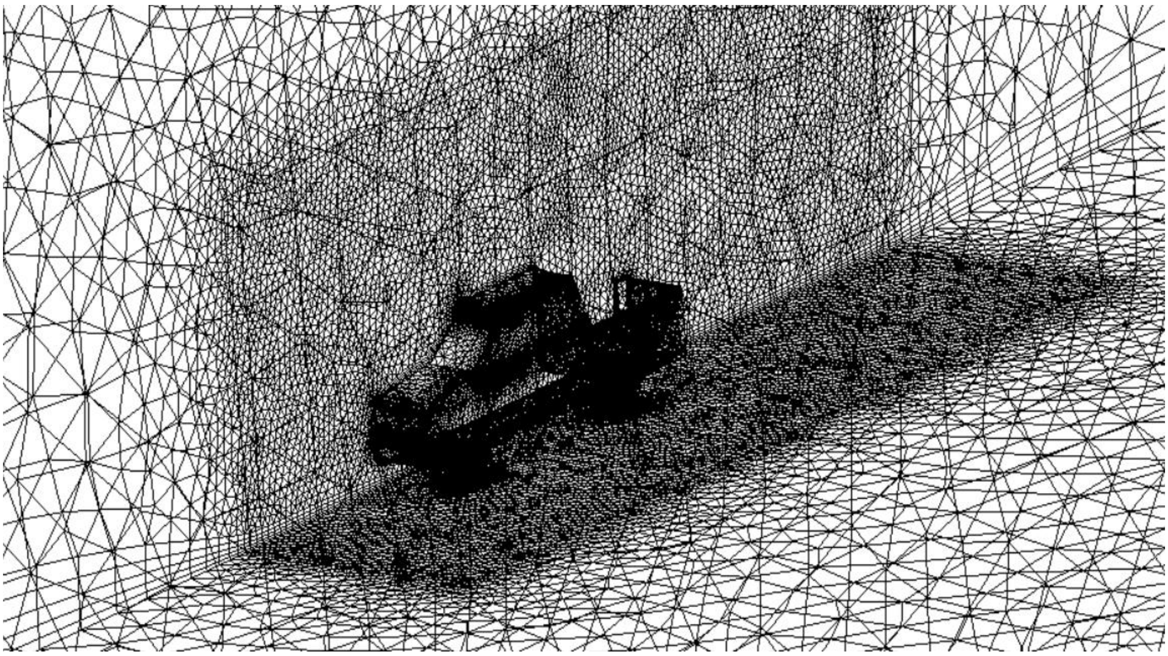

Figure A-2. Baseline model after meshing

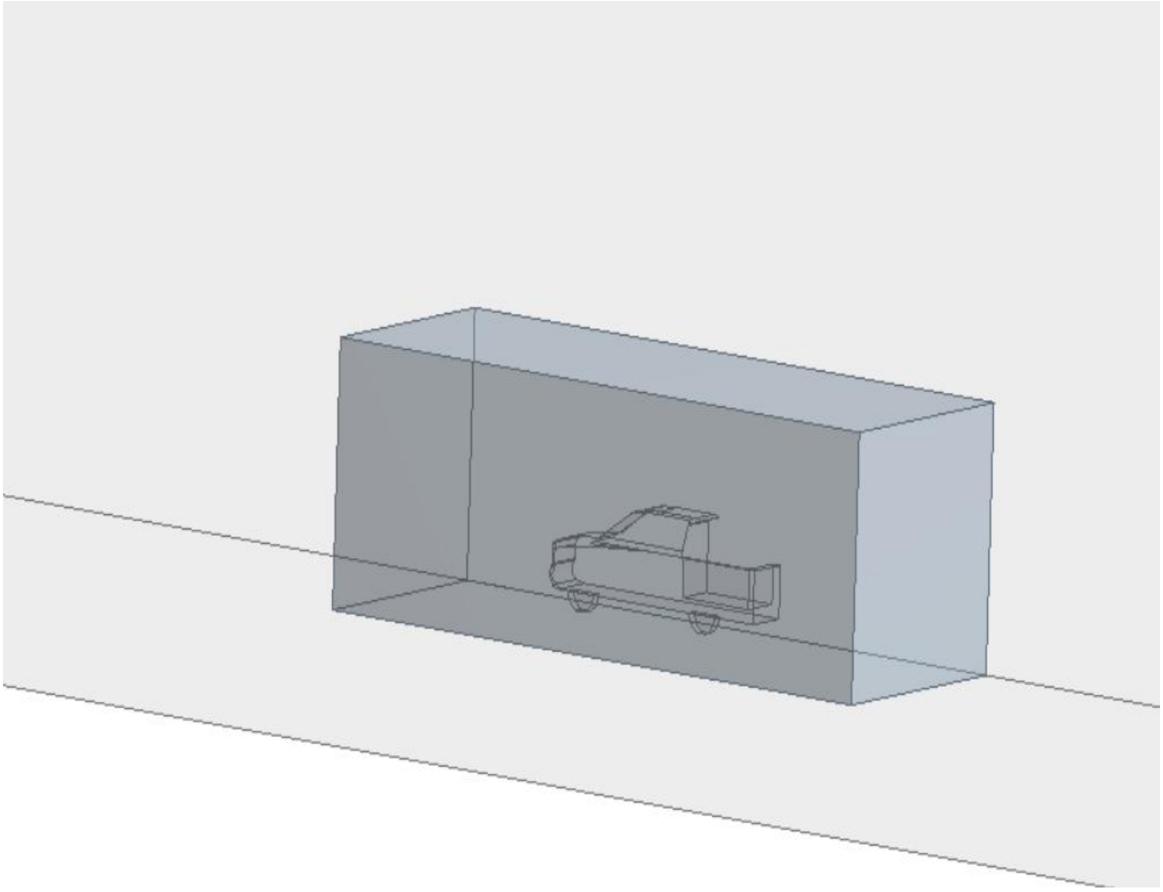

Figure A-3. Model one inside enclosure

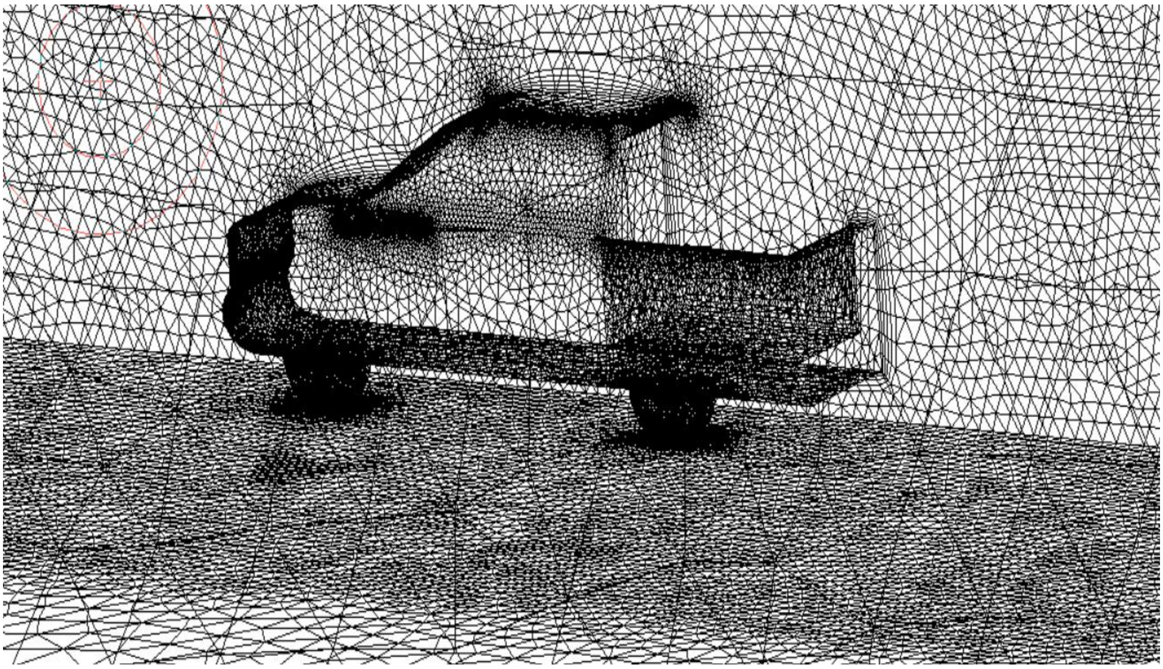

Figure A-4. Model one after meshing

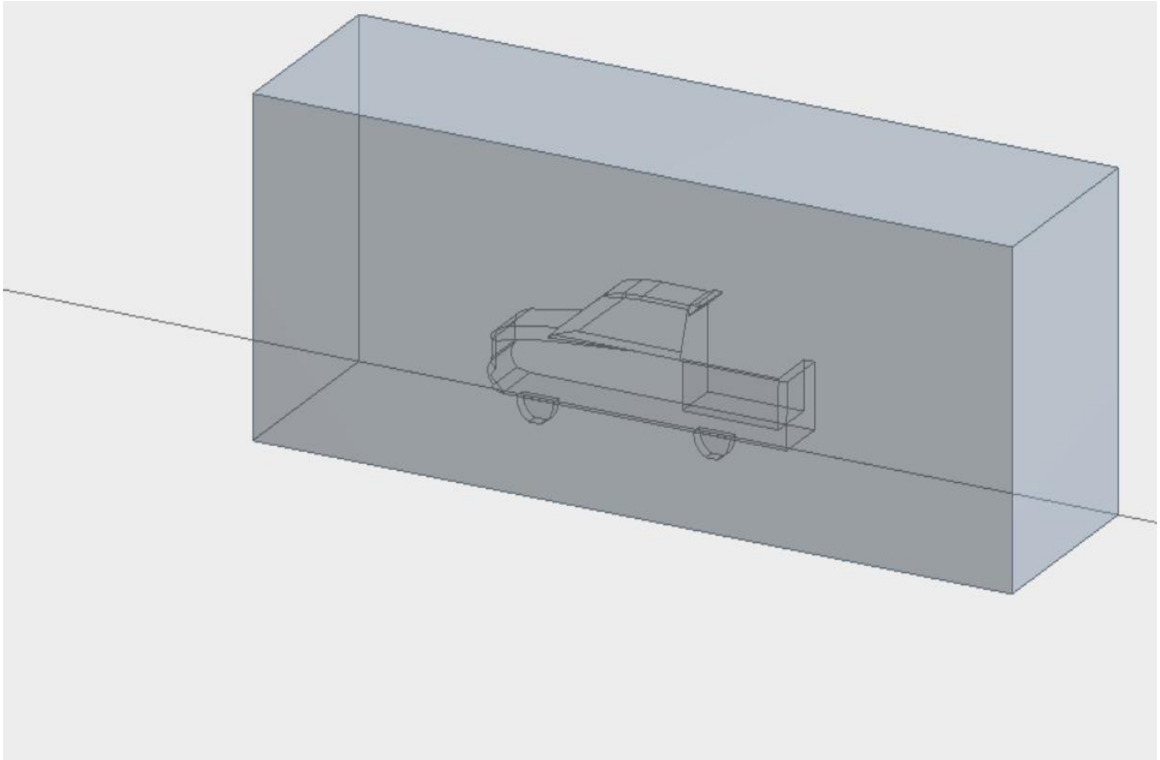

Figure A-5. Model two inside enclosure

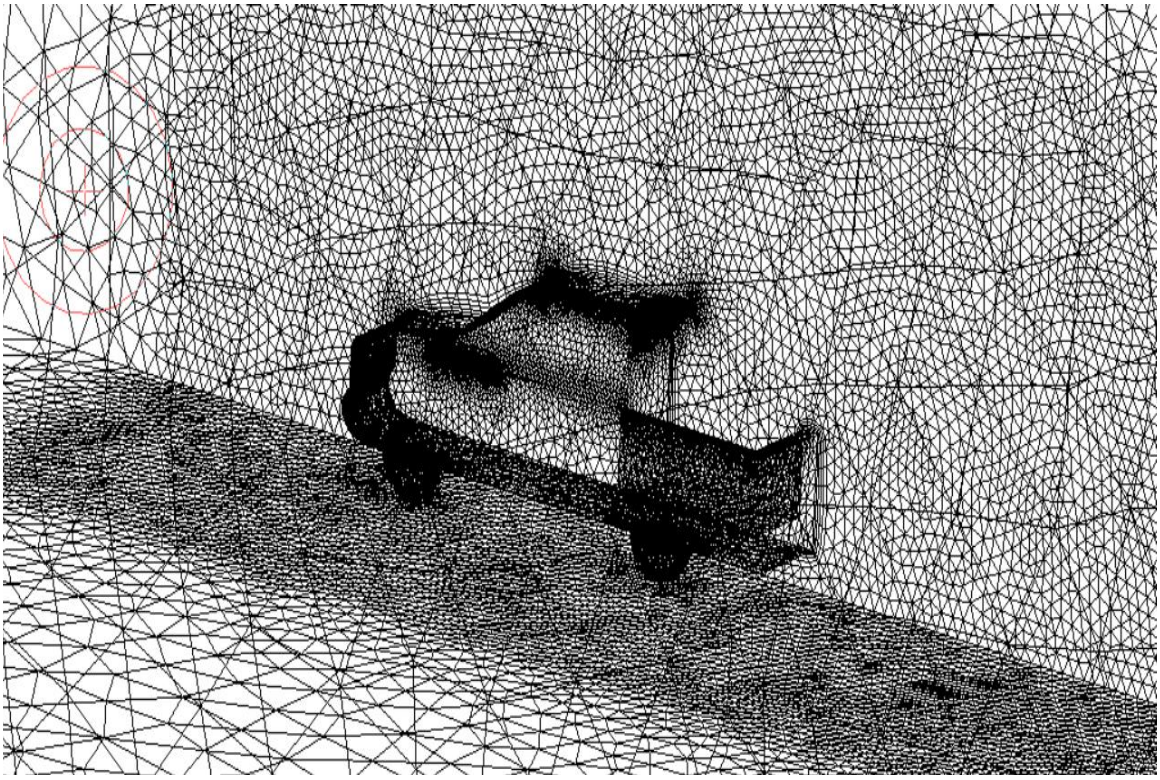

Figure A-6. Model two after meshing

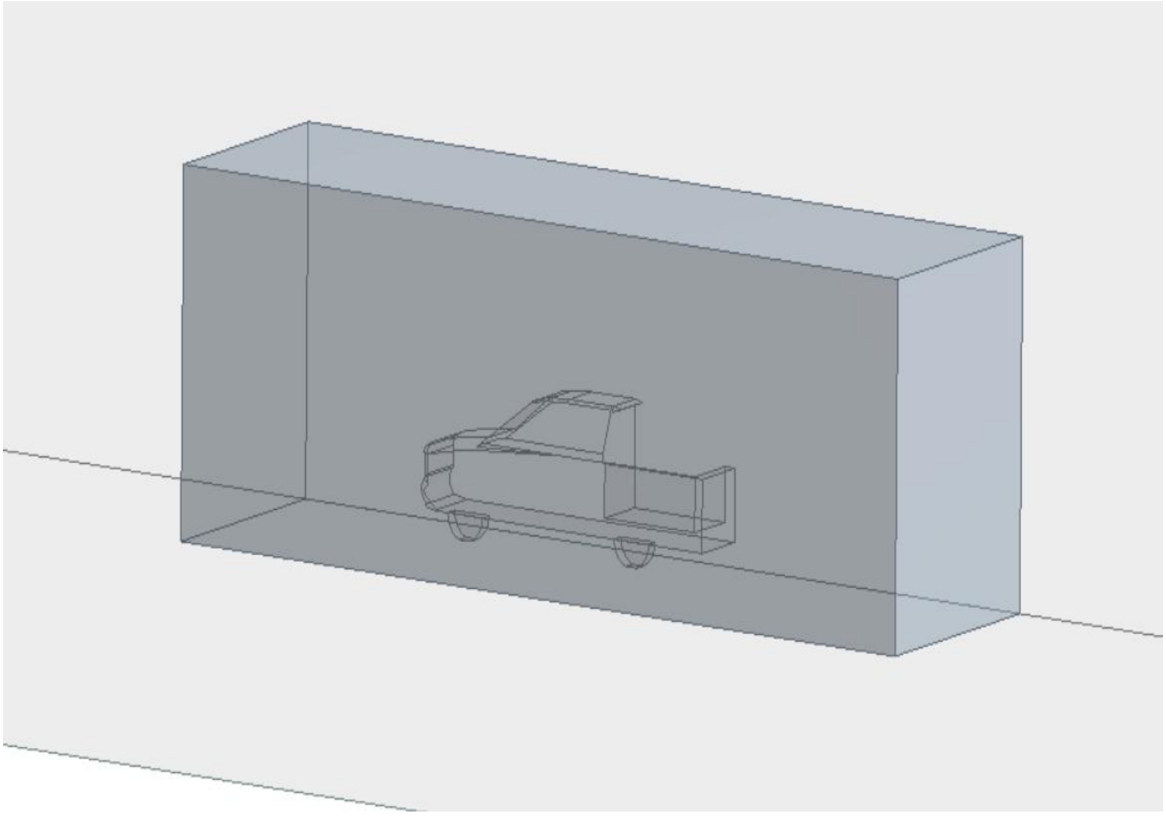

Figure A-7. Model three inside enclosure

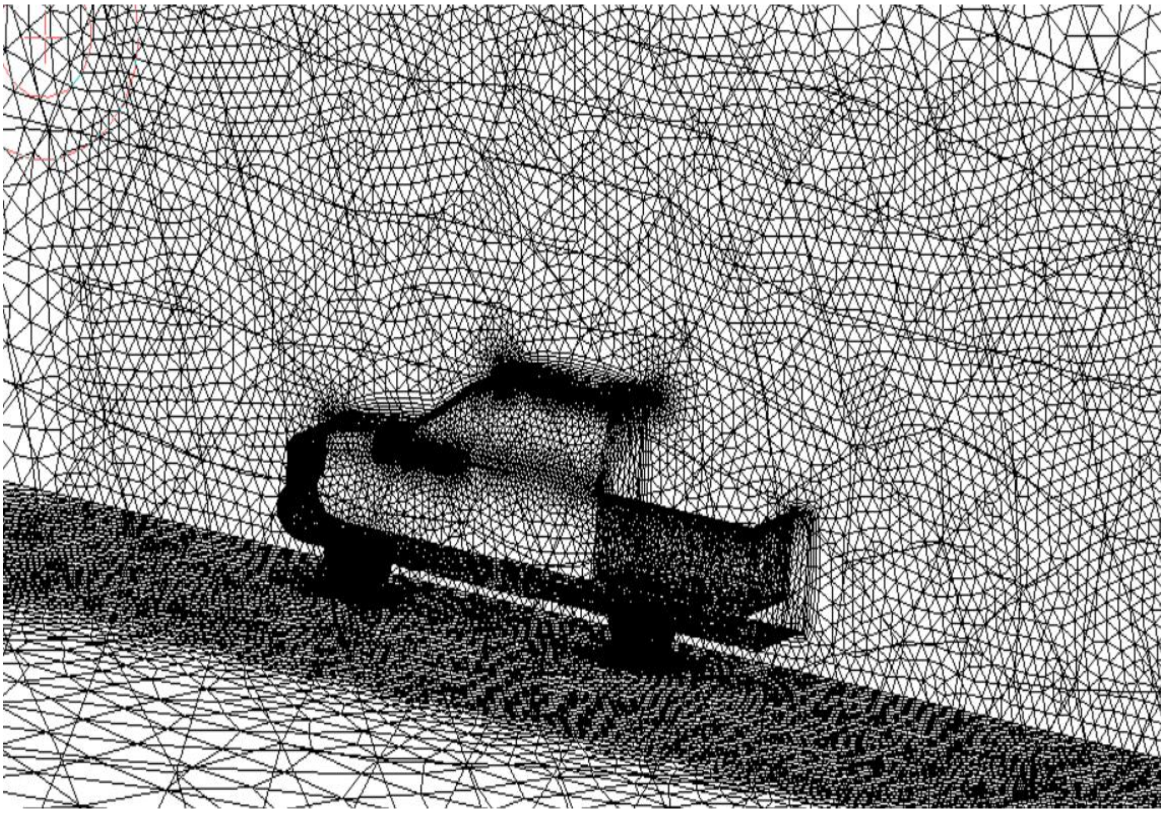

Figure A-8. Model three after meshing

Appendix B: SolidWorks Modelling

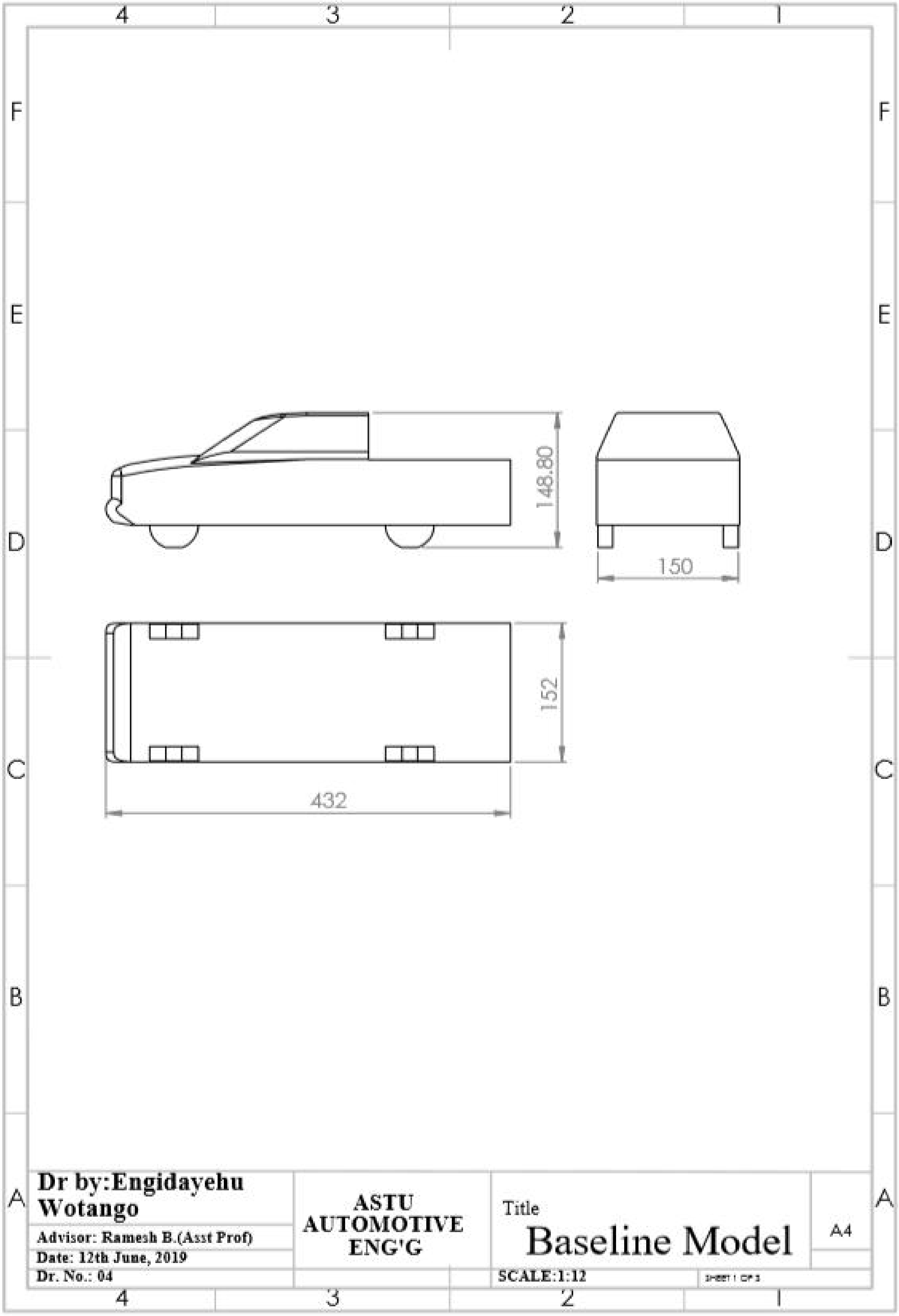

Figure B-1. Baseline model Multiview

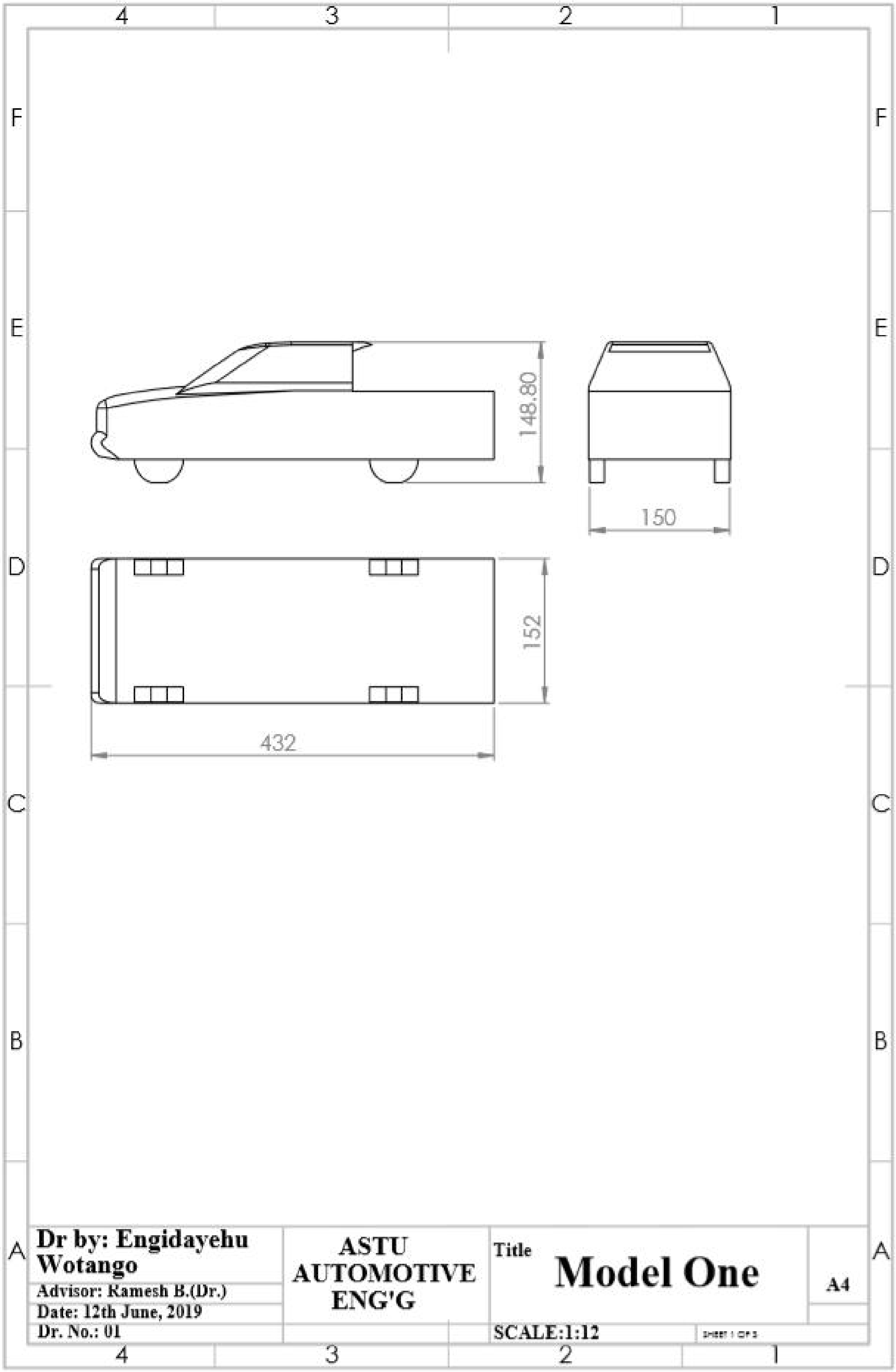

Figure B-2. Model one Multiview

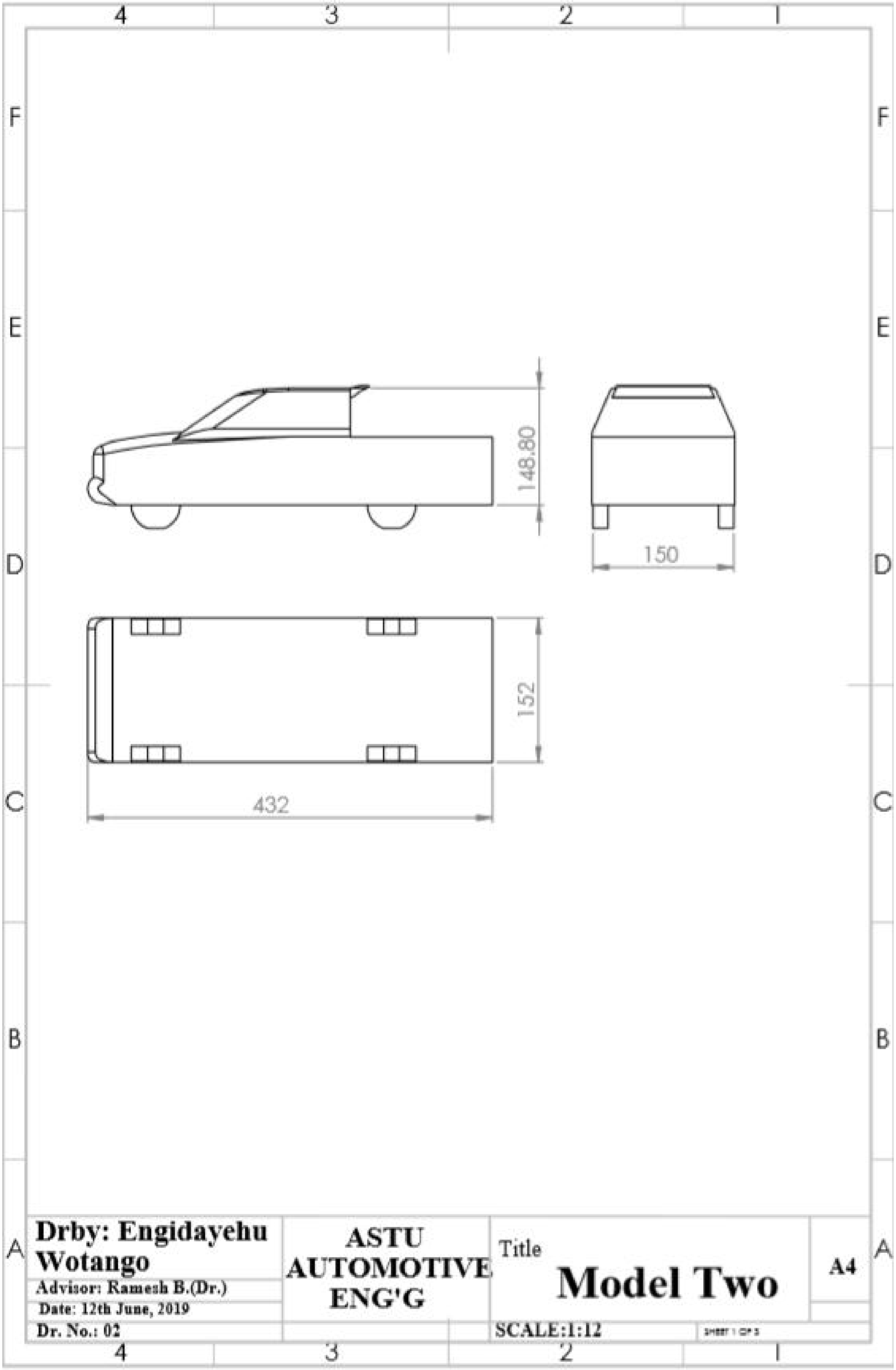

Figure B-3. Model two Multiview

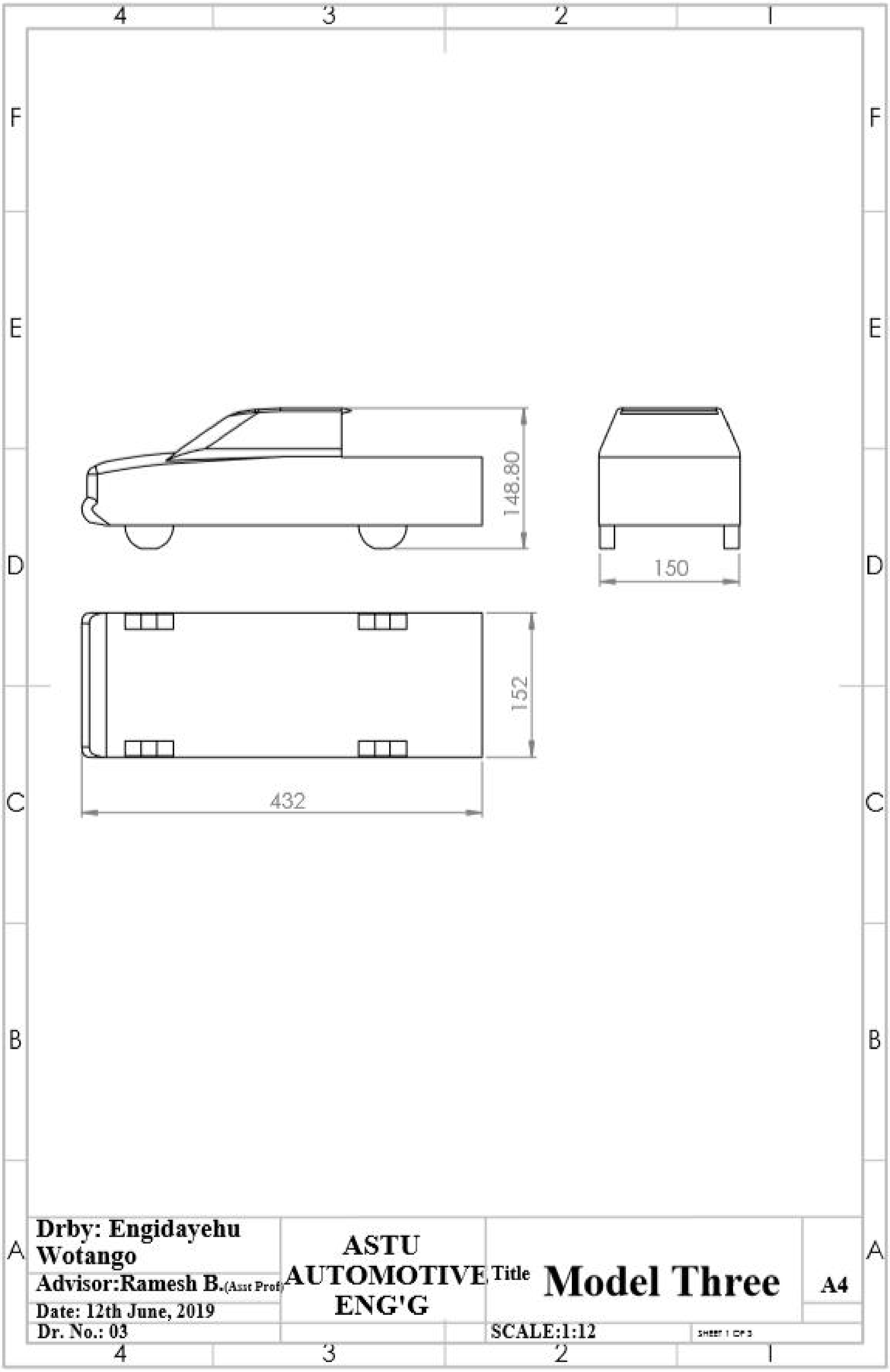

Figure B-4. Model three Multiview

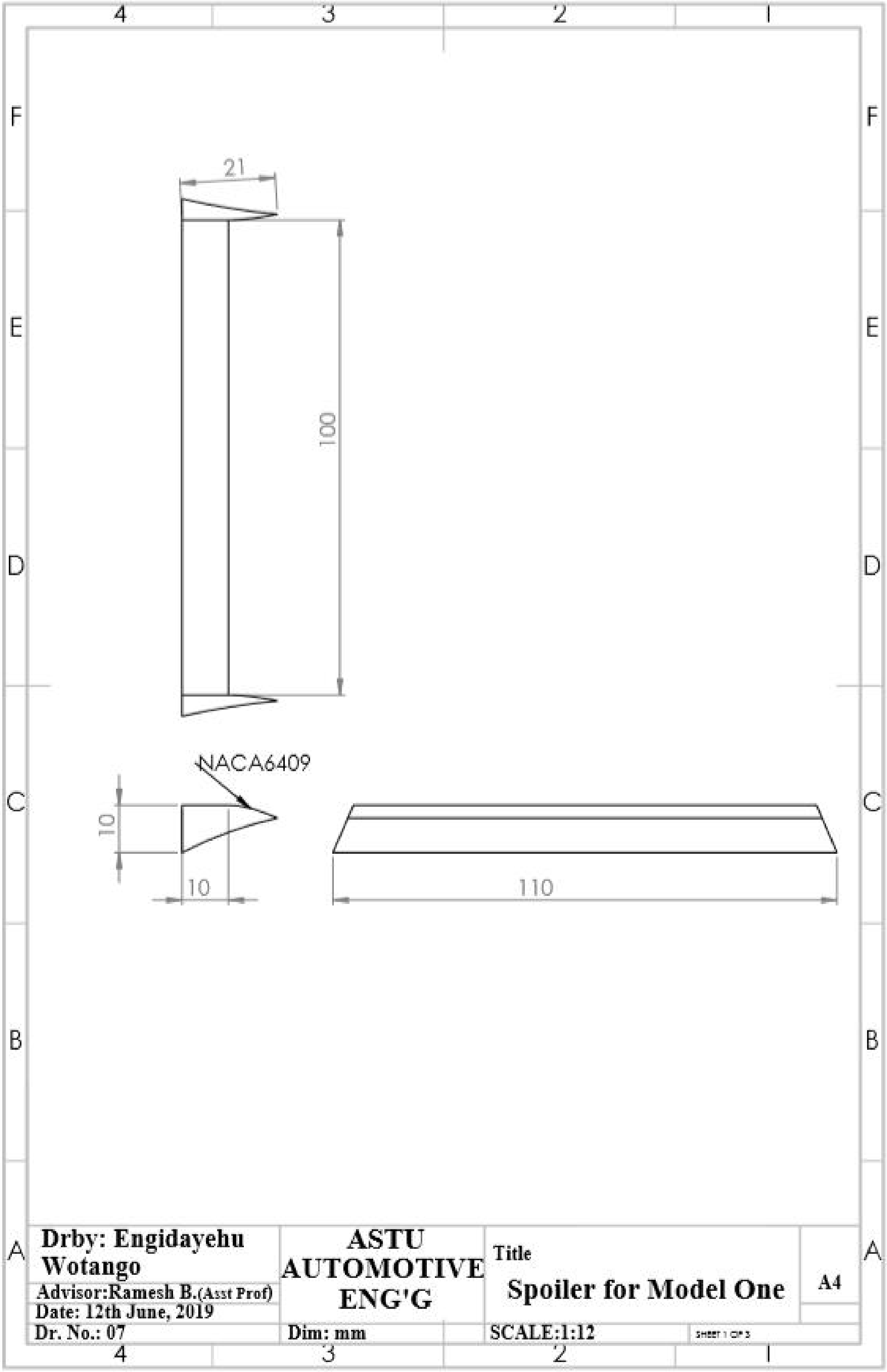

Figure B-5. Long Spoiler Multiview

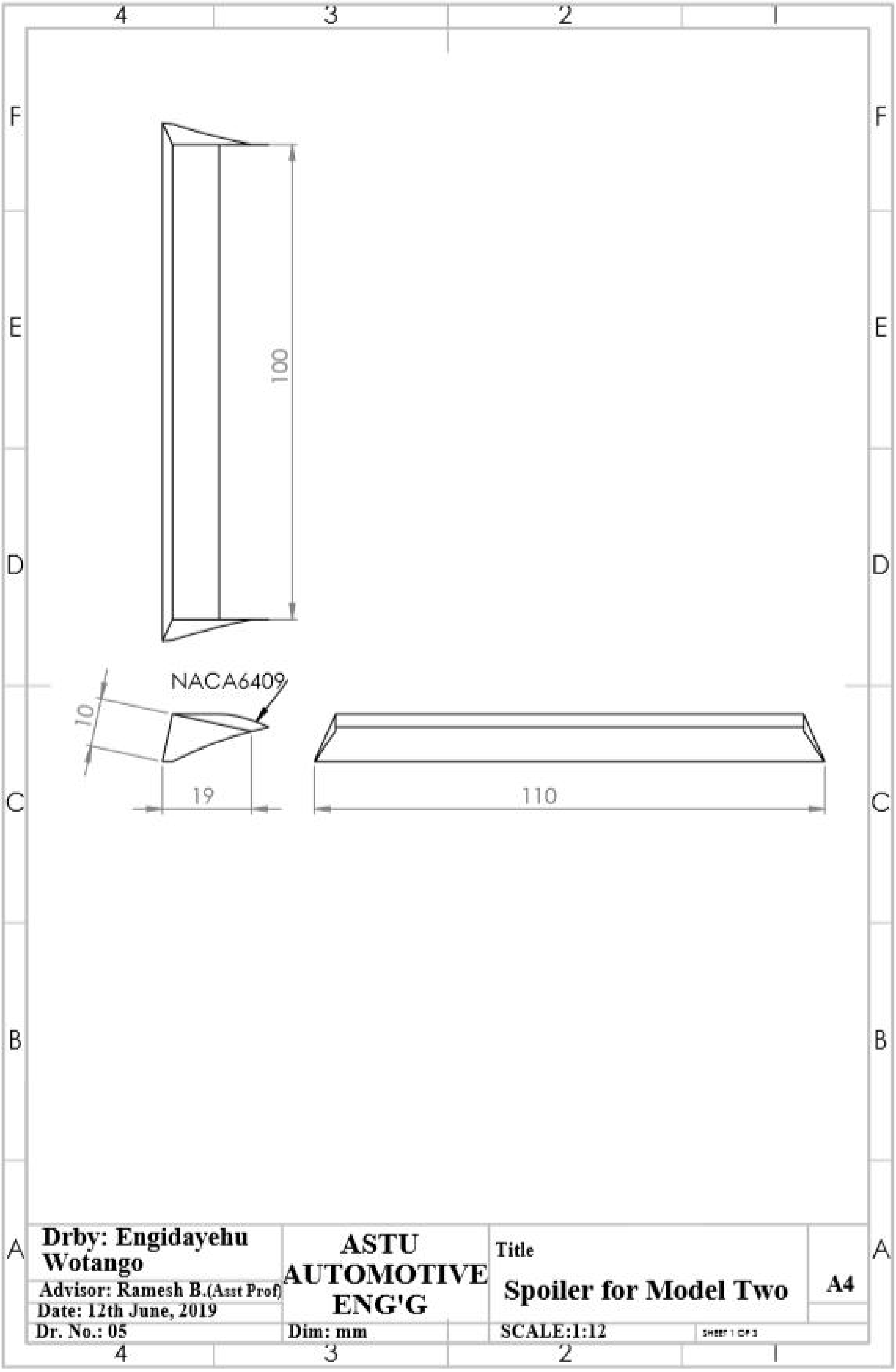

Figure B-6. Model two spoiler Multiview

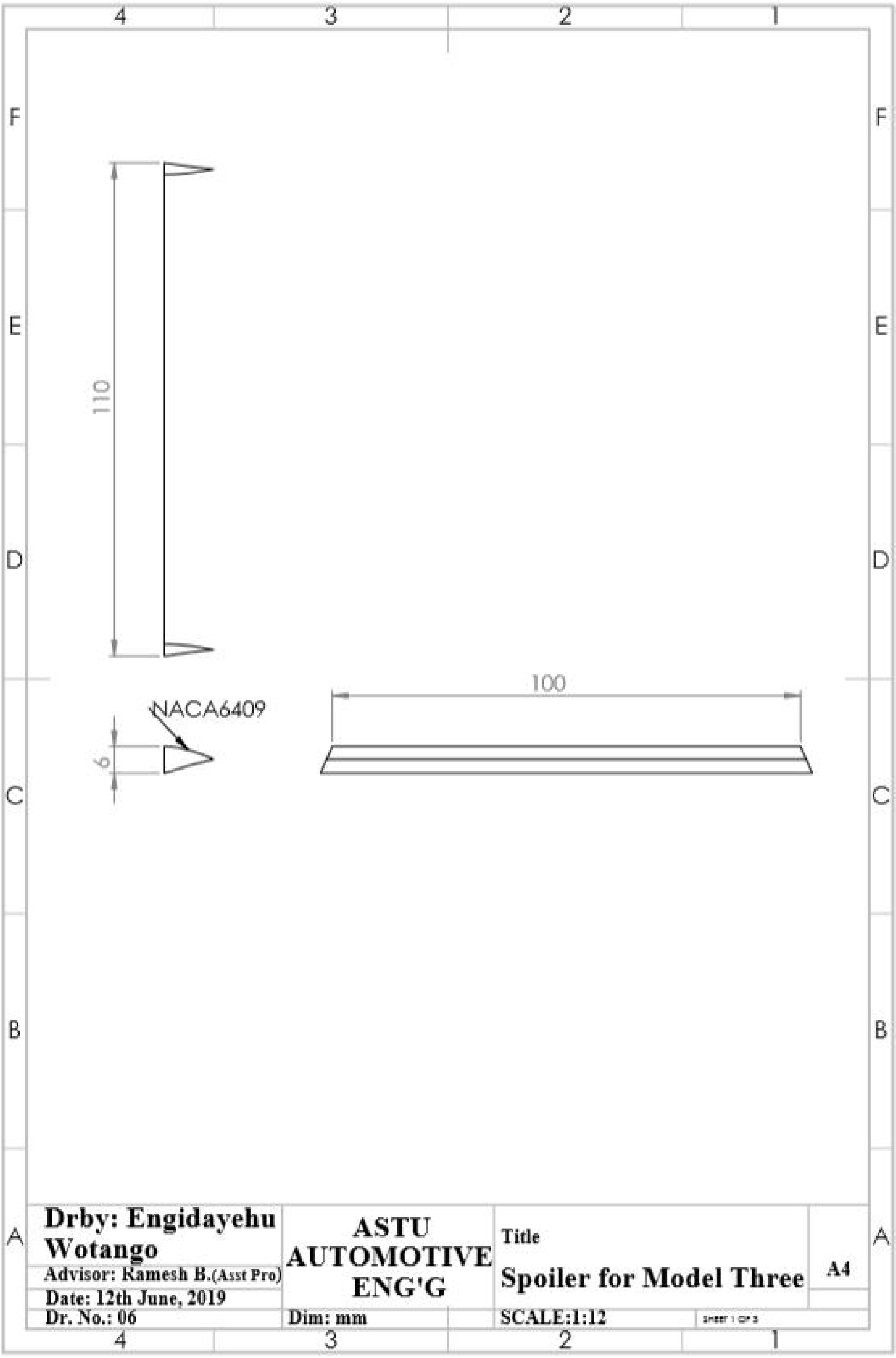

Figure B-7. Short Spoiler Multiview

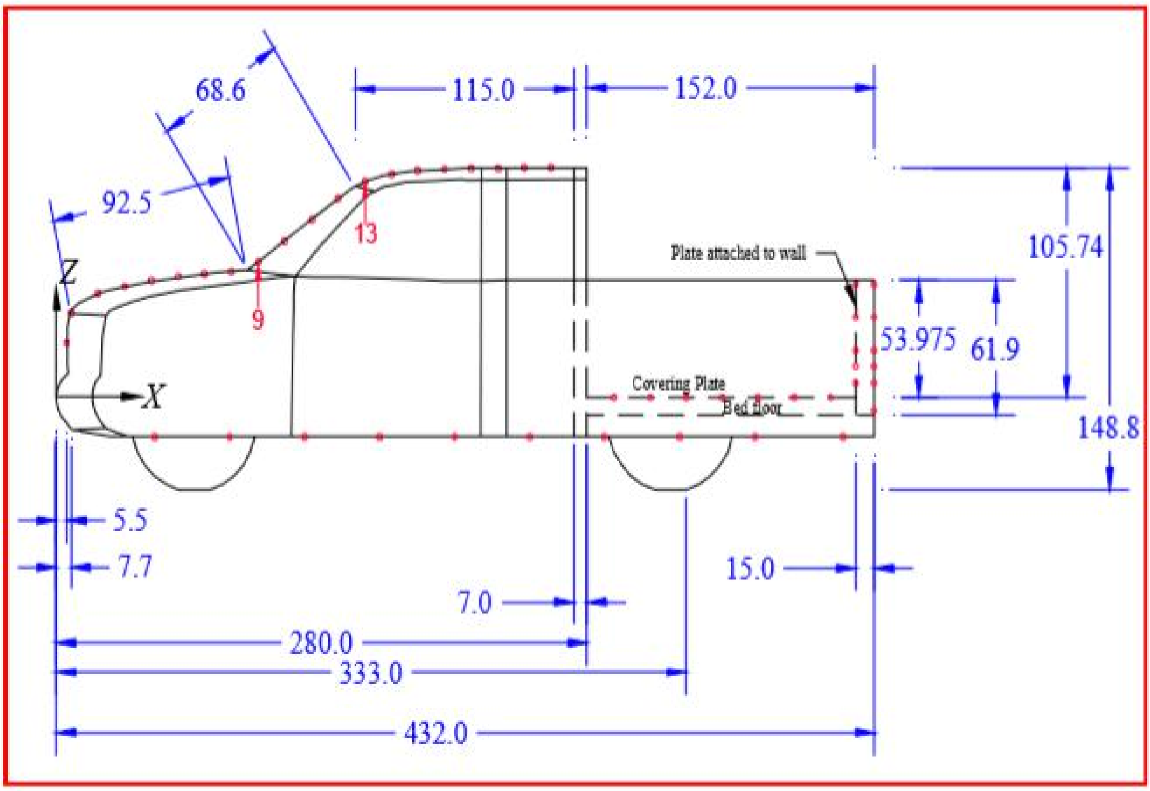

Figure B-8. 1/12 Scaled down Generic Pickup Vehicle Side view

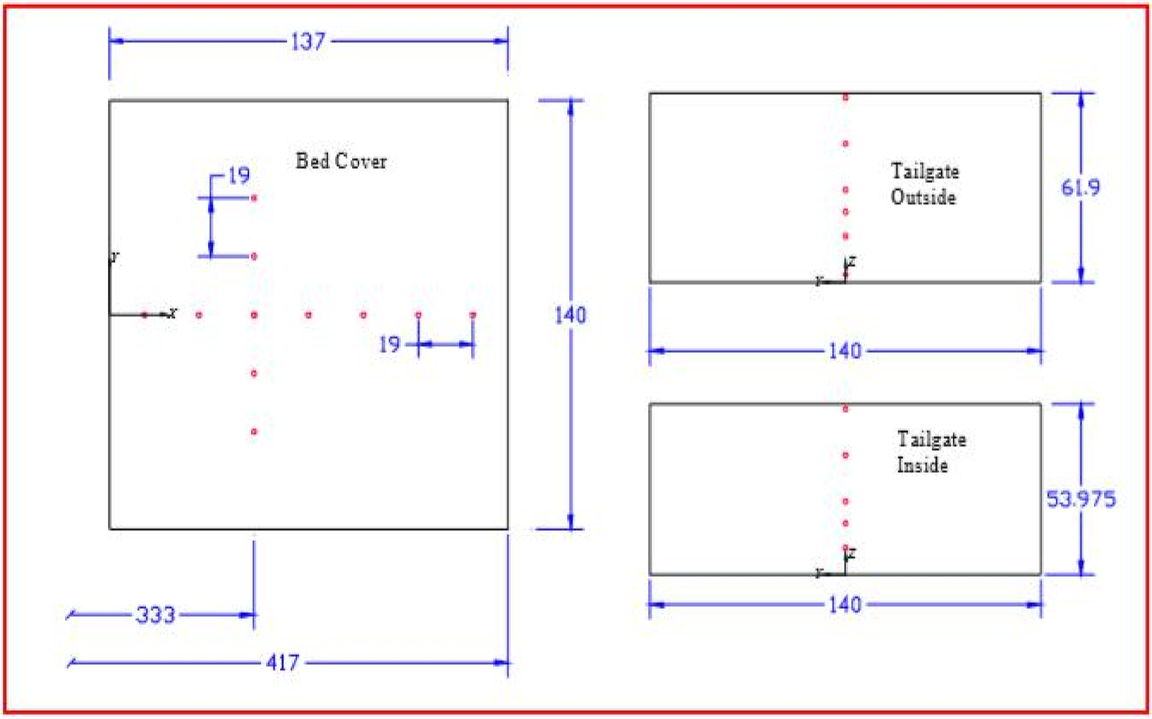

Figure B-9. 1/12 Scaled Down Generic Pickup Vehicle Bed cover and tailgate view

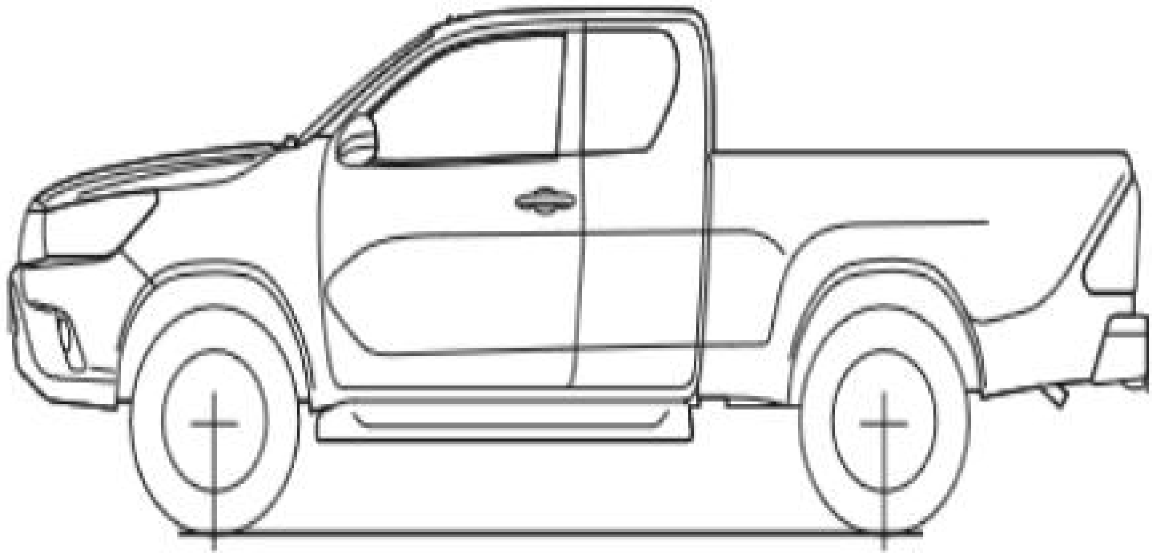

Figure B-10 *Extended cab Toyota pickup vehicle*

HiLux – 4x4		2.4L turbo diesel	
Applicability		4x4	
Engine	Name	2GD-FTV	
	Displacement (cm³)	2393	
	Max power² (kW@rpm)	110@3400	
	Max torque² (Nm@rpm)	400@1600-2000	
	Valve train	16-valve DOHC	
	Fuel system	Fuel injection with common rail	
	Fuel capacity (L)	80	
	Bore x stroke (mm)	92.0 x 90.0	
	Compression ratio	15.6:1	
Transmission	Type	Manual	Automatic
	Number of ratios	6-speed	6-speed
	Ratios (:1)	1st 4.784; 2nd 2.423; 3rd 1.443; 4th 1.000; 5th 0.777; 6th 0.643; Rev 4.066	1st 3.600; 2nd 2.090; 3rd 1.488; 4th 1.000; 5th 0.687; 6th 0.580; Rev 3.732
	Differential ratio (rear) (:1)	3.583	4.100

Figure B-11. Extended cab Toyota pickup specifications

APPENDIX C: Mesh Details

Table C-1. Baseline Model Mesh Detail

Object Name	*Mesh*
State	Solved
Defaults	
Physics Preference	CFD
Solver Preference	Fluent
Relevance	0
Sizing	
Size Function	Proximity and Curvature
Relevance Center	Fine
Initial Size Seed	Active Assembly
Smoothing	High
Transition	Slow
Span Angle Center	Fine
Curvature Normal Angle	Default (18.0 °)
Num Cells Across Gap	Default (3)
Proximity Size Function Sources	Faces and Edges
Min Size	Default (0.705130 mm)
Proximity Min Size	Default (0.705130 mm)
Max Face Size	Default (70.5130 mm)
Max Tet Size	Default (141.030 mm)
Growth Rate	Default (1.20)
Automatic Mesh Based Defeaturing	On
Defeaturing Tolerance	Default (0.352560 mm)
Minimum Edge Length	2.3975e-003 mm
Inflation	
Use Automatic Inflation	Program Controlled
Inflation Option	First Aspect Ratio
First Aspect Ratio	5.
Maximum Layers	5
Growth Rate	1.2
Assembly Meshing	
Method	Tetrahedrons
Feature Capture	Program Controlled
Tessellation Refinement	Program Controlled
Intersection Feature Creation	Program Controlled
Statistics	
Nodes	372762
Elements	2672004
Mesh Metric	None

Table C-2. Model One Mesh Detail

Object Name	*Mesh*
State	Solved
Defaults	
Physics Preference	CFD
Solver Preference	Fluent
Relevance	0
Sizing	
Size Function	Proximity and Curvature
Relevance Center	Fine
Initial Size Seed	Active Assembly
Smoothing	High
Transition	Slow
Span Angle Center	Fine
Curvature Normal Angle	Default (18.0 °)
Num Cells Across Gap	Default (3)
Proximity Size Function Sources	Faces and Edges
Min Size	Default (0.74120 mm)
Proximity Min Size	Default (0.74120 mm)
Max Face Size	Default (74.120 mm)
Max Tet Size	Default (148.240 mm)
Growth Rate	Default (1.20)
Automatic Mesh Based Defeaturing	On
Defeaturing Tolerance	Default (0.37060 mm)
Minimum Edge Length	2.3975e-003 mm
Inflation	
Use Automatic Inflation	All Faces in Chosen Named Selection
Named Selection	car
Inflation Option	First Aspect Ratio
First Aspect Ratio	5.
Maximum Layers	5
Assembly Meshing	
Method	Tetrahedrons
Feature Capture	Program Controlled
Tessellation Refinement	Program Controlled
Intersection Feature Creation	Program Controlled
Statistics	
Nodes	404201
Elements	2033495
Mesh Metric	None

Table C-3. Model Two Mesh Detail

Object Name	*Mesh*
State	Solved
Defaults	
Physics Preference	CFD
Solver Preference	Fluent
Relevance	0
Sizing	
Size Function	Proximity and Curvature
Relevance Center	Fine
Initial Size Seed	Active Assembly
Smoothing	High
Transition	Slow
Span Angle Center	Fine
Curvature Normal Angle	Default (18.0 °)
Num Cells Across Gap	Default (3)
Proximity Size Function Sources	Faces and Edges
Min Size	Default (0.74130 mm)
Proximity Min Size	Default (0.74130 mm)
Max Face Size	Default (74.130 mm)
Max Tet Size	Default (148.260 mm)
Growth Rate	Default (1.20)
Automatic Mesh Based Defeaturing	On
Defeaturing Tolerance	Default (0.370650 mm)
Minimum Edge Length	2.3975e-003 mm
Inflation	
Use Automatic Inflation	All Faces in Chosen Named Selection
Named Selection	car
Inflation Option	First Aspect Ratio
First Aspect Ratio	5.
Maximum Layers	5
Assembly Meshing	
Method	Tetrahedrons
Feature Capture	Program Controlled
Tessellation Refinement	Program Controlled
Intersection Feature Creation	Program Controlled
Statistics	
Nodes	329822
Elements	2622273
Mesh Metric	None

Table C-4. Model Three Mesh Detail

Object Name	*Mesh*
State	Solved
Defaults	
Physics Preference	CFD
Solver Preference	Fluent
Relevance	0
Sizing	
Size Function	Proximity and Curvature
Relevance Center	Fine
Initial Size Seed	Active Assembly
Smoothing	High
Transition	Slow
Span Angle Center	Fine
Curvature Normal Angle	Default (18.0 °)
Num Cells Across Gap	Default (3)
Proximity Size Function Sources	Faces and Edges
Min Size	Default (0.74120 mm)
Proximity Min Size	Default (0.74120 mm)
Max Face Size	Default (74.120 mm)
Max Tet Size	Default (148.240 mm)
Growth Rate	Default (1.20)
Automatic Mesh Based Defeaturing	On
Defeaturing Tolerance	Default (0.37060 mm)
Minimum Edge Length	2.3975e-003 mm
Inflation	
Use Automatic Inflation	All Faces in Chosen Named Selection
Named Selection	car
Inflation Option	First Aspect Ratio
First Aspect Ratio	5.
Maximum Layers	5
Assembly Meshing	
Method	Tetrahedrons
Feature Capture	Program Controlled
Tessellation Refinement	Program Controlled
Intersection Feature Creation	Program Controlled
Statistics	
Nodes	336737
Elements	2643764
Mesh Metric	None